4 Coaxial helicopter model

A coaxial helicopter model needs to be developed to investigate the hover and forward flight behavior of the coaxial helicopter. The characteristics of the helicopter model will be presented as well as the aerodynamic mutual interference of the two rotors.

4.1 Rotor characteristics

4.1.1 Azimuth angle and rotor angular velocity definition

In order to have a torque balance between the two main rotors, they are operating in opposite angular directions. As can been seen in Figure 4.1 and Figure 4.2, the upper rotor will be a counterclockwise rotating rotor (CCR) and the lower rotor a clockwise rotating rotor (CR).
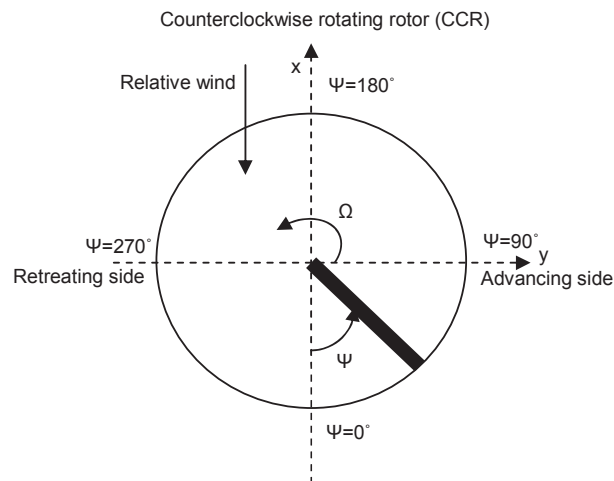
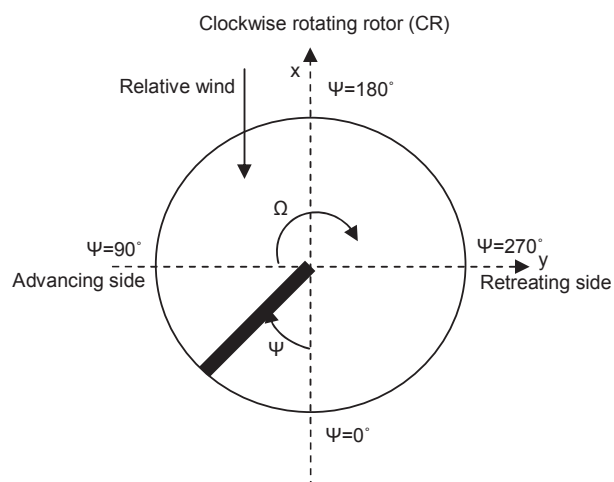**Figure 4.1: Azimuth angle and angular velocity of the CCR**

Figure 4.2: Azimuth angle and angular velocity of the CR

Because of the change in angular velocity, the advancing and retreating sides of the rotor have changed sides. For the CCR case, the advancing side will appear at the positive *y* direction and the advancing side will appear at the negative *y* direction for the CR case.

4.1.2 Reference axes and planes

Basically three physical rotor reference planes can be distinguished:

1. *Shaft plane (SP)*: The rotor shaft plane (or hub plane) is perpendicular to the rotor shaft. Because the SP is linked to the physical part of the helicopter, it will be used to describe the dynamics of the rotor blade. An observer in the SP will see both the flapping and the feathering motion.

2. *Control plane (CP)*: The rotor control plane (or no feathering plane) is normally used for performance analysis and is connected to the swashplate. In the CP, the observer will see no feathering (cyclic pitch) motion of the blade, but will see the flapping motion of the blade.

3. *Disk plane (DP)*: The rotor disk plane (or tip path plane) follows the motion of the blade tips through space and will be used for the aerodynamic analyses of the rotor. The mutual interference of the two rotors will be calculated in this plane. An observer in the DP will not see the flapping neither the feathering motion of the blade.

The three reference axes and planes are illustrated in Figure 4.3.
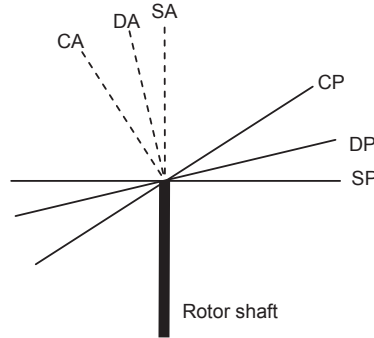

Figure 4.3: Rotor reference planes and axes

4.1.3 Determining of the flapping motion

As a response to the aerodynamic and centrifugal forces on a rotor blade, the rotor blades undergo a flapping motion each revolution. Assuming the flapping motion as a Fourier series, one gets the following factors: the coning angle a_0, the longitudinal flapping a_1, and the lateral flapping b_1. The flapping motion for the CCR and the CR are respectively equal to eq. (4.1) and (4.2).

$$\beta_u(\psi) = a_{0u} - a_{1u}\cos(\psi) - b_{1u}\sin(\psi) \qquad (4.1)$$

$$\beta_l(\psi) = a_{0l} - a_{1l}\cos(\psi) - b_{1l}\sin(\psi) \qquad (4.2)$$

As can be seen in Figure 4.4 and Figure 4.5 the flapping angle a_1 is taken positive when the TPP tilts backwards for both rotors. The flapping angle b_1 is positive to the right for the CCR and b_1 is positive to the left for the CR.
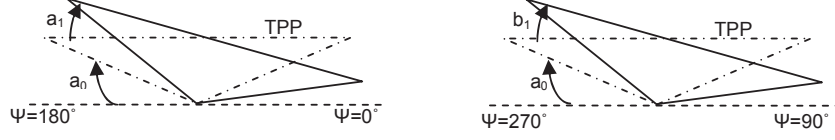

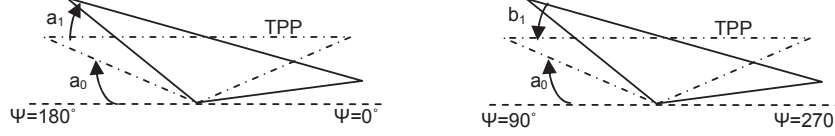Figure 4.4: Definition of the flapping angles for a CCR

Figure 4.5: Definition of the flapping angles for a CR

The disc tilt angles will be considered as steady state angles and can be calculated according to ref. 46:

$$\left(v_\beta{}^2 - 2\frac{r}{\Omega}\right)a_0 = \frac{\gamma}{8}\left(1 + \mu_x{}^2 - 2\frac{r}{\Omega}\right)\theta_0 - \frac{\gamma}{6}\mu_y\theta_{1c} - \frac{\gamma}{6}\mu_x\theta_{1s} + \frac{\gamma}{8}\left(\frac{4}{5} - \frac{8}{5}\frac{r}{\Omega} + \frac{2}{3}\mu_x{}^2\right)\theta_{tw} -$$
$$- \frac{\gamma}{6}(-\mu_z + \lambda_i) + \frac{\gamma}{12}\mu_x\frac{p}{\Omega} + \frac{\gamma}{12}\mu_y\frac{q}{\Omega} \tag{4.3}$$

$$\left(1 - \frac{r}{\Omega} - \frac{\mu_x{}^2}{2} - \frac{\mu_y{}^2}{2}\right)a_1 = \frac{\gamma}{6}\mu_y a_0 + \frac{\gamma}{3}\mu_x\theta_0 - \frac{\gamma}{8}\mu_x\mu_y\theta_{1c} - \frac{\gamma}{8}\left(1 - 2\frac{r}{\Omega} + \frac{3}{2}\mu_x{}^2\right)\theta_{1s} +$$
$$+ \frac{\gamma}{4}\mu_x\theta_{tw} - \frac{\gamma}{4}\mu_x(-\mu_z + \lambda_i) + \frac{\gamma}{8}\frac{p}{\Omega} - 2\frac{q}{\Omega} \tag{4.4}$$

$$\left(-1 + \frac{r}{\Omega} - \frac{\mu_x{}^2}{2} + \frac{\mu_y{}^2}{2}\right)b_1 = -\frac{\gamma}{6}\mu_x a_0 + \frac{\gamma}{3}\mu_y\theta_0 - \frac{\gamma}{8}\left(1 - 2\frac{r}{\Omega} + \frac{\mu_x{}^2}{2}\right)\theta_{1c} -$$
$$- \frac{\gamma}{8}\mu_x\mu_y\theta_{1s} + \frac{\gamma}{4}\mu_y\theta_{tw} - \frac{\gamma}{8}\mu_y(-\mu_z + \lambda_i) + 2\frac{p}{\Omega} + \frac{\gamma}{8}\frac{q}{\Omega} \tag{4.5}$$

4.1.4 Determining blade feathering motion of a coaxial rotor

The blade feathering (pitch) motion has two sources: the elastic deformation (twist) of the control system and blade, and the commanded input from the helicopter control system. The commanded input of the control system can be controlled by the pilot and consists of three different factors: the collective pitch θ_0, the lateral cyclic pitch θ_{1c}, and the longitudinal cyclic pitch θ_{1s}. For the counterclockwise rotating rotor (CCR) the feathering motion is equal to eq. (4.6).

$$\theta(y, \psi) = \theta_{0u} - \theta_{1c}\cos(\psi) - \theta_{1s}\sin(\psi) + \frac{\theta_{twist}\,y}{R} \tag{4.6}$$

Collective pitch θ_0

The thrust of the rotor can be directly influenced by increasing the lift of the whole rotor, and thus by increasing the collective pitch angle of the rotor. With a coaxial rotor configuration it is important to have a torque balance between both rotors in a trimmed condition. To achieve this, and keeping in mind that the lower rotor is influenced by the upper rotor, both rotors must be able to deliver a different thrust. This calls for separate collective pitch angles for the upper and lower rotor.

Lateral cyclic pitch θ_{1c}

By controlling the lateral cyclic pitch θ_{1c} the pilot controls the roll angle at ψ=0˚ and ψ=180˚ and this will lead 90˚ later (because of the gyroscopic effects) to an increase or decrease of the local lift, and thus to a left or a right turn of the rotor disk. A positive pitch angle applied at ψ=0˚ with a CCR will result in a laterally left tilt of the rotor disk. A positive pitch angle applied at ψ=0˚ with a CR will result in a laterally right tilt of the rotor disk. By keeping the same feathering motion as in eq. (4.6), both rotors would counteract each others motion and the helicopter would be uncontrollable. So, the positive pitch angle should be given at ψ=180˚. This can be done by making a phase shift of π or by just multiplying the cosine function by -1.

Longitudinal cyclic pitch θ_{1s}

By controlling the longitudinal cyclic pitch θ_{1s} the pilot controls the pitch angle at ψ=90˚ and ψ=270˚ and this will 90˚ later lead to an increase or decrease of the local lift, and thus to a forward or a backward tilt of the rotor disk. A positive pitch angle at the advancing side (ψ=90˚) with a CCR will result in a longitudinal backward tilt of the rotor disk. A positive pitch angle at the advancing side (ψ=90˚) with a CR will also result in a longitudinal backward tilt of the rotor disk. So for the longitudinal cyclic pitch, the sign is the same as in eq. (4.6).

The total feathering motion for a CR can be written as in eq. (4.7) .

$$\theta_l(y,\psi) = \theta_{0l} + \theta_{1c}\cos(\psi) - \theta_{1s}\sin(\psi) + \frac{\theta_{twist}\, y}{R} \tag{4.7}$$

The total cyclic motion including flapping and feathering motion for a CR and a CCR can be seen in Figure 4.6 and Figure 4.7.
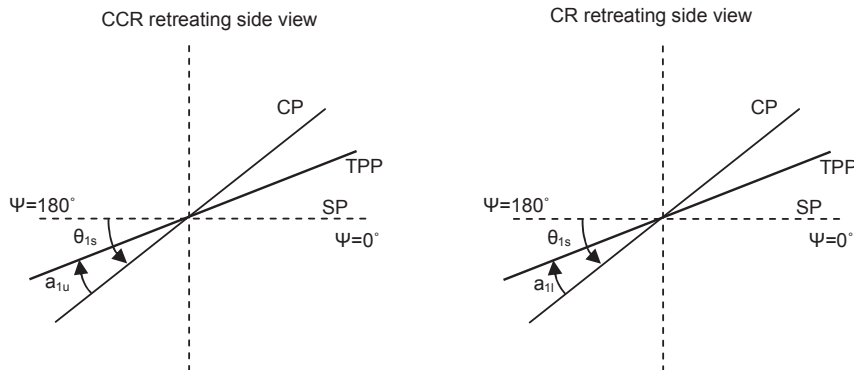

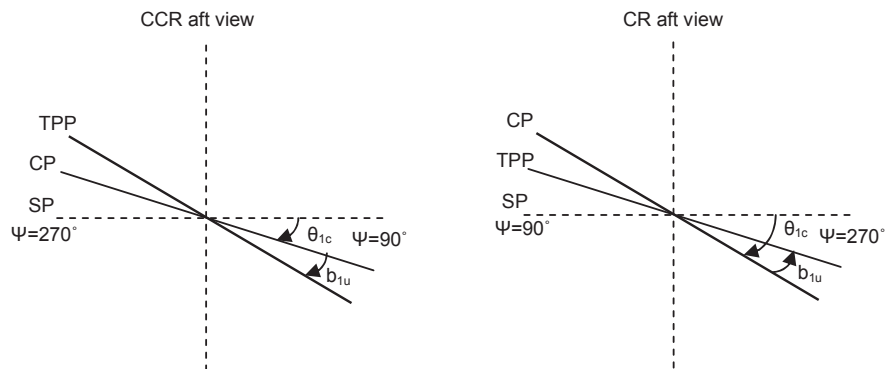**Figure 4.6: Flapping and feathering in the lateral plane**

Figure 4.7: Flapping and feathering in the longitudinal plane

4.1.5 Mutual interference between the rotors

The lower rotor is much more influenced by the upper rotor than the other way around. Because of this there will be assumed that only the upper rotor will affect the lower rotor. The upper rotor inflow will be treated as a uniform inflow.

If there would be no wake contraction of the upper rotor wake, the upper rotor will influence the entire lower rotor as shown in Figure 4.8.
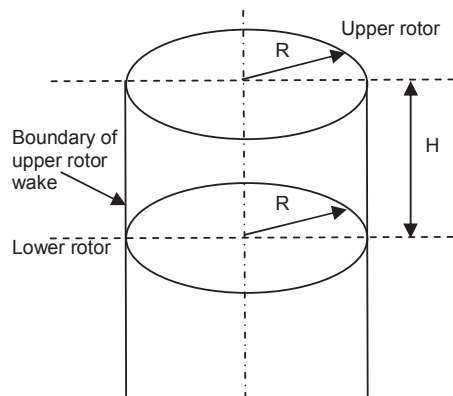

Figure 4.8: Influence of upper rotor wake on the lower rotor without wake contraction

For a coaxial rotor configuration, the axial spacing between the upper and the lower rotor is not large. For a Ka-32 coaxial helicopter the non-dimensional axial spacing is equal to $H/R = 0.189$. Nevertheless, the wake will contract the most near the rotor (see Figure 4.9). To check whether the wake contraction needs to be taken into account, Landgrebe's generalized wake model (ref. 37) will be used.
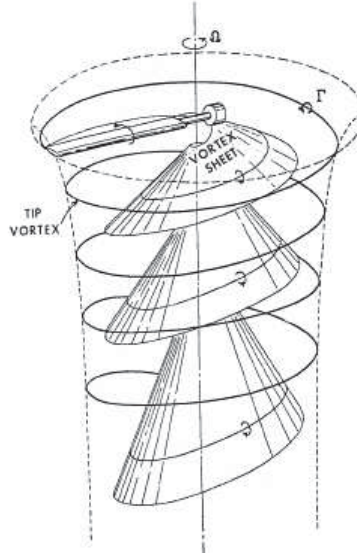
Figure 4.9: Hovering rotor wake structure (from ref. 37)

Landgrebe (ref. 37) has shown that both axial z_{tip} and radial y_{tip} coordinates of the local tip vortex can be well represented by the equations (4.8) and (4.9).

$$\frac{z_{tip}}{R} = k_1 \psi_w \qquad\qquad\qquad \text{for } 0 \leq \psi_w \leq 2\pi / N_b$$

$$\frac{z_{tip}}{R} = (\frac{z_{tip}}{R})_{\psi_w = 2\pi/N_b} + k_2(\psi_w - \frac{2\pi}{N_b}) \quad \text{for } \psi_w \geq 2\pi / N_b \tag{4.8}$$

and

$$\frac{y_{tip}}{R} = A + (1-A)\exp(-\Lambda \psi_w) \tag{4.9}$$

Ψ_w is known as the wake azimuth angle relative to the blade or the wake age. A and Λ are both empirical coefficients and are determined according to Landgrebe (ref. 32): *A=0.78* and *Λ=0.145+27C_T*. As can be seen in eq. (4.8) the axial coordinate of the tip vortex is linear with respect to the wake age. In the case of the coaxial rotor, the axial displacement is known as the axial spacing between the rotors. Now, it is easy to determine the wake age.

To check whether the wake age is within $\psi_w = 2\pi / N_b$, the thrust coefficient in hover needs to be determined by eq. (4.10).

$$C_{Thov} = \frac{T}{\rho(\Omega R)^2 \pi R^2} = \frac{W/2}{\rho(\Omega R)^2 \pi R^2} = \frac{98100/2}{1.225(226)^2 \pi 7.95^2} = 0.00395 \tag{4.10}$$

The constant k_1 can be approximated by the following empirical equation:

$$k_1 = 0.25 * (0.00395 / \sigma + 0.001\theta_{tw}) = 0.0171 \tag{4.11}$$

At $\psi_w = 2\pi / N_b$ the axial displacement is equal to

$$\left(\frac{z_{tip}}{R}\right)_{\psi_w=2\pi/N_b} = k_1\psi_w = k_1\frac{2\pi}{N_b} = 0.0694\frac{2\pi}{3} = 0.0358 \tag{4.12}$$

As can be seen in eq. (4.12), the 0.0358 is below the non-dimensional axial spacing between the rotors of 0.189, so also k_2 needs to be taken into account. The constant k_2 can be approximated by the following empirical equation:

$$k_2 = -(1.41 + 0.0141\theta_{tw})\sqrt{C_T/2} = 0.0626 \tag{4.13}$$

The wake age Ψ_w at H/R = 0.189 can now be determined by rewriting eq. (4.8):

$$\psi_w = \frac{\left(\frac{z_{tip}}{R}\right) - \left(\frac{z_{tip}}{R}\right)_{\psi_w=2\pi/N_b} + k_2\frac{2\pi}{N_b}}{k_2} = 4.5416 \text{ rad} \tag{4.14}$$

After determining the wake age Ψ_w with eq. (4.14), the radial contraction of the rotor wake can now be calculated with eq. (4.9).

$$\frac{y_{tip}}{R} = wc = A + (1-A)\exp(-\Lambda\psi_w) = 0.78 + (1-0.78)\exp(-(0.145 + 27 \cdot 0.00395) \cdot 4.5416) = 0.8502$$
$$\tag{4.15}$$

As can be seen in eq. (4.15), the wake contraction at the axial position of the lower rotor is already 0.8502. So, the wake contraction of the upper rotor wake has to be taken into account during the calculation of the interference effects between the two rotors. Note that the prescribed wake model of Landgrebe is normally only suitable for hovering flight. For simplicity, it will be assumed that the wake contraction will remain the same in forward flight. However, because of the free-stream component of the velocity at the rotor plane in forward flight, the wake will be influenced behind as well as below the rotor and it takes on a more complicated (non-axisymmetric) form (Leishman, ref. 39). Most likely, the wake contraction will decrease by increasing forward speed, which means that the influence of the upper rotor wake on the lower rotor is a bit higher in reality.

Because of the wake contraction, two different regions on the lower rotor can be distinguished. This can be seen in Figure 4.10. This means also that there are two different induced velocities on the lower rotor surface. The induced velocities are a summation of two factors:

1. The induced velocity created by the lower rotor λ_l
2. The induced velocity created by the upper rotor λ_u at the position of the lower rotor
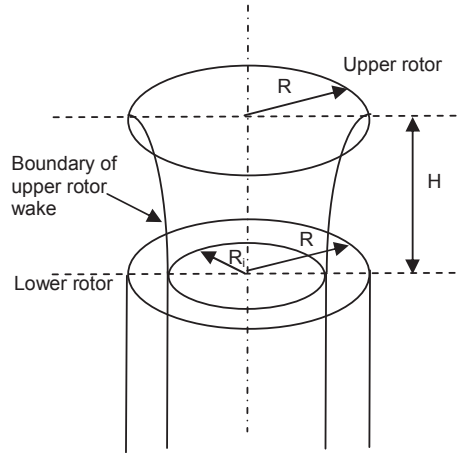
Figure 4.10: Influence of upper rotor wake on the lower rotor with wake contraction

Because the induced velocity created by the upper rotor has 'traveled' to the lower rotor, λ_u needs to be multiplied by a factor, which is called the attenuation coefficient C_{att}. Following Figure 4.10, there are two different induced velocities with their own attenuation coefficient:

$$\lambda_{l\_inner} = \lambda_{0l} + C_{att\_inner}\lambda_{0u} \qquad (4.16)$$

$$\lambda_{l\_outer} = \lambda_{0l} + C_{att\_outer}\lambda_{0u} \qquad (4.17)$$

Nagashima (ref. 42) has derived a formula for an unambiguous determination of the attenuation coefficients in hover as a function of the mutual spacing and rotor radius. However, to obtain the attenuation coefficients for forward flight there are more factors which need to be taken into account. The attenuation coefficient will be determined in the next paragraph.

Determining the attenuation coefficient

To determine the attenuation coefficient, one has to investigate the behavior of the upper rotor wake below the upper rotor. To be more specific, the strength of the upper rotor wake at the lower rotor surface needs to be determined. Nowadays, there are several experiments available which describe the rotor wake behavior below a lifting rotor. Most of these experiments are quite complicated and above all too difficult to implement the behavior of the rotor wake into the blade element method. Castles (ref. 18 and 19) succeeded actually to create a practical method for computing the approximate values of the normal component of the induced velocity in the flow field of a lifting rotor. As can be seen later in this paragraph, this method also meets the condition of the two different regions at the lower rotors surface.

Castles (ref. 18 and 19) assumed the rotor wake vortex distribution to consist of a straight semi-infinite elliptic cylinder. The elliptic cylinder is formed by an infinite number of vortex rings lying in planes parallel to the TPP and extending down to infinity. The straight elliptic cylinder coincides with the boundary of the wake. Wake contraction is not taken into account by Castles. Castles (ref. 19) has assembled a formula to calculate the ratio of the normal component of the induced velocity at any point (at radius y and azimuth angle ψ) to the normal component of the induced velocity at the center

of the rotor. The lines of constant induced velocity ratio in hover and in forward flight condition can be seen in Figure 4.11 and Figure 4.12.
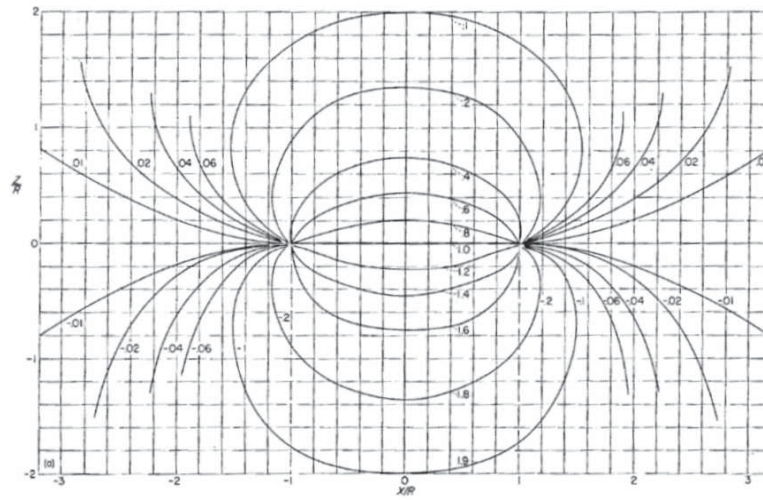

Figure 4.11: Lines of constant induced velocity ratio in hover (from ref. 18)
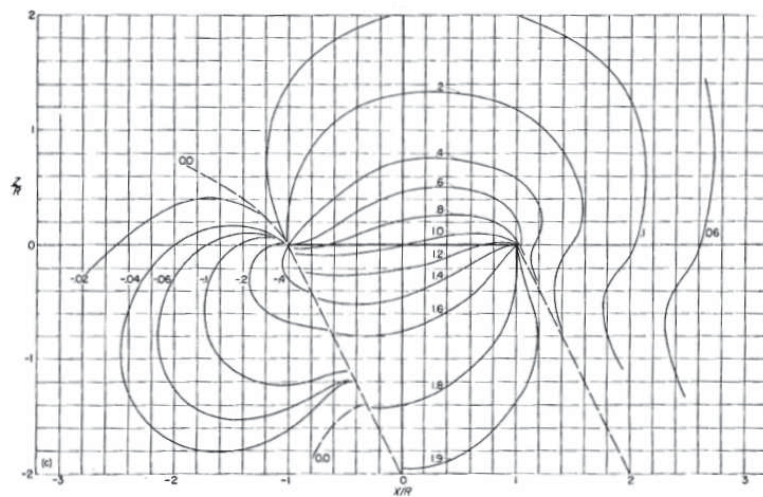

Figure 4.12: Lines of constant induced velocity ratio in forward flight (from ref. 18)

Because it has been assumed that the upper rotor has a uniform inflow, the normal component of the induced velocity at the center of the upper rotor is simply the induced velocity of the whole upper rotor λ_{0u}. As a matter of fact the calculated ratio of Castles' model is exactly the attenuation coefficient that is needed to determine the induced velocity of the lower rotor. So, the attenuation coefficient can be calculated by eq. (4.18) taken from Castles (ref. 19). The complete derivation of this formula can be seen in ref. 19.

$$C_{att} = \frac{1}{2\pi} \int_0^{2\pi} \frac{A - B\sqrt{C}}{\sqrt{C}(\sqrt{C} - D)} d\delta \qquad (4.18)$$

with

$$A = 1 + \frac{y\cos(\psi - \delta)}{R}$$

$$B = \frac{\tan(\chi)\cos(\delta)}{\sqrt{1 + \tan(\chi)^2}}$$

$$C = 1 + (y/R)^2 + (H/R)^2 + \frac{2y\cos(\psi - \delta)}{R} \qquad (4.19)$$

$$D = \frac{H/R + y/R \cdot \tan(\chi)\cos(\psi) + \tan(\chi)\cos(\delta)}{\sqrt{1 + \tan(\chi)^2}}$$

The χ in eq. (4.19) is known as the *wake skew angle* and can be determined, using Figure 4.13, as

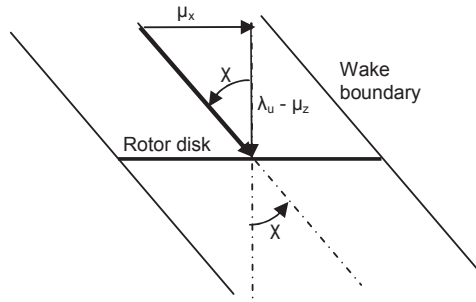$$\chi = \tan^{-1}\left(\frac{\mu_x}{\lambda_u - \mu_z}\right) \qquad (4.20)$$

Figure 4.13: Definition of the wake skew angle χ

As can be seen in Figure 4.11 and Figure 4.12, this method is also suitable to determine the attenuation coefficient in the area outside the boundary of the wake. This means that it is possible to use eq. (4.18) for both the inner part and the outer part of the lower rotor.

As mentioned before, it is necessary to take into account the contraction of the wake. In other words, the wake boundary of Figure 4.11 and Figure 4.12 needs to be shifted in such a way that the 'outside-the-wake-effects' take place earlier than on $y/R = 1$. To account for this effect the radius factors in eq. (4.19) will be multiplied by $j = \frac{1}{wc}$. Where wc is the wake contraction of the upper rotor wake. Eq. (4.19) becomes then eq. (4.21).

$$A = 1 + \frac{y \cdot j \cos(\psi - \theta)}{R}$$

$$B = \frac{\tan(\chi) \cos(\theta)}{\sqrt{1 + \tan(\chi)^2}}$$

$$C = 1 + (y \cdot j / R)^2 + (H / R)^2 + \frac{2y \cdot j \cos(\psi - \theta)}{R}$$

(4.21)

$$D = \frac{H / R + y \cdot j / R \cdot \tan(\chi) \cos(\psi) + \tan(\chi) \cos(\theta)}{\sqrt{1 + \tan(\chi)^2}}$$

After the calculation of the attenuation coefficient for every radius position y until $y = j*R$ (with $j > 0$) there has to be assumed that C_{att} is calculated for every y over the radius until R. In this way, the "outside-the-wake-effects" will take place within the radius R of the lower rotor. This is shown in Figure 4.14, where the wake contraction of the upper rotor wake is clearly present. Because the integration of eq. (4.21) over δ is too complicated to solve analytically, eq. (4.18) has been solved by using the Simpson integration rule. The integrated form of eq. (4.21) will be placed in a table for a set of radii y and azimuth angles ψ. The tabulated attenuation coefficients for hover are plotted in Figure 4.14. Here can be seen that the attenuation coefficient is negative for some parts outside the upper rotor wake. This is because of the upwash just outside the upper rotor wake.
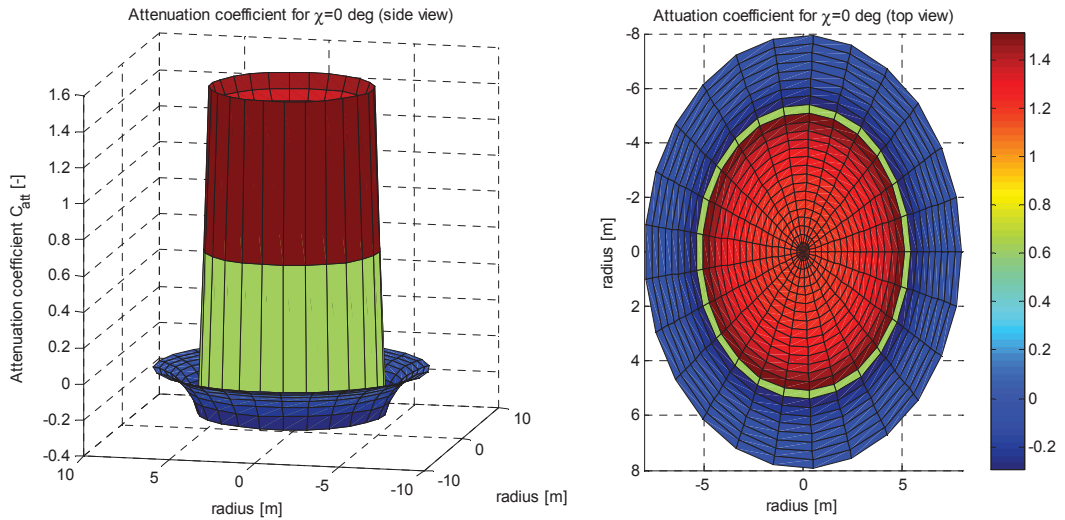

Figure 4.14: Attenuation coefficient in hover with wake contraction

Because eq. (4.21) cannot be solved analytically, it is impossible to implement this formula into the blade element method directly. It will also take to much computational time to determine the attenuation coefficient for each radius and azimuth angle and subsequently to apply the BEM for each radius and azimuth angle. In other words, it is necessary to approximate the attenuation coefficient.

There is a big difference between the attenuation coefficients inside and outside the upper rotor wake, so it is incorrect to use the same attenuation coefficient for the whole rotor. In order to determine a proper attenuation coefficient, the rotor will be separated in two sections first:

1. *Section 1:* Rotor in the positive *x* direction (from ψ = 90˚ to ψ = 270˚)
2. *Section 2:* Rotor in the negative *x* direction (from ψ = 270˚ to ψ = 90˚)

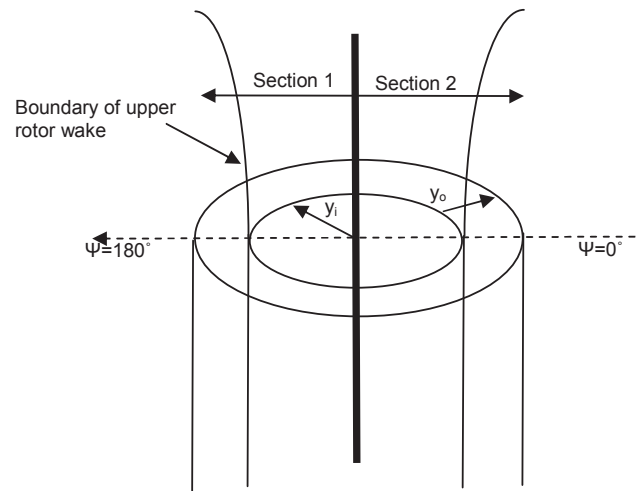The division of the two sections is shown in Figure 4.15.

Figure 4.15: Sections of the lower rotor

Now, for each section will be determined which part is lying within or outside the upper rotor wake. In hovering flight both the sections are similar. This can be seen in Figure 4.14 and Figure 4.16.
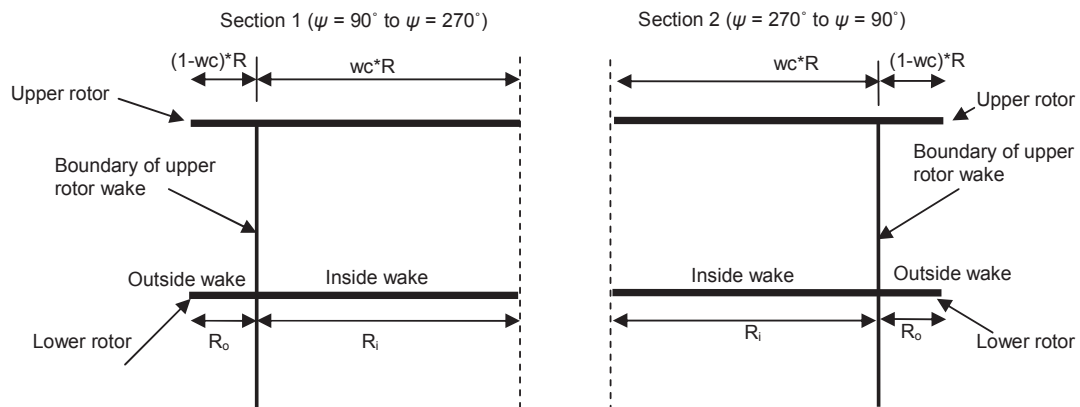

Figure 4.16: Wake geometry in hovering flight for both sections

When the helicopter accelerates to a higher forward speed, the wake skew angle (see Figure 4.13) will increase and consequently the boundary of the upper rotor wake will shift backwards. The various values of the attenuation coefficient in forward flight can be seen in Figure 4.17. One can see the left side of the lower rotor in the left plot of Figure 4.17 and in the right plot one can see the lower rotor surface from above.
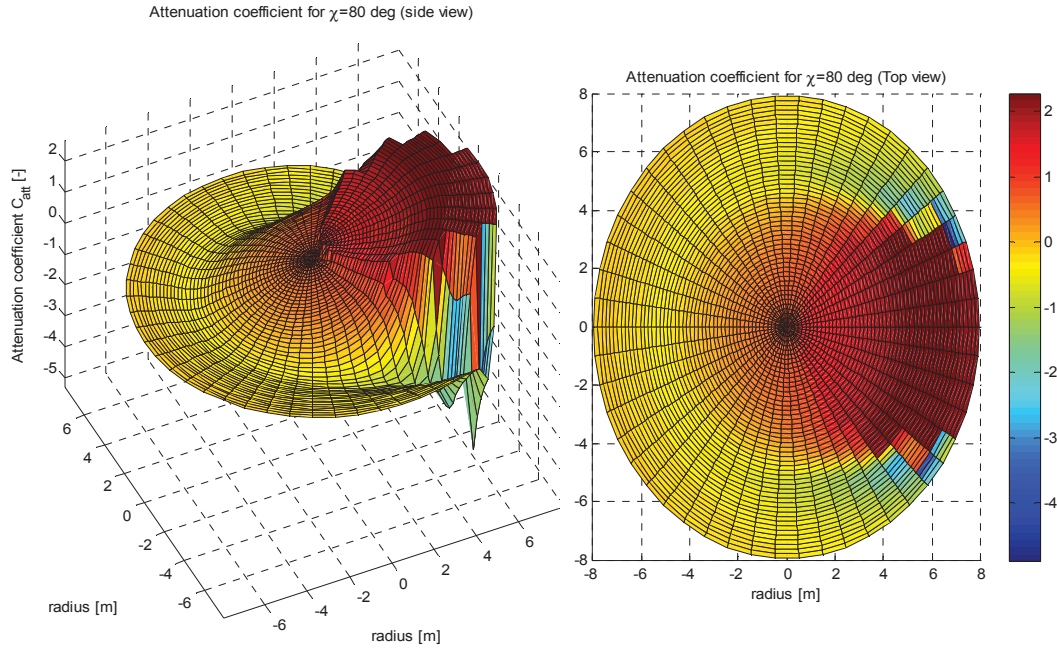
Figure 4.17: Attenuation coefficient in forward flight with wake contraction

An increasing wake skew angle results in an increasing 'outside wake radius' y_o and a decreasing 'inside wake radius' y_i for section 1. The situation on the longitudinal axis of the lower rotor can be seen in Figure 4.18.

Figure 4.18: Possible situations for section 1

As can be seen in Figure 4.18, there are only two different situations for section 1. In the helicopter model the BEM will be applied on section 1 for the following situations:

Situation 1.1: $\quad \chi \le \tan^{-1}\left(\dfrac{wc \cdot R}{H}\right) \Rightarrow R = y_i + y_o$ \hfill (4.22)

Situation 1.2: $\quad \chi > \tan^{-1}\left(\dfrac{wc \cdot R}{H}\right) \Rightarrow R = y_o$ \hfill (4.23)

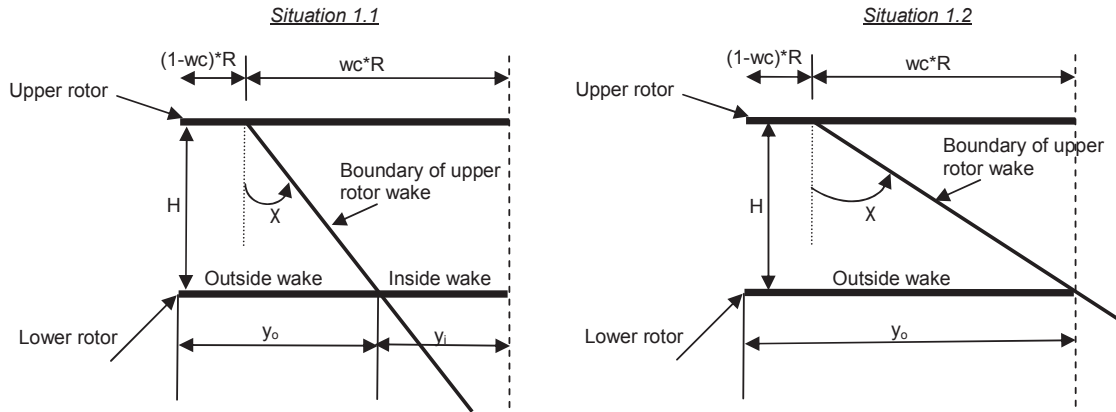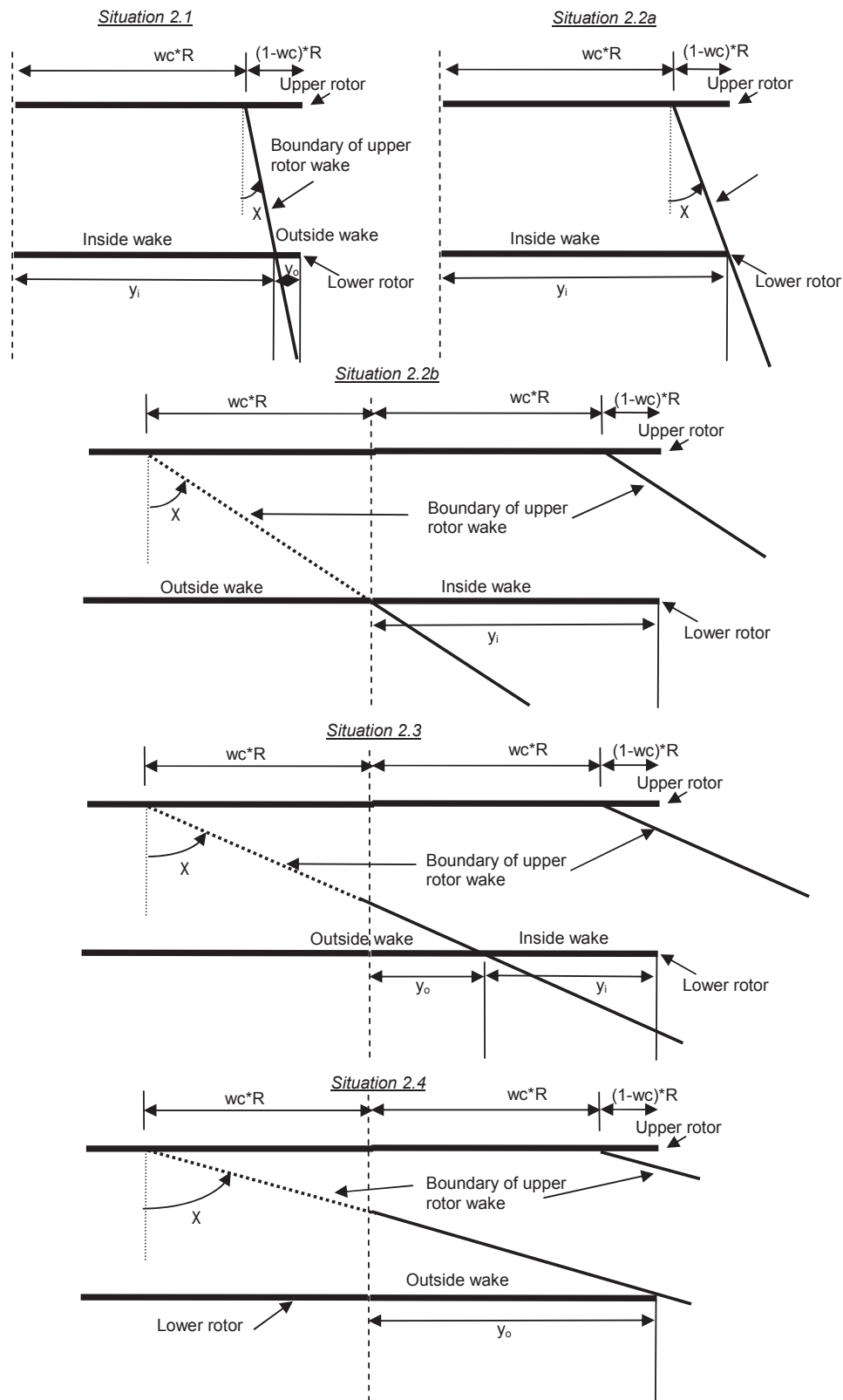The possible situations for section 2 are illustrated in Figure 4.19.

Figure 4.19: Possible situations for section 2

As can be seen in Figure 4.19, there are 4 different possible inflow situations. In the helicopter model the BEM will therefore be applied on section 2 for the following situations:

Situation 2.1: $\chi \leq \tan^{-1}\left(\dfrac{(1-wc)\cdot R}{H}\right) \Rightarrow R = y_i + y_o \;(with\; y_i > y_o)$ (4.24)

Situation 2.2: $\tan^{-1}\left(\dfrac{(1-wc)\cdot R}{H}\right) < \chi \leq \tan^{-1}\left(\dfrac{wc\cdot R}{H}\right) \Rightarrow R = y_i$ (4.25)

Situation 2.3: $\tan^{-1}\left(\dfrac{wc\cdot R}{H}\right) < \chi \leq \tan^{-1}\left(\dfrac{wc\cdot R + R}{H}\right) \Rightarrow R = y_i + y_o$ (4.26)

Situation 2.4: $\chi > \tan^{-1}\left(\dfrac{wc\cdot R + R}{H}\right) \Rightarrow R = y_o$ (4.27)

For situations 1.2, 2.2 and 2.4, there is just one integral that has to be solved to get a particular force (*f*) of the BEM. The method is the same for the T, H, S and Q force (see Appendix B). This can be seen in eq. (4.28) to (4.30).

$$\int_0^R \int_{0.5\pi}^{1.5\pi} f(\lambda_l = \lambda_{0l} + C_{att,outer}\lambda_{0u},..,..)\,d\psi dy \text{ for situation 1.2}$$ (4.28)

$$\int_0^R \int_{1.5\pi}^{2.5\pi} f(\lambda_l = \lambda_{0l} + C_{att,inner}\lambda_{0u},..,..)\,d\psi dy \text{ for situation 2.2}$$ (4.29)

$$\int_0^R \int_{1.5\pi}^{2.5\pi} f(\lambda_l = \lambda_{0l} + C_{att,outer}\lambda_{0u},..,..)\,d\psi dy \text{ for situation 2.4}$$ (4.30)

For the remainder situations one needs to solve two integrals to get a particular force (*f*) of the BEM. The table with the attenuation coefficients will be used to determine whether a section of the lower rotor lies in or out the rotor wake of the upper rotor. This will be done by determining a checkpoint *cp* at a particular radial position in the tabulated C_{att} data. This checkpoint will be different for each situation. At the transition from inside to outside the wake or the other way around, the difference in C_{att} will have its maximum. So, the checkpoint will be positioned at the radial position where the following holds:

$$cp = \max(C_{att\_y+dy} - C_{att\_y})$$ (4.31)

In eq. (4.31), *cp* is equal to a specific position in the tabulated C_{att} data. The position in percentage of the radius can be written as eq. (4.32).

$$cr = \frac{cp}{length(C_{att})}$$ (4.32)

The attenuation coefficient for section 1 and 2 will be determined from the tabulated C_{att} data as the mean value of respectively the radial values of C_{att} at $\psi = \pi$ and $\psi = 2\pi$ (in the longitudinal plane). The radial position of the transition point will be used to make a distinction between the inner and the outer part of the lower rotor surface for each section. This can be seen in eq. (4.33) to (4.36).

$$C_{att,section1,inner} = \overline{C}_{att,section1,inner} = \frac{1}{cp} \sum_{i=0}^{cp} (C_{att}(\psi = \pi))_i \tag{4.33}$$

$$C_{att,section1,outer} = \overline{C}_{att,section1,outer} = \frac{1}{(length(C_{att}) - cp)} \sum_{i=cp}^{length(C_{att})} (C_{att}(\psi = \pi))_i \tag{4.34}$$

$$C_{att,section2,inner} = \overline{C}_{att,section2,inner} = \frac{1}{cp} \sum_{i=0}^{cp} (C_{att}(\psi = 2\pi))_i \tag{4.35}$$

$$C_{att,section2,outer} = \overline{C}_{att,section2,outer} = \frac{1}{(length(C_{att}) - cp)} \sum_{i=cp}^{length(C_{att})} (C_{att}(\psi = 2\pi))_i \tag{4.36}$$

with *i* is a radial position in the tabulated C_{att} value.

For situations 1.2, 2.2 and 2.4, there is only one attenuation coefficients for each section, because the checkpoint *cp* is lying either at *i = 0* or at *i = R (= length(C$_{att}$))*.

The radial position of the transition point will also be used as a boundary for the BEM integrals. This can be seen in eq. (4.37) to (4.39).

$$\int_0^{cr\cdot R} \int_{0.5\pi}^{1.5\pi} f(\lambda_l = \lambda_{0l} + C_{att,section1,inside}\lambda_{0u},...,..)\,d\psi dy + \int_{cr\cdot R}^{R} \int_{0.5\pi}^{1.5\pi} f(\lambda_l = \lambda_{0l} + C_{att,section1,outside}\lambda_{0u},...,..)\,d\psi dy \text{ for 1.1}$$

$$\tag{4.37}$$

$$\int_0^{cr\cdot R} \int_{1.5\pi}^{2.5\pi} f(\lambda_l = \lambda_{0l} + C_{att,section2,inside}\lambda_{0u},...,..)\,d\psi dy + \int_{cr\cdot R}^{R} \int_{1.5\pi}^{2.5\pi} f(\lambda_l = \lambda_{0l} + C_{att,section2,outside}\lambda_{0u},...,..)\,d\psi dy \text{ for 2.1}$$

$$\tag{4.38}$$

$$\int_0^{cr\cdot R} \int_{1.5\pi}^{2.5\pi} f(\lambda_l = \lambda_{0l} + C_{att,section2,outside}\lambda_{0u},...,..)\,d\psi dy + \int_{cr\cdot R}^{R} \int_{1.5\pi}^{2.5\pi} f(\lambda_l = \lambda_{0l} + C_{att,section2,inside}\lambda_{0u},...,..)\,d\psi dy \text{ for 2.3}$$

$$\tag{4.39}$$

The method to determine the BEM forces of the lower rotor on each section for each situation is now known. The wake skew angle *χ* is needed to combine the correct situations with each other. Subsequently the involved forces can be added up to obtain the total forces on the lower rotor.

4.1.6 Determination of the rotor forces and moments

Velocity components

The induced velocity of the upper rotor has a great influence on the lower rotor. This means that the induced velocity of the lower rotor is different on every radius and azimuth angle. Due to this, it is not possible to make use of a uniform inflow method. The blade element method provides a method to calculate the separate forces on each radius and azimuth angle. Using this, one can simply integrate the blade elements as discussed in paragraph 4.1.5. The local velocity components on the blade

element will be calculated in the same way for both the CCR and the CR. The individual forces and velocities on each blade element for a counterclockwise rotating rotor are shown in Figure 4.20.
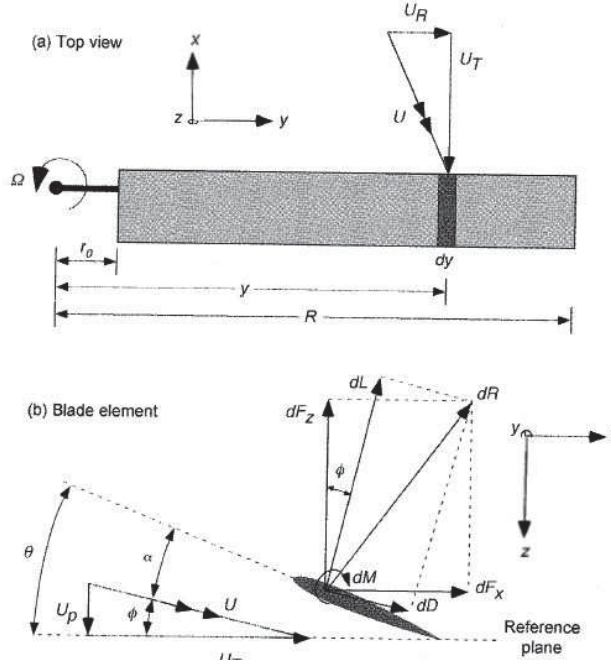

Figure 4.20: Illustration of the blade element (from ref. 39)

As can be seen in Figure 4.20, the local velocity U has three components: U_T in the local x direction, U_R in the local y direction, and U_P in the local z direction. In this thesis, the aerodynamic effects of the radial component U_R will be neglected.

First, the tangential velocity component U_T will be considered. U_T consists of three components: the rotor rotational velocity, which is always in the local x direction, the periodic flight speed in the x direction, the periodic flight speed in the y direction, and the angular velocity around the z axis. U_T can be written as follows (from ref. 29 and 39):

$$U_{Tu}(y,\psi) = U_{Tl}(y,\psi) = \Omega y + u \cdot \sin(\psi) + v \cdot \cos(\psi) + r \cdot y \qquad (4.40)$$

The local tangential velocity will be calculated in the same way for both rotors, but because of the change of retreating and advancing side of the rotor as can be seen in Figure 4.1 and Figure 4.2, U_T will be equal in modulus and will have an opposite direction.

The perpendicular velocity component U_P consists of the flight speed in the z direction, the induced velocity, the angular velocities around the x and y axis, and the periodic flight speeds, which are under influence of the flapping angle β. This can be seen in Figure 4.21.
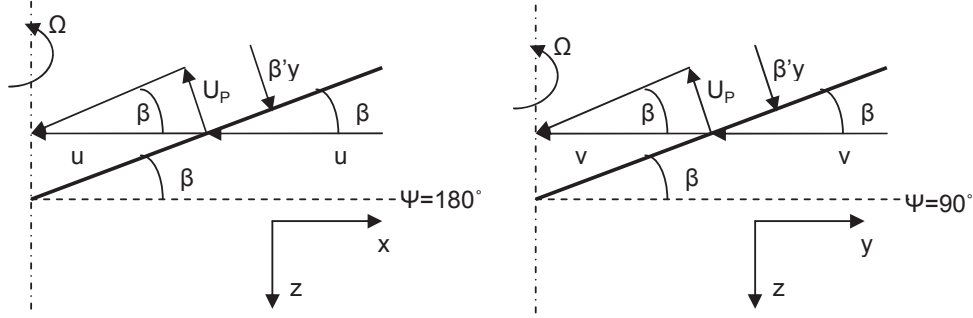
Figure 4.21: The influence of the flap angle to the blade element velocities

The equation for the perpendicular velocity component can now be seen in eq. (4.41) (from ref. 29 and 39).

$$U_{Pu}(y,\psi) = -w + (\lambda_{iu} + \lambda_{cu}) \cdot \Omega R + \dot{\beta}y - p \cdot y \cdot \sin(\psi) - q \cdot y \cdot \cos(\psi) + u\sin(\beta) \cdot \cos(\psi) + v\sin(\beta) \cdot \sin(\psi)$$

(4.41)

Assuming small angles for β, eq. (4.41) becomes:

$$U_{Pu}(y,\psi) = -w + (\lambda_{iu} + \lambda_{cu}) \cdot \Omega R + \dot{\beta}y - p \cdot y \sin(\psi) - q \cdot y \cos(\psi) + u\beta\cos(\psi) + v\beta\sin(\psi)$$ (4.42)

The perpendicular velocity component of the CR will be equal to eq. (4.42), with its own induced velocity included. So, the perpendicular velocity component of the lower rotor is given by

$$U_{Pl}(y,\psi) = -w + (\lambda_{il} + \lambda_{cl}) \cdot \Omega R + \dot{\beta}y - p \cdot y \sin(\psi) - q \cdot y \cos(\psi) + u\beta\cos(\psi) + v\beta\sin(\psi)$$

(4.43)

Incremental forces on a blade element for a CCR

There are two aerodynamic forces acting on a blade element: the incremental lift force *dL* and the incremental drag force *dD* as can be seen in Figure 4.20. As stated in paragraph 4.1.2, the reference plane to be considered is the tip path plane (TPP). The elementary aerodynamic forces can be decomposed as can be seen in Figure 4.22.

Before the elementary forces in the *x* (*dH*), *y* (*dS*), and *z* (*dT*) direction can be determined, the blade forces *dD* and *dL* have to be determined first. The relative inflow angle at the blade element is for small angles equal to

$$\phi = \tan^{-1}\left(\frac{U_P}{U_T}\right) \approx \frac{U_P}{U_T}$$

(4.44)

Because the perpendicular velocity on the blade is small relative to the tangential velocity, the resultant velocity can be approximated by *U_T*.

Now, the incremental lift force on a blade element is given by (ref. 39 and 47)

$$dL = \frac{1}{2}\rho U^2 c C_l dy = \frac{1}{2}\rho U_{Tu}^2 c C_{l\alpha}(\theta - \phi)dy$$

(4.45)

and the incremental drag is given by

$$dD = \frac{1}{2}\rho U^2 c C_d dy = \frac{1}{2}\rho U_{Tu}^2 c C_d dy \qquad (4.46)$$
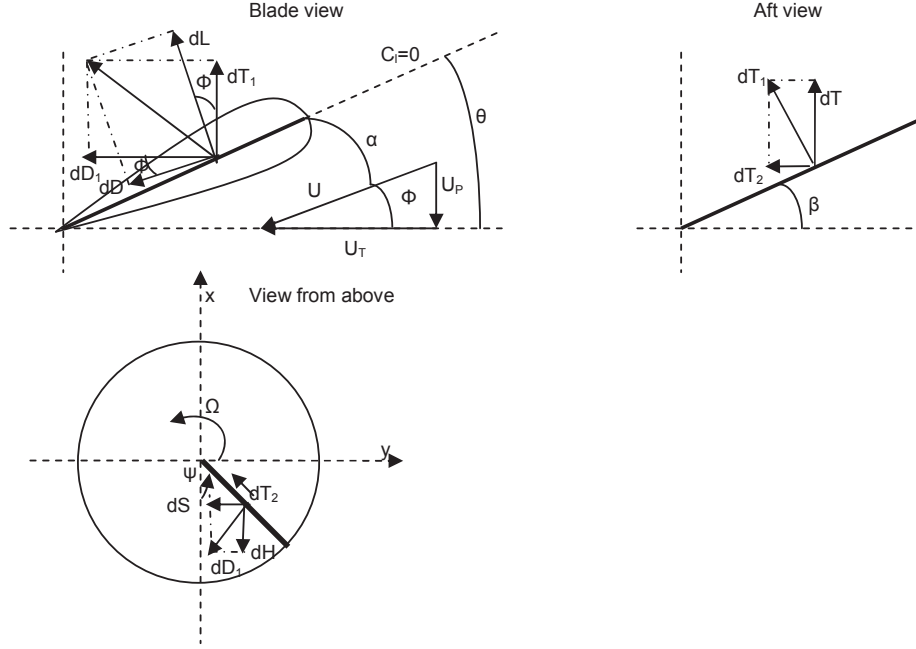

Figure 4.22: Forces on a blade element (ref. 47)

The incremental lift and drag can be decomposed following Figure 4.22 to get the drag force dD_1 parallel to the control plane (CP) and the thrust force dT_1 perpendicular to the blade. Assuming small inflow angles, the following equations can be written: (from ref. 47)

$$dT_1 = dL\cos(\phi) - dD\sin(\phi) \approx dL - dD\phi \approx dL \qquad (4.47)$$

$$dD_1 = dL\sin(\phi) + dD\cos(\phi) \approx dL\phi + dD \qquad (4.48)$$

Due to the flap angle β, the thrust force dT_1 can be decomposed following Figure 4.22 to get the thrust force dT perpendicular to the CP and dT_2 parallel to the CP.

$$dT_2 = dT_1\sin\beta \approx dL\beta \qquad (4.49)$$

$$dT_u = dT_1\cos(\beta) \approx dT_1 \approx dL \qquad (4.50)$$

Now the elementary forces in the x (dH) and y (dS) direction can be determined.

$$dH_u = dD_1\sin(\psi) - dT_2\cos(\psi) \qquad (4.51)$$

$$dS_u = dD_1\cos(\psi) + dT_2\sin(\psi) \qquad (4.52)$$

Finally, the elementary torque moment about the z axis can be seen in eq. (4.53).

$$dQ_u = y\,dD_1 \qquad (4.53)$$

The total forces in the CP can now be determined by integrating the incremental forces over the whole radius and azimuth angle. The thrust force T_u, longitudinal force H_u, lateral force S_u, and the torque

moment Q_u can be seen in eq. (4.54) to (4.57). The total derivation of the forces on the upper rotor can be found in the digital appendix.

$$T_u = \frac{N_b}{2\pi} \int_0^R \int_0^{2\pi} dT_u \tag{4.54}$$

$$H_u = \frac{N_b}{2\pi} \int_0^R \int_0^{2\pi} dH_u \tag{4.55}$$

$$S_u = \frac{N_b}{2\pi} \int_0^R \int_0^{2\pi} -dS_u \tag{4.56}$$

$$Q_u = \frac{N_b}{2\pi} \int_0^R \int_0^{2\pi} dQ_u \tag{4.57}$$

The minus sign in eq. (4.57) is taken to obtain a S-force in the positive y direction.

Incremental forces on a blade element for a CR

The incremental forces on the blade element for a CR will be calculated in the same way as for a CCR. The only difference appears at the lateral force S and the torque moment Q. S as well as Q are acting in the opposite direction. The incremental forces can now be determined for a CR in the same way as for a CCR.

$$dT_l = dT_1 \cos(\beta) \approx dT_1 \approx dL \tag{4.58}$$

$$dH_l = dD_1 \sin(\psi) - dT_2 \cos(\psi) \tag{4.59}$$

$$dS_l = -dD_1 \cos(\psi) - dT_2 \sin(\psi) \tag{4.60}$$

$$dQ_l = -ydD_1 \tag{4.61}$$

The total forces in the CP can now be determined by integrating the incremental forces over the whole radius and azimuth angle. This is in fact a summation of the different situations which are defined in paragraph 4.1.5. The total thrust force T_l, longitudinal force H_l, lateral force S_l, and the torque moment Q_l can be seen in eq. (4.62) to (4.65). The total derivation of the forces on the lower rotor can be found in the digital appendix.

$$T_l = \frac{N_b}{2\pi} \int_0^R \int_0^{2\pi} dT_l \tag{4.62}$$

$$H_l = \frac{N_b}{2\pi} \int_0^R \int_0^{2\pi} dH_l \tag{4.63}$$

$$S_l = \frac{N_b}{2\pi} \int_0^R \int_0^{2\pi} dS_l \tag{4.64}$$

$$Q_l = \frac{N_b}{2\pi} \int_0^R \int_0^{2\pi} dQ_l \tag{4.65}$$

Total rotor forces and moments

In the previous paragraph, the rotor forces have been calculated in the CP. In order to know the contribution of these rotor forces on the helicopter body, the rotor forces need to be converted to a rotor plane which is connected to the body. As can be seen in Figure 4.3, the shaft plane (SP) is directly connected to the shaft and to the body.
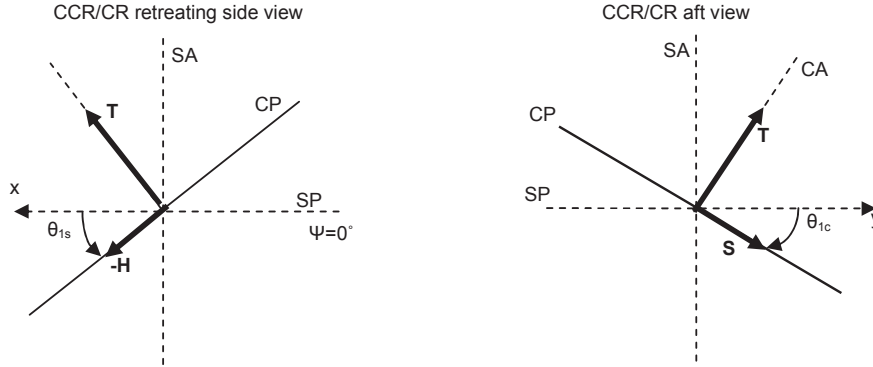

Figure 4.23: Relation of the forces in CP and SP

Using Figure 4.23, it is easy to determine the total forces in *X, Y,* and *Z* direction in the SP.

$$X_u = T_u \sin(\theta_{1s}) - H_u \cos(\theta_{1s})$$
$$Y_u = T_u \sin(\theta_{1c}) - S_u \cos(\theta_{1c}) \quad (4.66)$$
$$Z_u = -T_u \cos(\theta_{1s})\cos(\theta_{1c}) - H_u \sin(\theta_{1s}) + S_u \sin(\theta_{1c})$$

and for the lower rotor:

$$X_l = T_l \sin(\theta_{1s}) - H_l \cos(\theta_{1s})$$
$$Y_l = T_l \sin(\theta_{1c}) - S_l \cos(\theta_{1c}) \quad (4.67)$$
$$Z_l = -T_l \cos(\theta_{1s})\cos(\theta_{1c}) - H_l \sin(\theta_{1s}) + S_l \sin(\theta_{1c})$$

The rotor moments for the upper and lower rotor are now given by

$$L_u = Y_u z_u - Z_u y_u$$
$$M_u = -X_u z_u - Z_u x_u \quad (4.68)$$
$$N_u = Q_u$$

$$L_l = Y_l z_l - Z_l y_l$$
$$M_l = -X_l z_l - Z_l x_l \quad (4.69)$$
$$N_l = Q_l$$

4.2 Other helicopter forces

Beside the rotor forces several other forces will act on the helicopter. The three most important other forces are produced by the fuselage, the horizontal tail plane and the vertical tail plane.

4.2.1 Fuselage forces and moments

In forward flight the helicopter fuselage will cause an amount of parasite drag. For a fixed wing airplane the parasite drag can simply be expressed as a function of the drag coefficient and a reference area. In case of a helicopter it is not that simple to determine the reference area. For this reason the equivalent flat plate area has been used. The equivalent flat plate area *f* is the frontal area of a flat plate with a drag coefficient of 1, which has the same drag as the fuselage that has to be estimated. The parasite drag can be estimated either by adding up the various components that are creating the drag based on theory or by wind tunnel testing. The main rotor hub and shaft give a considerable contribution to the total equivalent flat plate area. Consequently, a coaxial rotor configuration has a substantially higher equivalent flat plate area than a single rotor configuration. Normally, knowing the helicopter gross weight, it is easy to estimate the equivalent flat plate area by using test data from other helicopters. Because of the lack of experimental data of a coaxial helicopter and the great contribution of the main rotor hub and shaft to the total equivalent flat plate area, the equivalent flat plate area of a tandem rotor configuration (CH-47) will be used. The angle of attack and sideslip angle of the fuselage are needed in order to determine the fuselage drag forces in the different directions in the body fixed reference frame. These angles are given by

$$\alpha_{fus} = \tan^{-1}(w/u)$$
$$\beta_{fus} = \tan^{-1}(v/u)$$

(4.70)

The fuselage drag forces are now given by (ref. 24)

$$X_{fus} = -\frac{1}{2}\rho V^2 f \cos(\alpha_{fus})\cos(\beta_{fus})$$

$$Y_{fus} = -\frac{1}{2}\rho V^2 f \sin(\beta_{fus})$$

(4.71)

$$Z_{fus} = -\frac{1}{2}\rho V^2 f \sin(\alpha_{fus})$$

For the fuselage, only the moment about the *y* axis will be used and is given by (ref. 24)

$$M_{fus} = \rho V^2 k_{fus} Vol_{fus}\alpha_{fus}$$

(4.72)

4.2.2 Horizontal stabilizer

To give the helicopter stability in pitch, a horizontal stabilizer is required. In this helicopter model only the force in *z* direction and the moment about the *y* (pitching) axis will be considered. The local velocity at the horizontal stabilizer is equal to (ref. 24)

$$V_{hs} = \sqrt{u^2 + (w + q \cdot x_{hs})^2}$$

(4.73)

The force in *z* direction due to the horizontal stabilizer is given by (ref. 24)

$$Z_{hs} = -\frac{1}{2}\rho V_{hs}^2 S_{hs} C_{lhs} = -\frac{1}{2}\rho V_{hs}^2 S_{hs} C_{l\alpha hs}\alpha_{hs}$$

(4.74)

with

$$\alpha_{hs} = \alpha_{0hs} + \tan^{-1}(\frac{w + q \cdot x_{hs}}{u})$$

(4.75)

The pitching moment of the horizontal stabilizer is given by

$$M_{hs} = Z_{hs} \cdot x_{hs}$$

(4.76)

4.2.3 Vertical stabilizer

To give the helicopter more stability in yaw, a vertical stabilizer or fin is required. In this helicopter model only the force in y direction and the moment about the x (rolling) and z (yawing) axis will be considered. The local velocity at the vertical stabilizer is equal to (ref. 24)

$$V_{vs} = \sqrt{u^2 + (v - r \cdot x_{vs} + p \cdot z_{vs})^2}$$

(4.77)

The force in Y direction due to the vertical stabilizer is given by (ref. 24)

$$Y_{vs} = -\frac{1}{2}\rho V_{vs}^2 S_{vs} C_{lvs} = -\frac{1}{2}\rho V_{vs}^2 S_{vs} C_{l\alpha hs}\beta_{hs}$$

(4.78)

with

$$\beta_{vs} = \beta_{0vs} + \tan^{-1}(\frac{v - r \cdot x_{vs} + p \cdot z_{vs}}{u})$$

(4.79)

The moments of the vertical stabilizer are given by

$$\begin{aligned} L_{vs} &= Y_{vs} \cdot z_{vs} \\ N_{vs} &= -Y_{vs} \cdot x_{vs} \end{aligned}$$

(4.80)

4.3 Total helicopter forces and moments

The total aerodynamic forces and moments acting on the coaxial helicopter consist of the sum of the rotor forces and moments, fuselage forces and moments, and the stabilizer forces and moments. Eq. (4.81) gives the summation of all aerodynamic forces which are determined earlier in this chapter.

$$\begin{aligned} X &= X_u + X_l + X_{fus} \\ Y &= Y_u + Y_l + Y_{fus} + Y_{vs} \\ Z &= Z_u + Z_l + Z_{fus} + Z_{hs} \end{aligned}$$

(4.81)

To determine the total helicopter forces in the body reference frame, the helicopter weight has to be included. The total forces are now given by (ref. 47)

$$\begin{aligned} F_x &= -W\sin(\theta_f) + X \\ F_y &= W\cos(\theta_f)\sin(\phi_f) + Y \\ F_z &= W\cos(\theta_f)\cos(\phi_f) + Z \end{aligned}$$

(4.82)

Eq. (4.83) gives the summation of all aerodynamic moments which are determined earlier in this chapter.

$$\begin{aligned} L &= L_u + L_l + L_{vs} \\ M &= M_u + M_l + M_{fus} + M_{hs} \\ N &= N_u + N_l + N_{vs} \end{aligned}$$

(4.83)

4.4 Formulation of the equations of motion

Now the total forces and moments on the helicopter are known, the equations of motion of the helicopter can be formulated for the translations (ref. 47):

$$\dot{u} = \frac{F_x}{m} + rv - qw$$

$$\dot{v} = \frac{F_y}{m} - ru + pw \tag{4.84}$$

$$\dot{w} = \frac{F_z}{m} - qu + pv$$

and for the rotations (ref. 47):

$$\dot{p} = \frac{(I_{yy}I_{zz} - I_{zz}^2 - J_{xz}^2)rq + (I_{xx} - I_{yy} + I_{zz})J_{xz}pq + I_{zz}L + J_{xz}N}{I_{xx}I_{zz} - J_{xz}^2}$$

$$\dot{q} = \frac{M + (I_{zz} - I_{xx})pr - J_{xz}(r^2 - p^2)}{I_{yy}} \tag{4.85}$$

$$\dot{r} = \frac{(I_{xx}^2 - I_{xx}I_{yy} + J_{xz}^2)pq - (I_{xx} - I_{yy} + I_{zz})J_{xz}qr + J_{xz}L + I_{xx}N)}{(I_{xx}I_{zz} - J_{xz}^2)}$$

The orientation with respect to the earth's inertial reference frame are defined as follows (ref. 24):

$$\dot{\psi} = \frac{(q\sin(\phi) + r\cos(\phi))}{\cos(\theta)}$$

$$\dot{\theta} = q\cos(\phi) - r\sin(\phi) \tag{4.86}$$

$$\dot{\phi} = p + \dot{\psi}\sin(\theta)$$

The velocities in the earth's inertial reference frame are calculated by (ref. 24)

$$\dot{x} = (u\cos(\theta) + (v\sin(\phi) + w\cos(\phi))\sin(\theta))\cos(\psi) - (v\cos(\phi) - w\sin(\phi))\sin(\psi)$$

$$\dot{y} = (u\cos(\theta) + (v\sin(\phi) + w\cos(\phi))\sin(\theta))\sin(\psi) + (v\cos(phi) - w\sin(\phi))\cos(\psi) \tag{4.87}$$

$$\dot{z} = -u\sin(\theta) + (v\sin(\phi) + w\cos(\phi))\cos(\theta)$$

The induced velocities of both rotors will be treated as state variables and therefore two new equations based on "quasi-dynamic inflow" will be introduced (ref. 46):

$$\dot{\lambda}_{iu} = \frac{C_{Tu}^{elem} - C_{Tu}^{gl}}{\tau_\lambda} \tag{4.88}$$

$$\dot{\lambda}_{il} = \frac{C_{Tl}^{elem} - C_{Tl}^{gl}}{\tau_\lambda} \tag{4.89}$$

The thrust coefficient according to Glauert is given by (from ref. 46):

$$C_T^{gl} = 2\lambda_i\sqrt{(\mu\cos(\alpha_{cp} - a_1))^2 + (\mu\sin(\alpha_{cp} - a_1) + \lambda_i)^2} \tag{4.90}$$

The induced velocity of the lower rotor to determine the thrust coefficient according to Glauert is calculated as the mean value of the induced velocities of the different situations.

4.4.1 Implementation in Matlab

The discussed equations in this chapter will be implemented in Matlab in order to derive the trim condition as well as the dynamic response of the coaxial helicopter. A description of the content and working principle of the different Matlab routines can be found in Appendix B.

The Matlab routine uses 14 state variables and 4 controls variables to either determine the trim condition and the dynamic response.

The state variables are

$$x = [u \ v \ w \ p \ q \ r \ \psi_f \ \theta_f \ \phi_f \ x \ y \ z \ \lambda_{0u} \ \lambda_{0l}]^T \tag{4.91}$$

And the control variables are

$$u = [\theta_{0u} \ \theta_{0l} \ \theta_{1s} \ \theta_{1c}]^T \tag{4.92}$$

5 Coaxial helicopter trim

The method to achieve the trim condition will be described in this chapter and subsequently the trim results will be discussed. Also some power calculations have been made to make a comparison between the simulated data and the real coaxial helicopter.

5.1 Defining the trim condition

In this thesis the trim condition for a straight forward flight will be determined. In order to obtain a trimmed state of the helicopter for a given forward speed, it requires that the time derivatives of all state variables as can be seen in eq. (4.91) except the velocities in the earth inertial reference frame are zero. If the angular velocities are zero, the time derivatives of the attitude angles are automatically zero as well, so the set of time derivatives that have to equal zero is now reduced to eq. (5.1).

$$f = [\dot{u} \ \dot{v} \ \dot{w} \ \dot{p} \ \dot{q} \ \dot{r} \ \dot{\lambda}_{0u} \ \dot{\lambda}_{0l}]^T \tag{5.1}$$

The following set of trim variables will be used to obtain a certain trim condition.

$$g = [\theta_f \ \phi_f \ \theta_{0u} \ \theta_{0l} \ \theta_{1s} \ \theta_{1c} \ \lambda_{0u} \ \lambda_{0l}]^T \tag{5.2}$$

As can be seen in eq. (5.2) the number of trim variables is equal to the number time derivatives that need to be zero.

The Newton iteration method (see eq. (5.3)) will be used to find the trimmed values of vector *g*. It calculates a state vector *f* with a given initial condition and subsequently changes alternately every trim variable of *g* to determine the effect on each state of *f*. These effects (partial derivatives) will form a Jacobian matrix *J*. The inverse of the Jacobian matrix will be used to determine a new condition of trim variables which will serve as a new input for the next iteration step. This will be repeated until all the elements of the state vector *f* are equal to zero.

The Newton iteration method:

$$g_{n+1} = g_n - \frac{f(g_n)}{f'(g_n)} \tag{5.3}$$

 The Newton iteration method for a non-linear system of equations:

$$\begin{pmatrix} g_{1_{n+1}} \\ g_{2_{n+1}} \\ .. \end{pmatrix} = \begin{pmatrix} g_{1_n} \\ g_{1_n} \\ .. \end{pmatrix} - \begin{pmatrix} \dfrac{\partial f_{1_n}}{\partial g_{1_n}} & \dfrac{\partial f_{1_n}}{\partial g_{2_n}} & .. \\ \dfrac{\partial f_{2_n}}{\partial g_{1_n}} & \dfrac{\partial f_{2_n}}{\partial g_{2_n}} & .. \\ .. & .. & .. \end{pmatrix}^{-1} \begin{pmatrix} f_1(g_n) \\ f_2(g_n) \\ .. \end{pmatrix} = \begin{pmatrix} g_{1_n} \\ g_{1_n} \\ .. \end{pmatrix} - J^{-1} \begin{pmatrix} f_1(g_n) \\ f_2(g_n) \\ .. \end{pmatrix} \tag{5.4}$$

5.2 Trim results and validation

5.2.1 Controls and states

Because there is very little information available about coaxial helicopters, it is not easy to validate the obtained data from the coaxial simulation model. As discussed earlier in paragraph 3.4, the Ka-32 can be compared with the Puma single rotor helicopter in view of dimensions. To determine whether the simulated data are fairly reasonable data, the trim data will be compared with a numerical blade element model "MoGeHM" (ref. 55) for the Puma and with Puma trim measurements performed by the South African Air Force (ref. 30). Also the trim results without the mutual interference between the rotors are plotted to see what the effect is of the rotor interference. This is of course a hypothetical situation.
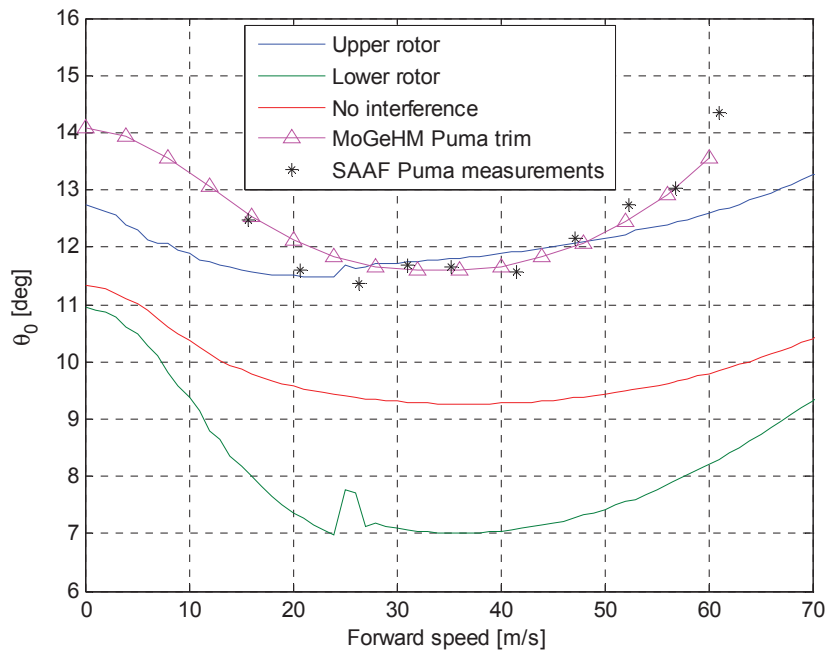

Figure 5.1: Collective pitch angle in trimmed forward flight

Collective pitch

As can be seen in Figure 5.1, both upper and lower rotor collective pitch angle graph show the same bucket shape as the Puma models. The "no interference" line, which represents the collective pitch angle for both upper and lower rotor when there would be no mutual interference between the rotors, is somewhere between the two separate rotor lines from about 10 m/s, which coincides with the expectations.

The lower rotor acts in the downwash field of the upper rotor. This means that the isolated lower rotor has to produce less thrust than the isolated upper rotor. In other words, the collective pitch angle of the lower rotor, which influences the thrust, has to be smaller in comparison with the one of the upper

rotor. Also Nagashima (ref. 42) proved this expectation in his article. Figure 5.1 shows indeed a smaller collective pitch angle at each forward speed.

When looking closely to Figure 5.1 three remarkable effects can be distinguished which occur at about *V = 7 m/s*, *V = 25 m/s*, and *V = 53 m/s* . These effects are probably the result of the following model deficiencies:

1. The attenuation coefficient has been approximated in the longitudinal axis.
2. The discrete behavior of the situation switch as explained in paragraph 4.1.5.

To explain above model shortcomings further, the collective pitch angle will be plotted again, together with the wake skew angle in Figure 5.2. Also the wake skew angles of the situation switches will be determined to see whether there exists a relationship between the situation switches and the discrepancy in Figure 5.1.

Assuming a wake contraction of 0.85 as has been determined in eq. (4.15), it is possible to calculate the wake skew angle during the switch from situation 2.1 to situation 2.2 (see Figure 4.19 and eq. (4.24)):

$$\chi = \tan^{-1}\left(\frac{(1-wc)\cdot R}{H}\right) = \tan^{-1}\left(\frac{(1-0.85)\cdot 7.95}{0.189\cdot 7.95}\right) = 38.44 \text{ deg} \qquad (5.5)$$

The first discrepancy can be seen at *V = 7 m/s*. Figure 5.2 shows that the wake skew angle at this forward speed is approximately equal to 38 deg and this is indeed the wake skew angle of the switch between situation 2.1 and situation 2.2. To explain this discrepancy further, the situation will be considered from above in order to make a good visualization of the situation. This can be seen in Figure 5.3.
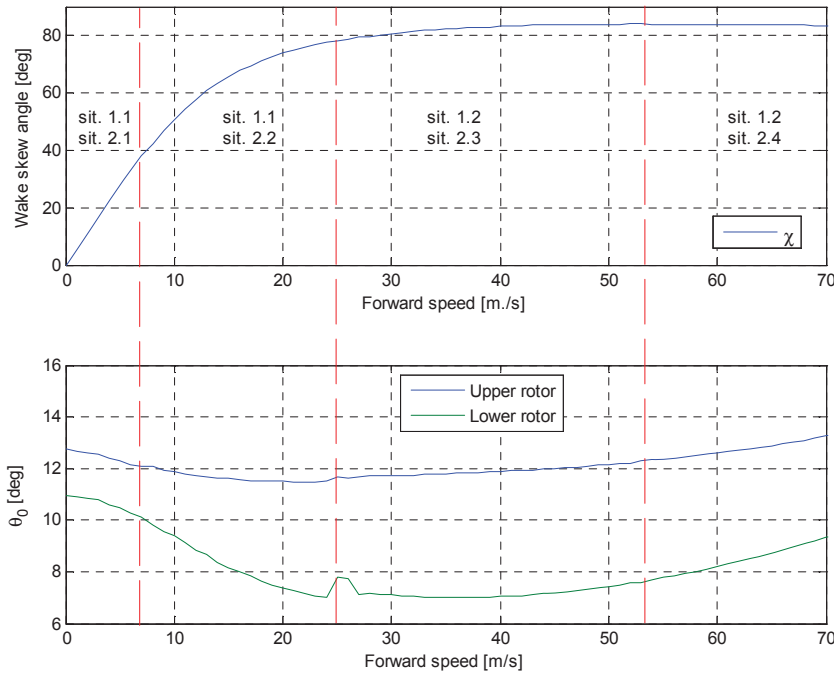

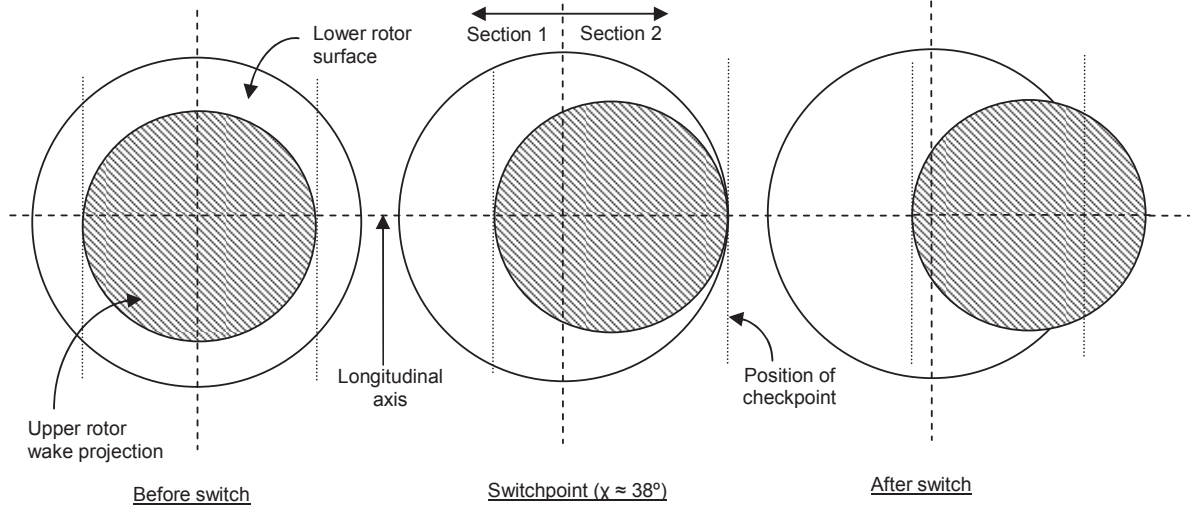**Figure 5.2: Relation between wake skew angle and collective pitch**

Figure 5.3: Situation sketch around first switchpoint

As can be seen in Figure 5.3, the radial checkpoint of section 2 at the switchpoint is positioned at $cp = R$. However, in the real case this is the only azimuth angle ($\psi = 0$) where the upper rotor wake covers whole section 2. At the remainder azimuth angles of section 2 still holds: $R = y_i + y_o$ with $y_i = cp$ and $y_o = (R - cp)$. To get a better approximation of the real case, the radial checkpoint, the corresponding attenuation coefficient and subsequently the BEM integral should be determined for each azimuth angle. This will require a lot of calculations, therefore the attenuation coefficient will only be determined at the longitudinal axis in this report. Because of this simplification and because the situation switch appears quite abrupt, there exists a discrepancy at $\chi = 38°$ and thus on $V = 8$ m/s.

The next situation switch appears at the following wake skew angle (see Figure 4.18, Figure 4.19, eq. (4.25) and eq. (4.22):

$$\chi = \tan^{-1}\left(\frac{wc \cdot R}{H}\right) = \tan^{-1}\left(\frac{0.85 \cdot 7.95}{0.189 \cdot 7.95}\right) = 77.46 \text{ deg} \qquad (5.6)$$

Looking at Figure 5.2, this is indeed the wake skew angle where the next and largest discrepancy in collective pitch angle appears.
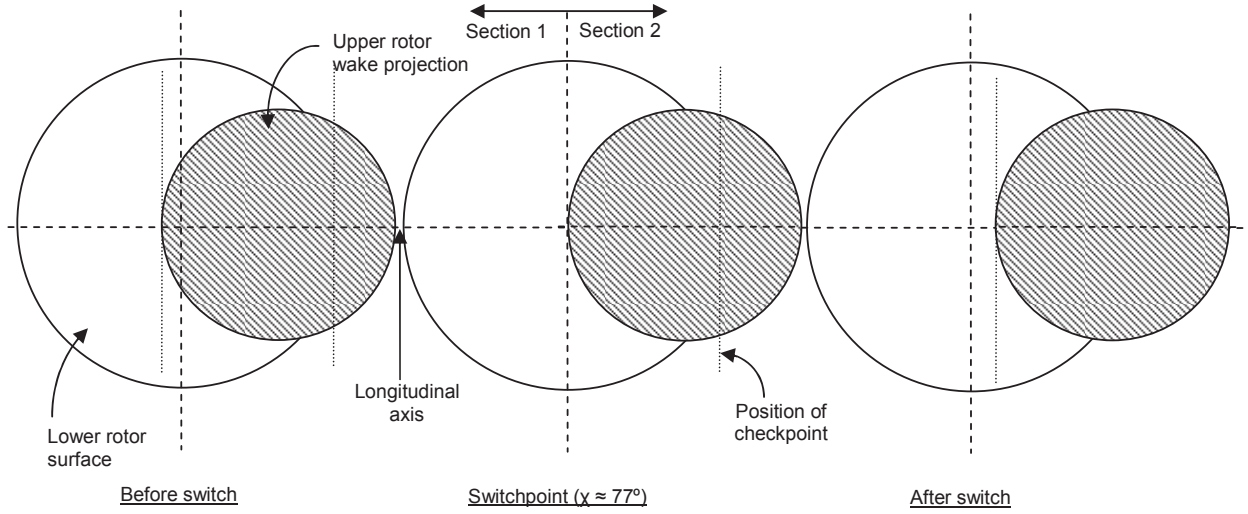
Figure 5.4: Situation sketch around second switchpoint

This large discrepancy can be attributed to the fact that at $\chi \approx 77°$ there appears a situation switch for both sections. This can be seen in Figure 5.4. Before the switch, section 1 was considered to lie inside the upper rotor wake for some part, whereas a big part of section 1 was already lying completely outside the upper rotor wake. After the switch, section 1 lies completely outside the upper rotor wake and therefore the approximation of the attenuation coefficient will be quite correct.

Before the switch has taken place, section 2 lies completely inside the upper rotor wake. After the switch, the inner part of section 2 is lying outside the upper rotor wake and the outer part is lying inside the upper rotor wake. This is good approximated by the checkpoint, but with an overestimation of the outer part of the lower rotor. This is due to the fact that the checkpoint approximates the section to lie inside the upper rotor wake, whereas at larger azimuth angles the section is lying outside the upper wake for a large part. This can be seen in Figure 5.4 after the switch. Because of all this, there exists a discrepancy at $\chi \approx 77°$ and thus on $V \approx 25\ m/s$.

The last situation switch appears at the following wake skew angle (see Figure 4.19 and eq. (4.27)):

$$\chi = \tan^{-1}\left(\frac{(wc \cdot R) + R}{H}\right) = \tan^{-1}\left(\frac{(0.85 \cdot 7.95) + 7.95}{0.189 \cdot 7.95}\right) = 84.17\ \text{deg} \qquad (5.7)$$

Looking at Figure 5.2, this is indeed the wake skew angle where the next discrepancy in collective pitch angle appears. At $\chi \approx 84°$ and thus on $V \approx 53\ m/s$, the upper rotor wake leaves the lower rotor completely after which the lower rotor lies entirely outside the upper rotor wake. Because this transition is approximated quite well by the model (see Figure 5.5), the effect on the collective pitch angles in Figure 5.2 is not large.
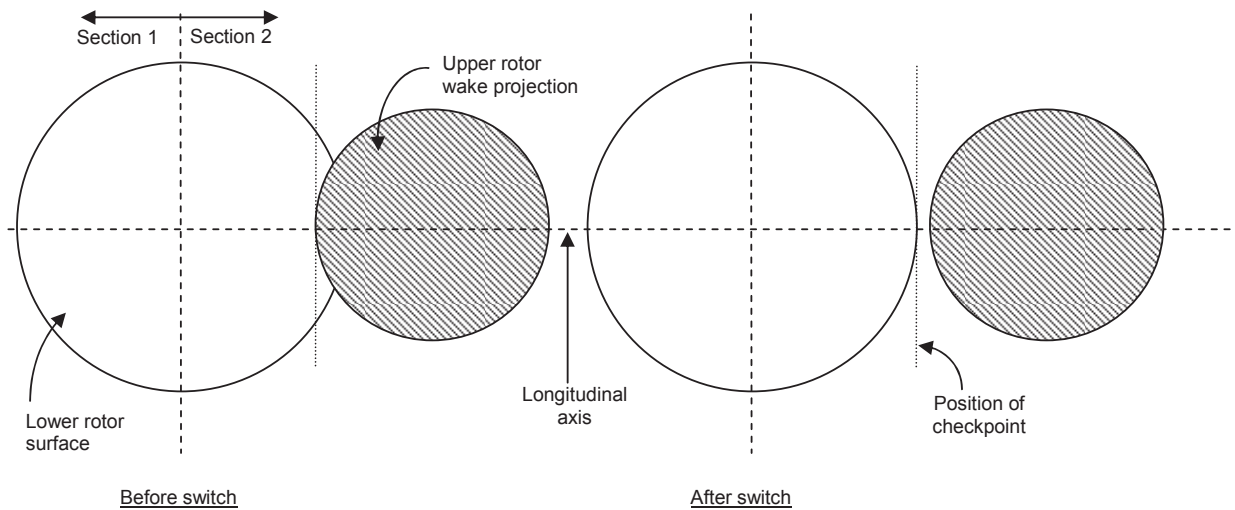
Section 1   Section 2

Upper rotor
wake projection

Lower rotor
surface

Longitudinal
axis

Position of
checkpoint

Before switch   After switch

Figure 5.5: Situation sketch around last switchpoint

Lateral cyclic pitch

As discussed earlier in paragraph 3.2, a very important characteristic of the coaxial helicopter is that there exists no cross-coupling between the longitudinal and lateral movement. So, in theory the lateral cyclic pitch angle of both rotors should be zero when the helicopter is performing a straight forward flight. As can be seen in Figure 5.6 this is indeed the situation for the hypothetical "no interference" case. However, for the simulated coaxial helicopter with mutual interference between the rotors, the lateral cyclic pitch shows a "strange behavior" in the first *25 m/s*. The reason for this behavior can be attributed to the strong influence of the upper rotor on the lower rotor, especially in the first 25 *m/s*. Apparently the interference between the rotors influences the lateral behavior of the helicopter and therefore the helicopter has to correct the influence from the upper rotor wake with the lateral cyclic pitch. After the second switchpoint (see Figure 5.4) the influence of the upper rotor is so low that there is no need to compensate with the lateral cyclic pitch. Therefore the lateral cyclic pitch of the coaxial helicopter will be almost zero for forward speeds above 25 *m/s*. This can clearly be seen in Figure 5.6.

Longitudinal cyclic pitch

The longitudinal cyclic pitch has been plotted against the forward speed in Figure 5.7. As expected, the longitudinal cyclic pitch angle will increase by increasing forward speed. The good correlation between the coaxial rotor and the "no interference" situation at low speeds attracts immediately the attention. Apparently the mutual interference between the rotors does affect the longitudinal pitch angle only at higher forward speeds. The reason for the vertical shift between the simulated coaxial data and the Puma data can be attributed to the fact that the position of the center of gravity of both helicopters differs. The difference can also lie in the manner how the control angles are measured. If the control angles are measured close to the pilot, this can result in errors in comparison with the ideal case where the controls angles are measured at blade pitch bearings. Furthermore, it has to be kept in mind that a Puma helicopter is really another helicopter type. To decide properly whether the coaxial

rotor data and the Puma data show the same trend, the longitudinal cyclic pitch has been plotted again in Figure 5.8 without the vertical shift. Here it is easy to see that the coaxial helicopter needs much less longitudinal pitch to fly the same forward speed than a single rotor helicopter.
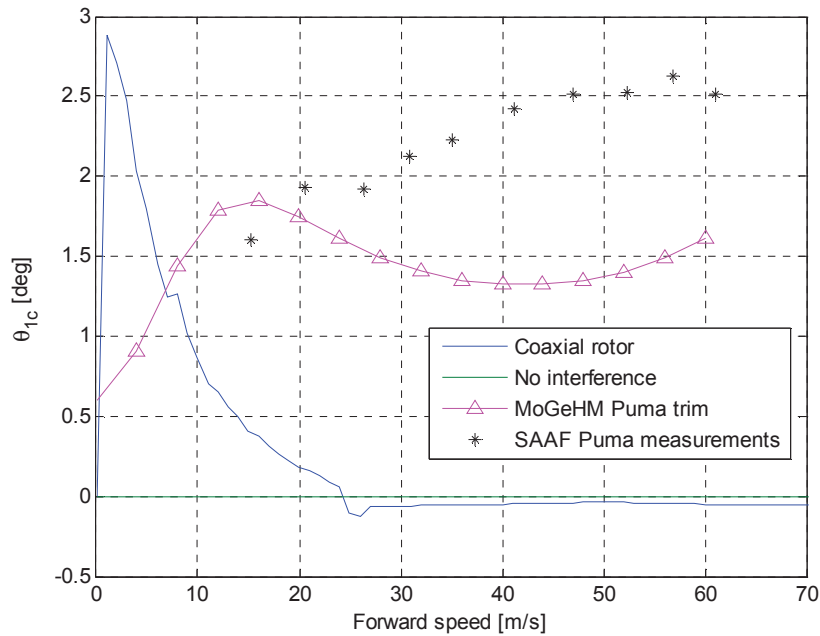

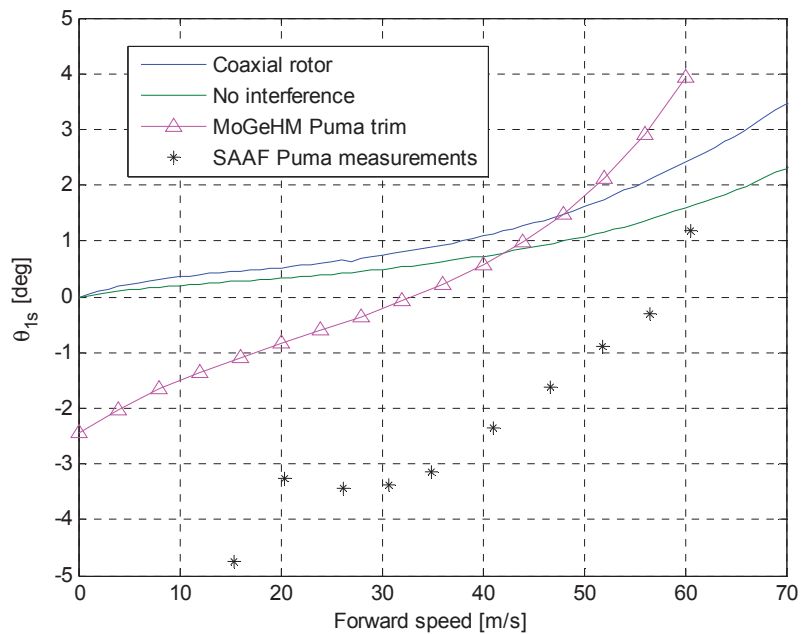**Figure 5.6: Lateral cyclic pitch angle in trimmed forward flight**

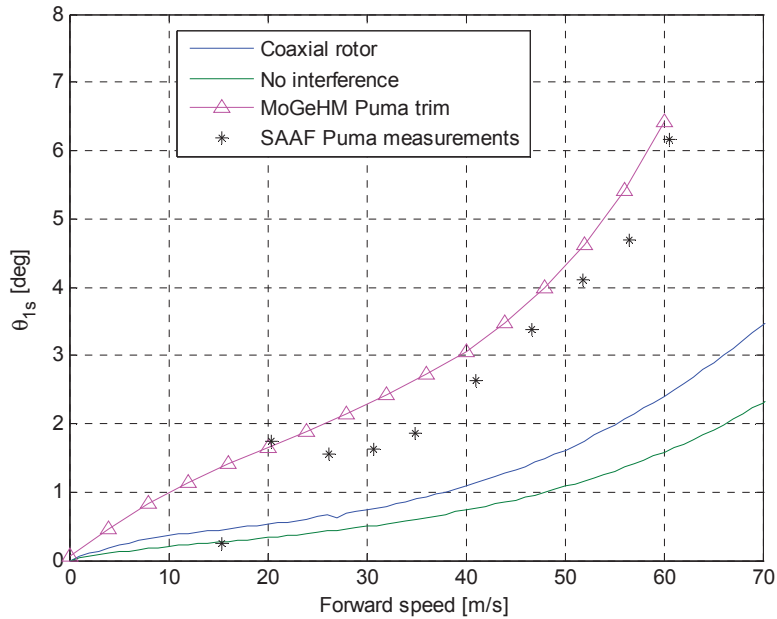**Figure 5.7: Longitudinal cyclic pitch angle in trimmed forward flight**

Figure 5.8: Longitudinal cyclic pitch angle in trimmed forward flight (with corrected data)

Fuselage pitch angle

The fuselage pitch angle is plotted against the forward speed in Figure 5.9. The slope difference between the "no interference" line and the simulated coaxial helicopter attracts immediately the attention. Apparently the coaxial helicopter has to tilt more forward to reach a particular forward speed, because of the mutual interference effects between the rotors. This coincides with the expectations, since the rotor interference leads to an increase of aerodynamic drag. The vertical shift in comparison with the Puma data arises from the fact that there is no shaft tilt included in the coaxial helicopter model. Again, the Puma data have been shifted in Figure 5.10. The coaxial fuselage pitch angle appears to correspond well with the Puma data.

Fuselage roll angle

Because there is no relationship between the longitudinal and lateral movement, the fuselage roll angle should theoretically be equal to zero in straight forward flight. This theoretical case can be seen in Figure 5.11 as the "no interference" case. Also the simulated coaxial helicopter shows a fuselage roll angle of almost zero from about *V = 25 m/s*, whereas the fuselage roll angle for the single rotor Puma helicopter shows a nonzero value for each forward speed. As mentioned before, this is due to the fact that a conventional helicopter has to suffer from unwanted cross-coupling effects between the longitudinal and lateral movement. Below *V = 25 m/s* there exists a small fuselage roll angle for the simulated coaxial helicopter. This effect can be attributed to the strong influence of the upper rotor at the lower rotor surface in the first *25 m/s*. Above *V = 25 m/s* the coaxial helicopter shows the expected behavior.
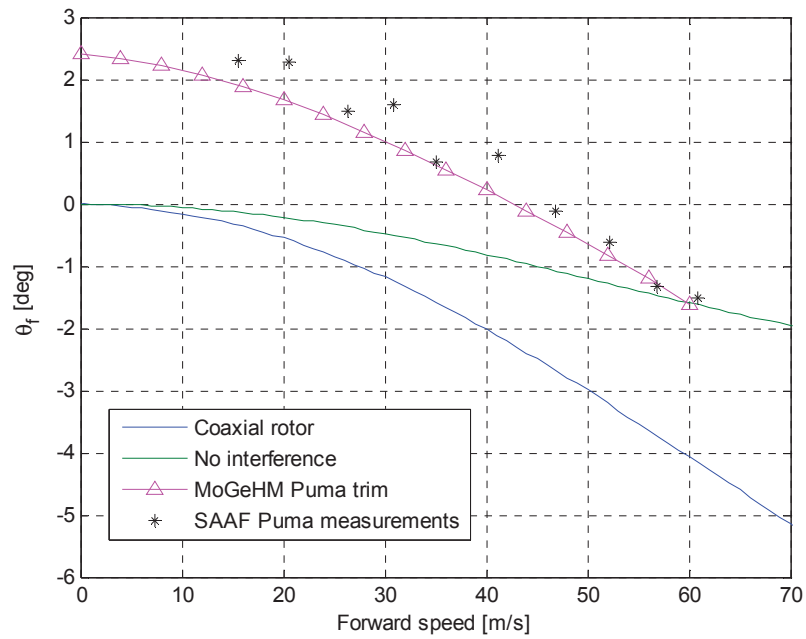
Figure 5.9: Fuselage pitch angle in trimmed forward flight
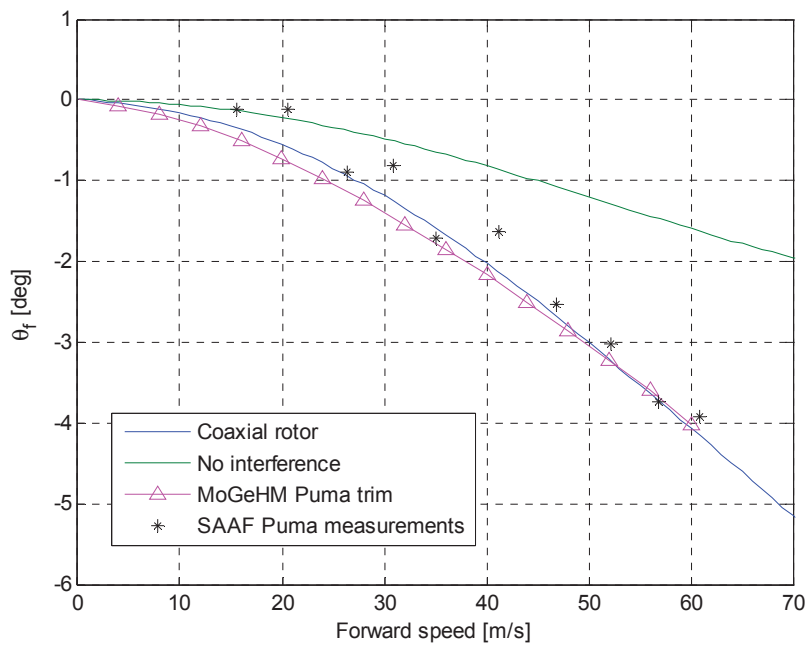

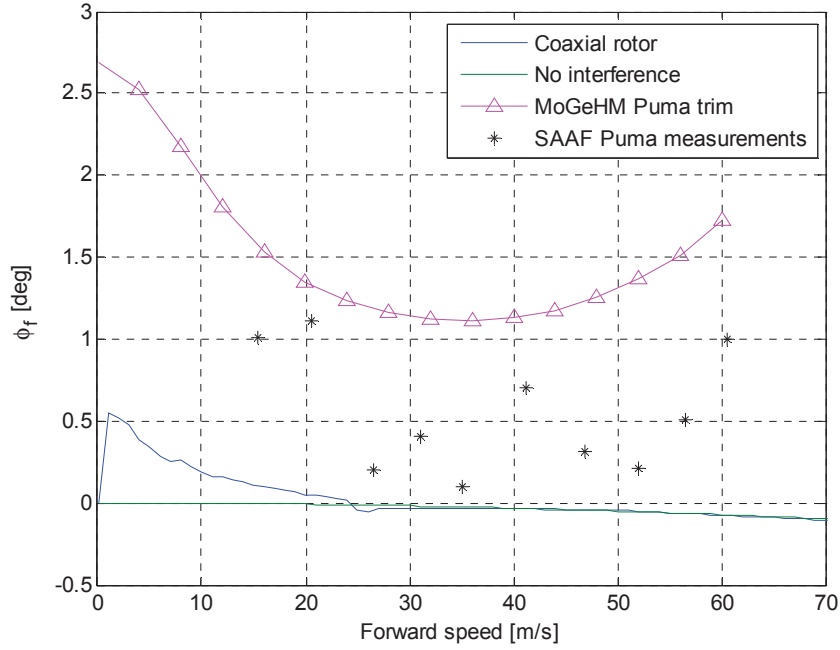**Figure 5.10: Fuselage pitch angle in trimmed forward flight (corrected data)**

Figure 5.11: Fuselage roll angle in trimmed forward flight

Induced velocity

As derived earlier in paragraph 4.1.5, the following equations hold for the non dimensional induced velocities of both rotors:

Upper rotor:

$$\lambda_u = \lambda_{0u} \tag{5.8}$$

Lower rotor:

$$\lambda_l = \lambda_{0l} + C_{att}\lambda_u \tag{5.9}$$

According to eq. (5.8) and (5.9) the induced velocity of the (isolated) upper rotor is always higher than the induced velocity of the (isolated) lower rotor if the attenuation coefficient has a positive value. Also Zimmer (ref. 59) and Nagashima (ref. 42) have derived that the lower rotor produces less thrust than the upper rotor, since the lower rotor works in the downwash field of the upper rotor. In Figure 5.12 one can see that the induced velocity of the lower rotor is indeed lower than the induced velocity of the upper rotor. Since the upper rotor wake has less influence on the lower rotor as the forward speed increases, it can be expected that the induced velocities should approach each other with increasing forward speed. This is indeed the case in Figure 5.12, but there is still a substantial difference between the two induced velocities. Apparently the upper rotor also influences the lower rotor when the lower rotor acts outside the upper rotor wake. The largest difference between the induced velocity of the upper and lower rotor appears to be at hovering flight. This can be explained by the fact that the upper rotor wake is covering both sections and by the approximation with the checkpoints this results in a coverage of almost the whole lower rotor surface (see Figure 5.3) through which the upper rotor wake has a great effect on the lower rotor in hovering flight. In reality, the difference between the induced

velocities will be a little less, since the checkpoint approximation is overestimating the region which lies inside the upper rotor wake.

As can be seen in Figure 5.12, the second switchpoint has a great impact on the induced velocity of the lower rotor. Apparently the transition from situation 2 to situation 3, where both sections are changing from situation, cannot be simulated smoothly.

Another remarkable effect is that the induced velocity of the lower rotor is almost equal to the "no interference" situation. Here should actually be expected that the "no interference" line is lying between the two rotors. The exact explanation for this effect is not known, but apparently the mutual interference has a positive effect with respect to the induced velocity of the (isolated) upper rotor and has almost no effect on the induced velocity of the (isolated) lower rotor. Note that the total induced velocity of the lower rotor according to eq. (5.9) is considerably higher than of the isolated lower rotor and even of the upper rotor.
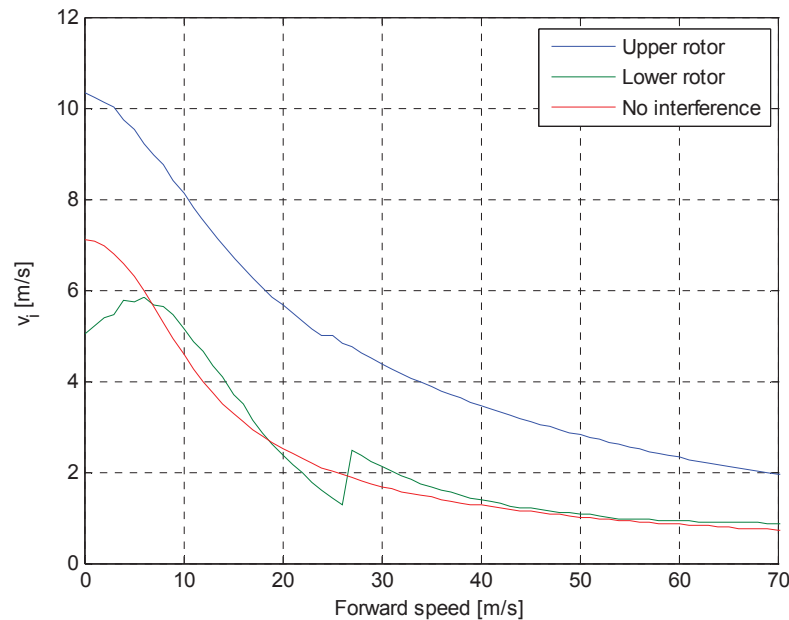

Figure 5.12: Induced velocities in trimmed forward flight

5.3 Performance calculations

In the previous paragraph the simulated data of the 6-DOF coaxial helicopter has not been validated with real experimental data of a coaxial helicopter, since there is very little information available. One given characteristic of the Ka-32 from Jane's (ref. 26) is the available continuous engine power and the maximum cruising speed. With the determined states and controls for each forward speed, it is possible to calculate the different power contributions and subsequently the total power required. After that, the maximum cruising speed of the simulated coaxial helicopter can be determined.

In forward flight the power required is determined by the following summation (ref. 29):

$$P_{req} = P_{par} + P_D + P_P + P_i \tag{5.10}$$

In which: P_{par} = Parasite power

P_D = Drag power

P_p = Profile drag power

P_i = Induced power

The different contributions for the required power in forward flight for a coaxial helicopter will now be determined.

Parasite power

In forward flight the parasite power P_p is required to overcome the drag of all the non-rotor components. A large portion of this power is due to the drag of the rotor hub. With a coaxial rotor configuration this drag is substantially higher than with a single rotor configuration.

The total parasite power required to overcome the parasite drag is (ref. 29)

$$P_{par} = f\frac{1}{2}\rho V^3 \tag{5.11}$$

The equivalent flat plate area *f* is already determined in paragraph 4.2.1.

Drag- and profile drag power

The total profile drag power consists of the profile drag of the rotor blades and the resultant of the profile drag in *x*-direction. Normally, this drag forces can be determined by applying the BEM, but for simplicity the drag- and profile drag power will be approximated by the Bennet approximation (ref. 29). The Bennet approximation is given by

$$P_p + P_d = \frac{\sigma \overline{C}_{Dp}}{8}\rho(\Omega R)^3 \pi R^2 (1 + 4.65\mu_x^2) \tag{5.12}$$

Induced power

The induced power P_i is caused by the backward tilt of the lift vector with respect to the rotor axis. This is caused by the induced velocity v_i. The total induced power for a coaxial helicopter consists of the summation of the induced power of the upper and lower rotor. The induced power for both the rotors is given by eq. (5.13) and (5.14).

$$P_{i\_u} = kT_u v_{i\_u} = kT_u \lambda_u (\Omega R) \tag{5.13}$$

$$P_{i\_l} = kT_l v_{i\_l} = kT_u \lambda_l (\Omega R) \tag{5.14}$$

The total induced power is now given by

$$P_i = P_{i\_u} + P_{i\_l} \tag{5.15}$$

Available power

The available power for cruising flight can be determined by multiplying the available engine power with the mechanical efficiency and the maximum continuous power factor:

$$P_{av} = P_{eng} \eta_m K_{cp} \tag{5.16}$$

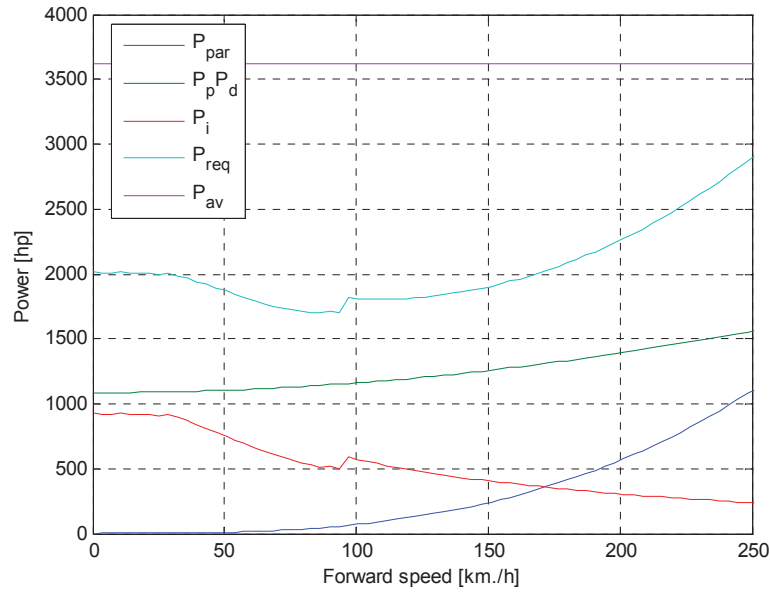The power contributions together with the total required power and the available power are plotted in Figure 5.13.

Figure 5.13: Required and available power against forward speed

As can be seen in Figure 5.13, the required power is substantially lower than the available power at the theoretical maximum cruising speed of *V = 230 km/h*. This indicates either a too low parasite power or a too low profile drag power. The cause of this event can be attributed to several factors. For example, the equivalent flat plate area has been approximated to be 4 m^2. When the equivalent should have been doubled in real case, the required power will be much higher and the maximum cruising speed is in this case around the theoretical maximum speed. This can be seen in Figure 5.14. In Figure 5.14 is also plotted the required power in case of the hypothetical "no interference" case. This will give some insight in the influence of the simulated interference between the rotors. As expected, the interference effects have a bigger influence at lower flight speeds.
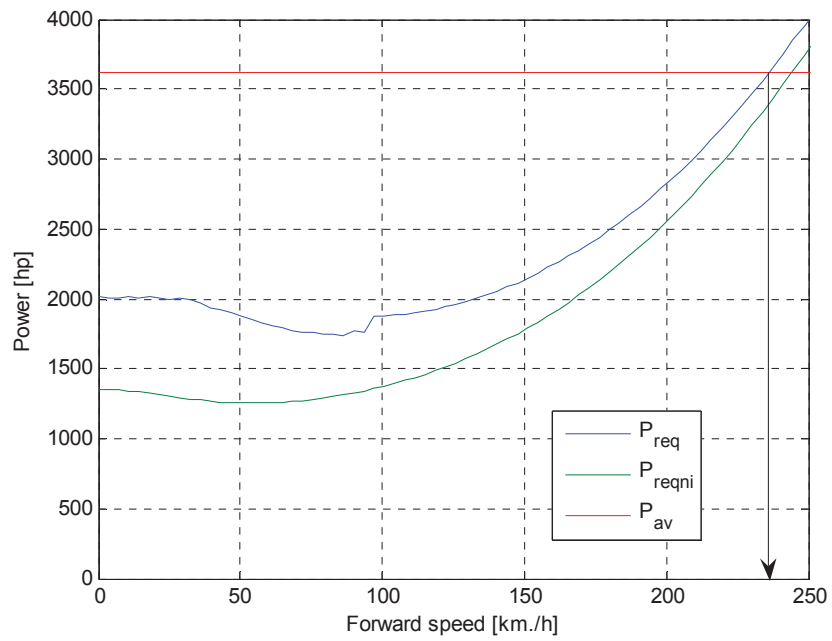
Figure 5.14: Required and available power against forward speed (corrected)

6 Dynamic response of the coaxial helicopter

In order to simulate the flying characteristics of the coaxial helicopter, the dynamic response in different flying conditions will be determined. The trim conditions at several forward speeds will be used as reference points and subsequently there will be given a certain disturbance to see how the coaxial helicopter will react.

6.1 Coaxial PID controller

Because of the unstable behavior of the helicopter, the helicopter not automatically returns to its trim or other desired position when a disturbance is given. In real case, the pilot takes care of the controls to bring the helicopter back in a stable flight condition. So, in order to stabilize the simulated helicopter after a given disturbance, an artificial pilot is needed.

The artificial pilot consists of PID-controllers to control the movements around the 6-DOF. A PID-controller consists of the following parts:

-   Proportional part: The proportional part of the PID-controller produces a response which is proportional to the difference between the desired state and the current simulated state (the current state error e). The proportional response can be adjusted by multiplying the current state error with a constant factor, which is called the proportional gain K_p. The rise time will be reduced by increasing the proportional gain.

-   Integrating part: The integrating part gives an output which is proportional to the current state error as well as the duration of the error. The I-action accumulates the offset that should have been corrected earlier by integrating the error over time. The integral response can be adjusted by multiplying the integral with a constant factor, which is called the integral gain K_i. The steady state error will be reduced by increasing magnitude of the integral gain.

-   Differential part: The differential part of the PID-controller gives an output which is proportional to rate of change of the error. The D-action determines the slope of the error over time and multiplies it with a constant factor, which is called the differential gain K_d. The overshoot will be reduced by increasing the influence of the differential part.
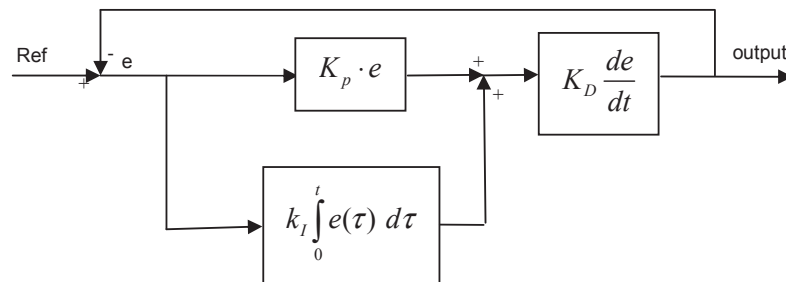
The PID controller will now look like Figure 6.1.

Figure 6.1: Standard PID controller layout

In order to handle the helicopter in 6-DOF, the artificial pilot has to control the helicopter in and around the following axes:

- In the x-axis (translational): To provide velocity control in the x-axis. (forward speed)
- In the y-axis (translational): To provide velocity control in the y-axis. (sideward speed)
- In the z-axis (translational): To provide velocity control in the z-axis. (up- and downward speed)
- Around the x-axis: To provide roll control.
- Around the y-axis: To provide pitch control.
- Around the z-axis: To provide yaw control.

The pilot controls above degrees of freedom with the four available control inputs in the helicopter: the longitudinal stick, the lateral stick, the collective (thrust) and the pedals. The PID-controller needs to be designed in such a way that it can control the inputs of the pilot, so the total helicopter controller will consist of four PID-controllers. Because the relation between the pilot's input in the cockpit and the resulting blade angle is not known for a coaxial helicopter, the PID-controllers will be designed to control the blade angles directly. The controllers for each control input will now be discussed.

Longitudinal stick control

The longitudinal stick input controls the pitch attitude and also the forward speed of the helicopter. By giving a positive (forward) input on the longitudinal stick, the blades will act as discussed in paragraph 4.1.4, and the helicopter will tilt forward. This is actually the same situation as for a conventional single rotor helicopter, only for a coaxial rotor the longitudinal cyclic input will be given on both the rotors on opposite sides. To control the pitch attitude of the coaxial helicopter properly, the following PID-controller has been designed:

$$\theta_{1s} = K_\theta (\theta_{req} - \theta) + K_{\theta\text{int}} \int_0^t (\theta_{req} - \theta) d\tau + K_q q + \theta_{1s\_trim} \qquad (6.1)$$

Lateral stick control

The longitudinal stick input controls the roll attitude and also the sideward speed of the helicopter. By giving a positive (rightward) input on the lateral stick, the blades will act as discussed in paragraph 4.1.4, and the helicopter will tilt to the right. This is the same situation as for a conventional single rotor helicopter, only for a coaxial rotor the lateral cyclic input will be given on both the rotors on opposite sides. To control the roll attitude of the coaxial helicopter properly, the following PID-controller has been designed:

$$\theta_{1c} = K_\phi (\phi_{req} - \phi) + K_{\phi\text{int}} \int_0^t (\phi_{req} - \phi) d\tau + K_p p + \theta_{1c\_trim} \qquad (6.2)$$

Collective (thrust) control

The collective thrust input controls the altitude and the vertical speed of the helicopter. By increasing collective input, the blades of both the rotors will collectively increase its blade pitch, which will result in more lift and subsequently the helicopter will move upwards. Again, this is the same situation as for a conventional single rotor helicopter, only the blade collective pitch will increase for both rotors. There

have to be designed two PID-controllers to control both the upper and the lower rotor in order to control the altitude of the coaxial helicopter. These two PID-controllers are almost identical; only the trim condition differs. The PID-controllers to control the altitude can be seen in eq. (6.3) and (6.4).

$$\theta_{0u} = K_z(z_{req} - z) + K_{z\,int}\int_0^t (z_{req} - z)d\tau + K_z\dot{z} + \theta_{0u\_trim} \tag{6.3}$$

$$\theta_{0l} = K_z(z_{req} - z) + K_{z\,int}\int_0^t (z_{req} - z)d\tau + K_z\dot{z} + \theta_{0l\_trim} \tag{6.4}$$

Pedal control

The pedals control the yaw (heading) angle and the angular velocity around the z-axis. For a conventional single rotor helicopter, the pedals control the collective pitch angle of the tail rotor. As mentioned in paragraph 3.3, because of the absence of the tail rotor, the coaxial helicopter has to control its heading in a different way. This is done by an independent change in collective for both rotors, which is called differential collective. In trimmed straight forward flight, the two sets of rotor blades produce the same torque. In order to make a heading change to the right, the collective pitch angle of the upper rotor blades will be increased and this will result in an increase of torque to the right. At the same time, the collective pitch angle of the lower rotor blades will be decreased and this will result in a decrease of torque to the left. Together this will result in a heading change to the right. The situation described above can be seen in Figure 6.2.
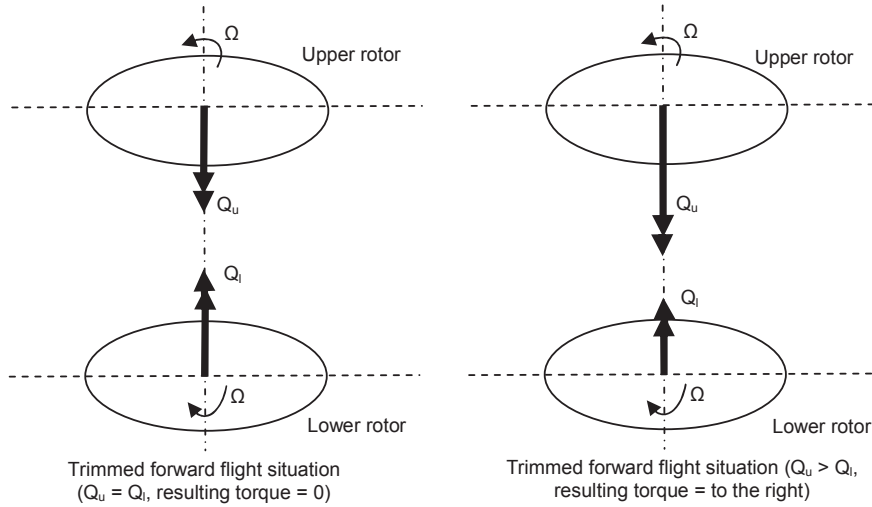

Figure 6.2: Situation sketch of a heading change to the right

So, in order to control the yaw angle of the helicopter, the PID-controller needs to control the difference in collective between the two rotors. The following PID-controller has been made:

$$(\theta_{0u} - \theta_{0l}) = K_\psi(\psi_{req} - \psi) + K_{\psi\,int}\int_0^t (\psi_{req} - \psi)d\tau + K_r r \tag{6.5}$$

Now, the contribution to each collective pitch angle needs to be determined in such a way that the total thrust of the helicopter will not change. The contribution from the differential collective to each rotor will

be fixed at 0.5 for the upper rotor and -0.5 for the lower rotor. The PID-controllers for both the rotors can now be seen in eq. (6.6) and (6.7).

$$\theta_{0u} = 0.5 \cdot (K_\psi(\psi_{req} - \psi) + K_{\psi\text{int}} \int_0^t (\psi_{req} - \psi)d\tau + K_r r) \tag{6.6}$$

$$\theta_{0l} = -0.5 \cdot (K_\psi(\psi_{req} - \psi) + K_{\psi\text{int}} \int_0^t (\psi_{req} - \psi)d\tau + K_r r) \tag{6.7}$$

As can be noticed above, the collective pitch delivers the control for two axes. The total collective control input for the upper rotor will be a summation of eq. (6.3) and (6.6), and the total collective control input for the lower rotor will be a summation of eq. (6.4) and (6.7).

The four PID-controllers were implemented in Simulink and the outputs of the controllers, together with the new states, will serve as inputs for the same coaxial helicopter model as has been derived in chapter 0. The Simulink model can be seen in Appendix B.

6.1.1 Determining the gains

In order to obtain an adequate controller it is very important to make a careful choice of each gain which makes part of the different PID-controllers. The following method is used to determine the gains:

1. Choose one control axis. The other axes will not be controlled and will remain in trimmed position.
2. Increase the proportional gain to improve the rise time to the desired state.
3. Increase the differential gain to improve (decrease) the overshoot.
4. Increase the integral gain to eliminate the steady state error.

Above steps will be executed for all control axes and the four controllers will eventually be joined together in Simulink. The determined gains can be seen in Appendix A.

6.2 Disturbances from trimmed condition

In order to check how the coaxial helicopter responds to a disturbance and whether the controllers of the different axes work properly, a disturbance (see Figure 6.3) will now be given on each control axis starting from a trimmed flight condition. After a certain time interval the controller of the concerned axis will be turned on in order to see how the controller brings the helicopter back to a steady trimmed position. The controllers of the other axes will be turned on during the whole procedure. The disturbances will be given in the low speed flight regime (according to ADS-33, ref. 53) at 20 m/s. The forward flight speed of 20 m/s is chosen, because the behavior of the coaxial helicopter is in accordance with the coaxial theory. This is in contrast to the lower speeds where there exists a small cross-coupling between the longitudinal and lateral movement (see paragraph 5.2). The duration and the amplitude of the steps are different for each disturbance in order to show good changes in the different states.
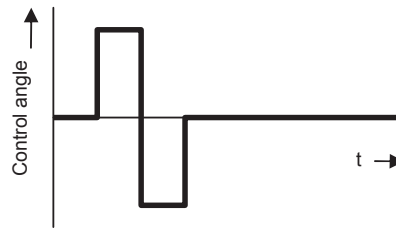
Figure 6.3: The shape of the disturbance

6.2.1 Longitudinal cyclic disturbance behavior

The procedure to check the response and stability around the y-axis is as follows:

1. 0 – 1 second: Trimmed forward flight at 20 m/s.

2. 1 – 2 seconds: Positive disturbance of θ_{1s} of 1 deg.

3. 2 – 3 seconds: Negative disturbance of θ_{1s} of 1 deg.

4. 3 – 10 seconds: Helicopter is free to move around the y-axis with θ_{1s} back in trimmed position.

5. 10 – 50 seconds: Longitudinal cyclic controller is turned on.

As can be seen in Figure 6.4, a positive disturbance at $t = 1\ s$ leads to a negative fuselage pitch angle (= nose tilt down movement) and an increasing forward flight speed. Of course, this is according to the expectations. One second later, there will be given a negative longitudinal cyclic input and as can be seen in Figure 6.4, the fuselage pitch angle immediately starts to increase and the forward flight speed starts to decrease a little later. When θ_f changes its rate, u responds a few seconds later. At $t = 3\ s$, the longitudinal cyclic is placed back in trimmed position, but the fuselage pitch angle is still increasing. This is because after pulling the stick, the helicopter still has a positive pitch rate. Only when the pitch rate is crossing zero, the pitch angle will start to decrease. This will be confirmed in Figure 6.5. Figure 6.5 also shows a reached pitch rate of about *8 deg/s*. The maximum pitch rate for a higher disturbance is probably high, because of the fact that a longitudinal cyclic stick input will result in a θ_{1s} deflection for the upper rotor as well as for the lower rotor, which both result in the same movement of the helicopter. In other words, a θ_{1s} disturbance of *1 deg* has twice the impact in comparison with a conventional single rotor helicopter. Anakin (ref. 3) states that the time to achieve a predetermined pitch angle with a coaxial rotor configuration is twice as less as for a single rotor configuration. (see also paragraph 3.2) This will be further discussed in paragraph 6.3.1.

Finally, Figure 6.4a shows no static state error for θ_f at *t = 50 s.* On the other hand, *u* shows a little error of approximately *0.25 m/s*, but this error is quite acceptable.
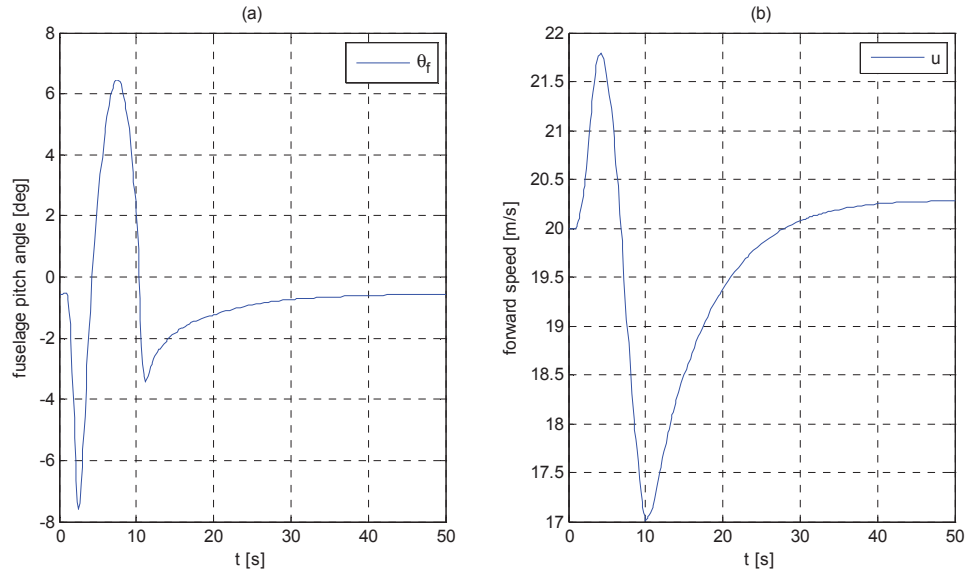
Figure 6.4: Fuselage pitch angle and forward flight speed behavior after longitudinal disturbance
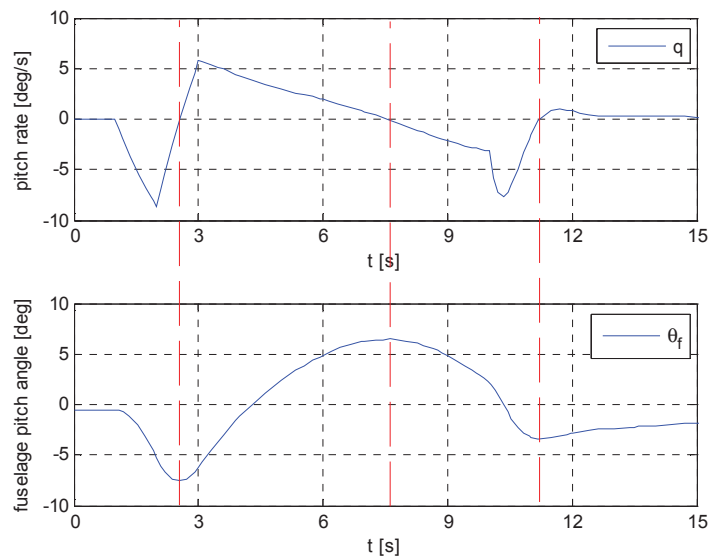

Figure 6.5: Relationship between pitch rate and fuselage pitch angle

According to the coaxial theory, a longitudinal disturbance should not influence the lateral behavior of the helicopter. In order to check this theory, the fuselage roll angle is plotted in Figure 6.6a. As can be seen in Figure 6.6a, the maximum roll angle difference is about *0.32 deg*. It can be concluded that the influence of the longitudinal disturbance on the lateral behavior of the coaxial helicopter is indeed minimal. Figure 6.6b shows that the maximum yaw angle difference is about *0.68 deg*. As expected, the longitudinal disturbance has no large effect on the yaw angle.
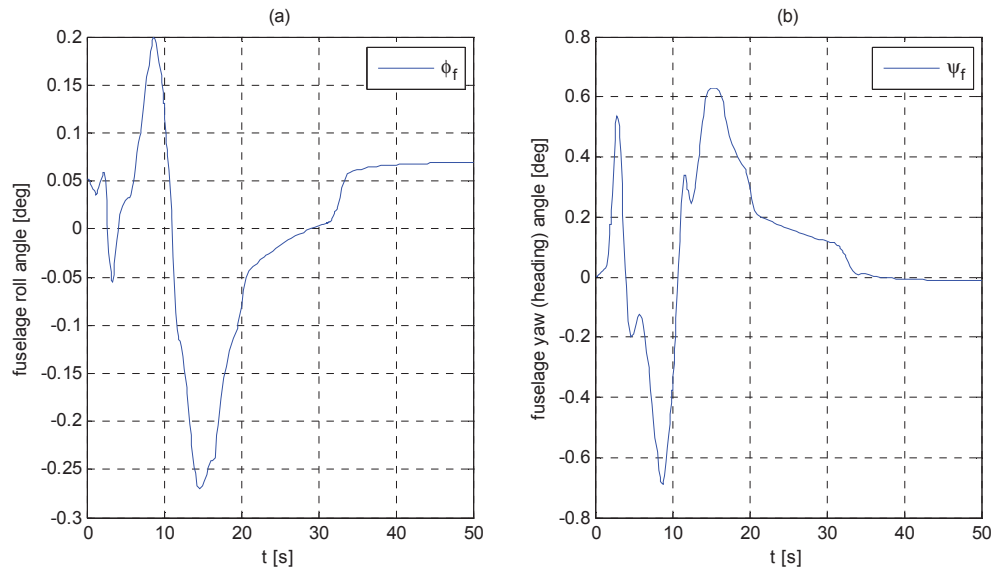
Figure 6.6: Roll and yaw angle behavior after a longitudinal disturbance

The effect on altitude after a longitudinal stick disturbance is shown in Figure 6.7. The thrust vectors of both rotors are tilting forward when the fuselage pitch angle gets more negative. Because of this, the lifting force of both rotors will decrease. Therefore a decrease in altitude will be expected after the pushing the stick forward. When the fuselage pitch angle increases, the opposite effect should happen. This is indeed the behavior as it occurs in Figure 6.7.
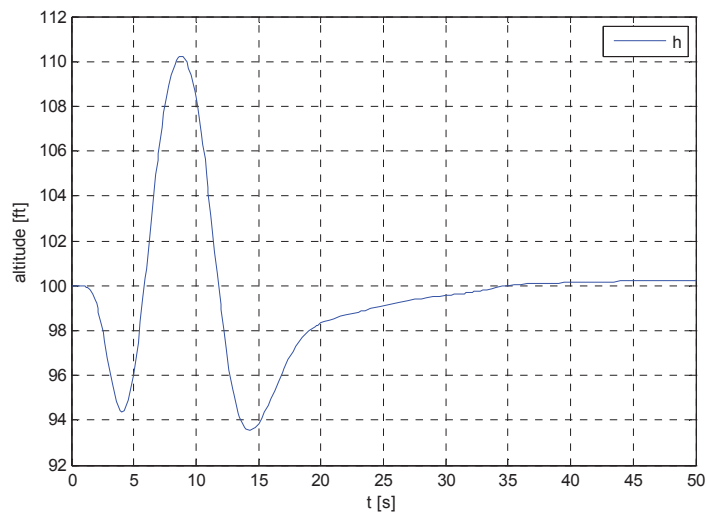
Figure 6.7: Altitude behavior after a longitudinal disturbance
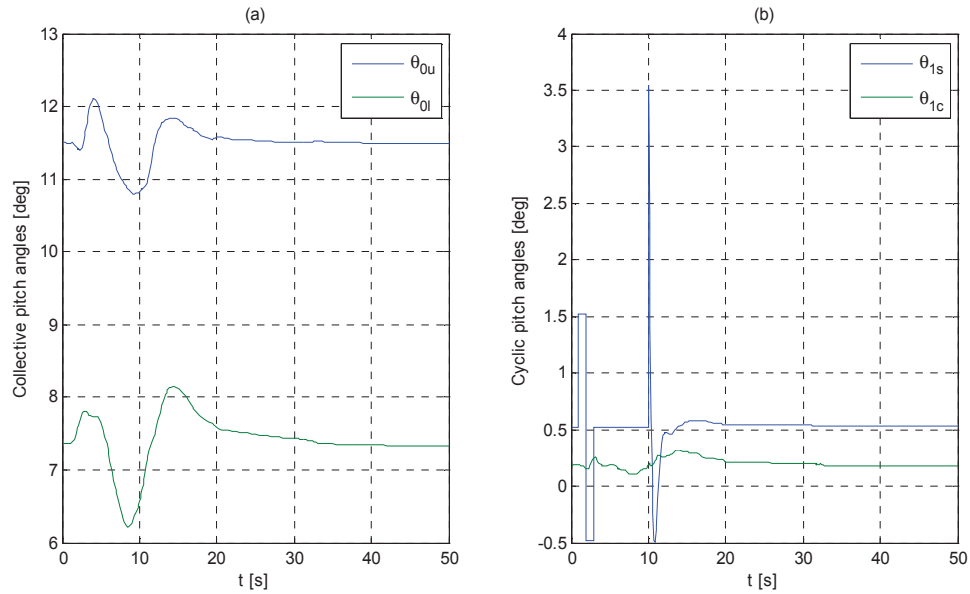
Figure 6.8: Control inputs after longitudinal disturbance

The control inputs during the manoeuvre are plotted in Figure 6.8. The collective pitch angles follow the same trend. This is because the influence of the longitudinal disturbance on the yaw angle is very small (see Figure 6.6), and therefore the differential collective input will be almost zero. The collective is only used to correct the altitude. The lateral cyclic pitch angle shows also very small deflections, because of the minimal cross-coupling between the longitudinal and longitudinal movements. The given longitudinal disturbance is shown in Figure 6.8b. Also the impact of the controller at $t = 10\ s$ is very obvious. The controller immediately wants to recover the current state to the required trim state.

6.2.2 Lateral cyclic disturbance behavior

The procedure to check the response and stability around the x-axis is as follows:

1. 0 – 1 second: Trimmed forward flight at 20 m/s.
2. 1 – 1.5 seconds: Positive (stick to the right) disturbance of θ_{1c} of 1 deg.
3. 1.5 – 3 seconds: Negative (stick to the left) disturbance of θ_{1c} of 1 deg.
4. 3 – 4 seconds: Helicopter is free to move around the x-axis with θ_{1c} back in trimmed position.
5. 4 – 80 seconds: Lateral cyclic controller is turned on.

As can be seen above, the positive disturbances with the lateral cyclic pitch angle will last for *0.5 s* instead of *1 s*, because a helicopter is turning a lot faster around its roll axis. This is because the moment of inertia around the x-axis is substantially lower. After the positive disturbance the negative disturbance has to neutralize the positive roll angle in order to achieve a negative roll movement. For that reason, the negative disturbance will last for 1.5 seconds. After the two disturbances the controller is turned on after only 1 second, because the helicopter still keeps rolling around the negative x-axis.

A positive (to the right) disturbance of the stick will result in a roll angle around the positive x-axis. This can be seen in Figure 6.9. The negative disturbance starts at *t = 1.5 s* and approximately *0.5 s* later,

the roll angle starts to decrease. This delay is again the result of the roll rate which still has a positive value (see Figure 6.10). At *t = 3 s* the stick is placed back in trimmed position, but Figure 6.10 shows that the pitch rate keeps increasing (in a negative sense) with a slightly lower slope. This indicates a very maneuverable behavior around its roll axis. The maximum achieved roll rate in this procedure is *40 deg/s*. This is probably the result of the lateral cyclic which influences both the upper and lower rotor as has been discussed in paragraph 6.2.1 and the low moment of inertia around the roll axis.

At last, Figure 6.9 shows that the fuselage roll angle Φ_f returns neatly to its original trim condition with a very fast rate.
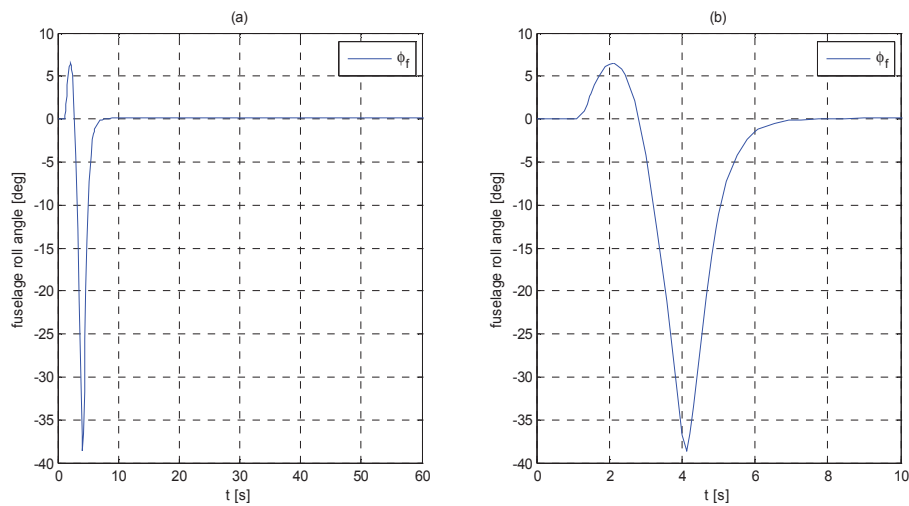
Figure 6.9: Fuselage roll behavior after a lateral disturbance
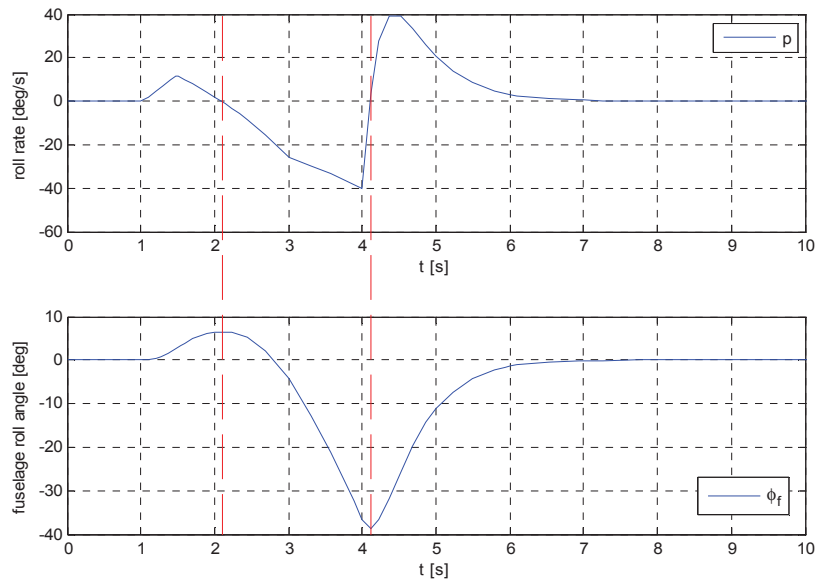
Figure 6.10: Relationship between pitch rate and fuselage pitch angle

According to the coaxial theory, a lateral disturbance should not influence the longitudinal behavior of the helicopter. In order to check this theory, the fuselage pitch angle is plotted in Figure 6.11b. As can be seen in Figure 6.11b, the maximum pitch angle difference is about *0.73 deg*. It can be concluded that the influence of the lateral disturbance on the longitudinal behavior of the coaxial helicopter is not zero, but very little. Figure 6.11a shows a maximum yaw angle difference of about *1.22 deg*. As expected, the lateral disturbance has little effect on the yaw angle of the helicopter.
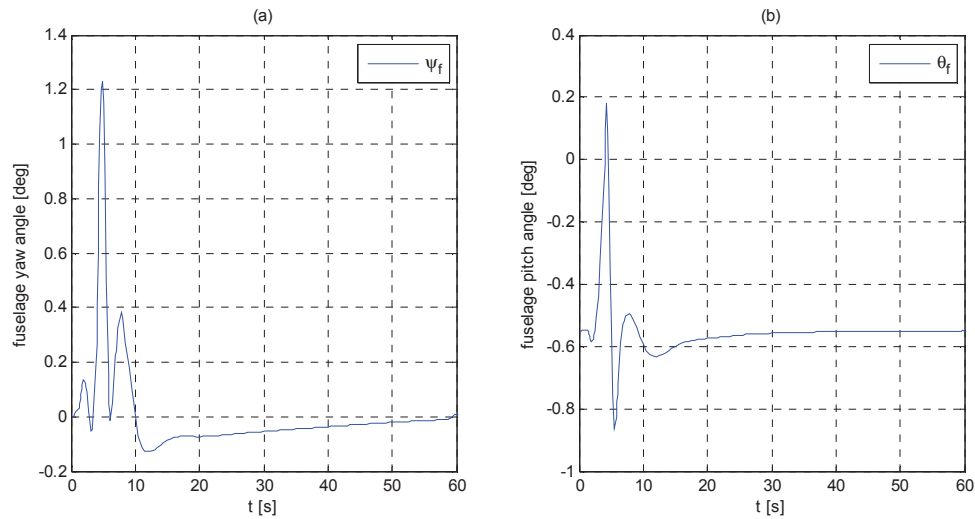
Figure 6.11: Yaw and pitch angle behavior after a longitudinal disturbance

The effect on the altitude after a lateral stick disturbance can be seen in Figure 6.12. The thrust vectors of both the rotors are tilting sideward when the fuselage roll angle is increased or decreased. So, the lifting force of both the rotors will decrease when the helicopter executes a roll movement to the left as well as to the right. Therefore a decrease in altitude will be expected during both the negative and positive disturbance. Figure 6.12 shows indeed a decreasing altitude until the roll angle is almost zero again. This can be seen better in Figure 6.13.
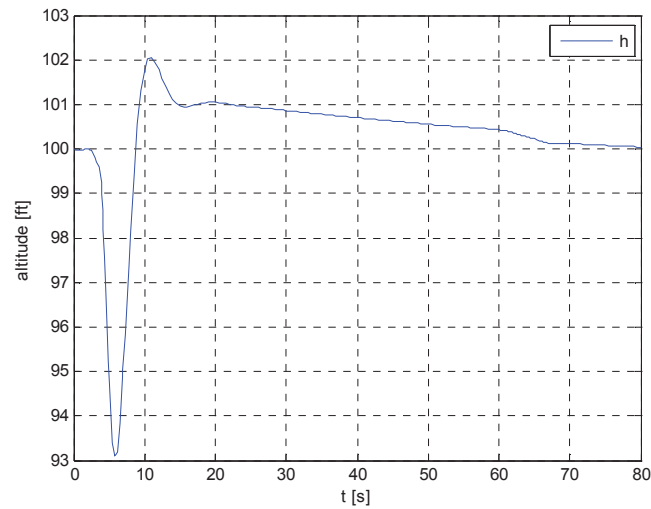
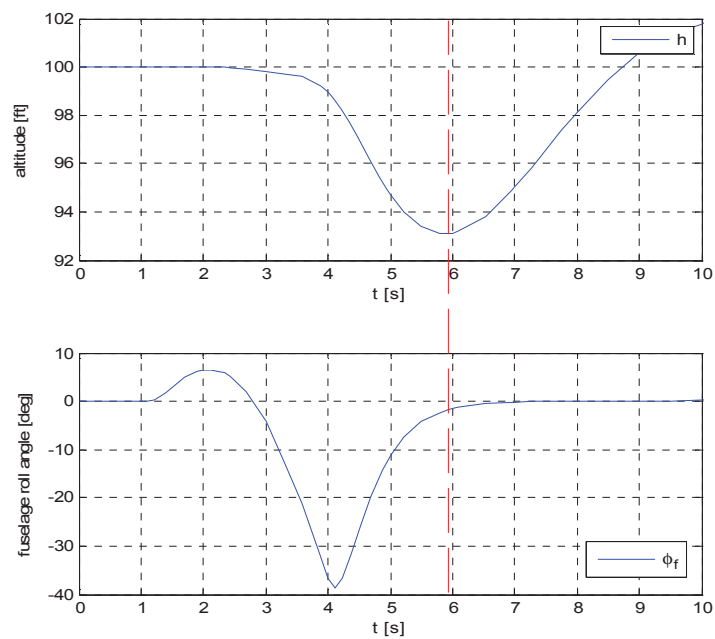**Figure 6.12: Altitude behavior after a lateral disturbance**

Figure 6.13: Relationship between altitude and roll angle

The control inputs during the procedure are plotted in Figure 6.14. The collective pitch angles show some small deflections to correct for the altitude and heading change. The longitudinal cyclic pitch angle shows also very small deflections to correct for the small fuselage pitch angle change. The given lateral disturbance can be well seen in Figure 6.14b. Also the impact of the controller is very obvious. Apparently the controller uses the maximum (*6.75 deg*) to correct for the given disturbance.
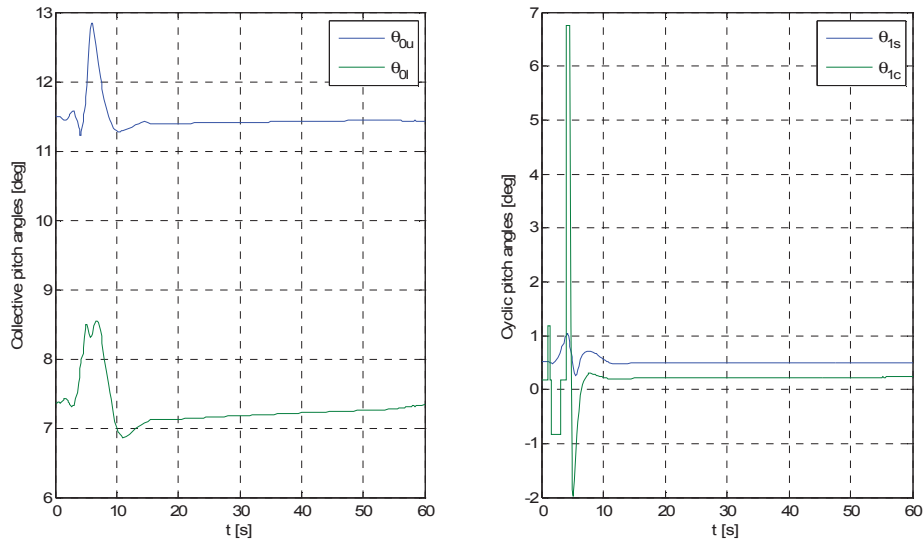
Figure 6.14: Control inputs after a lateral disturbance

6.2.3 Directional disturbance behavior

The procedure to check the response and stability around the z-axis is as follows:

1. 0 – 1 second: Trimmed forward flight at 20 m/s.
2. 1 – 2 seconds: Positive disturbance of ($\theta_{0u} - \theta_{0l}$) of 1 deg.
3. 2 – 3.5 seconds: Negative disturbance of ($\theta_{0u} - \theta_{0l}$) of 1 deg.
4. 3.5 – 10 seconds: Helicopter is free to move along the z-axis with θ_{0u} and θ_{0l} back in trimmed position.
5. 10 – 40 seconds: Pedal controller is turned on.

A positive disturbance (pushing the right pedal) should lead to a (positive) yaw angle to the right. The opposite should appear when pushing the left pedal. This is indeed the situation in Figure 6.15. Just as for the previous axes, the yaw angle will start to increase or decrease when the yaw rate is crossing zero. This can be seen in Figure 6.16. Figure 6.16 shows also that after the negative disturbance is given, the yaw rate remains almost constant until the controller was switched on. This implies that the movement around the yaw axis does not experience much resistance. The coaxial helicopter achieved a yaw rate of *11 deg/s*. Of course, the yaw rate will be a lot higher if the disturbance is higher. A very high maximum yaw rate should be expected, since the way how the yawing moment is achieved (see paragraph 3.3) can lead to very high yawing moments. This will be discussed further in paragraph 6.3.3.

Figure 6.17 shows a maximum difference in fuselage pitch angle of *0.06 deg* and a maximum difference in roll angle of *0.37 deg*. Apparently the directional disturbance has almost no influence on the pitch and roll axis.
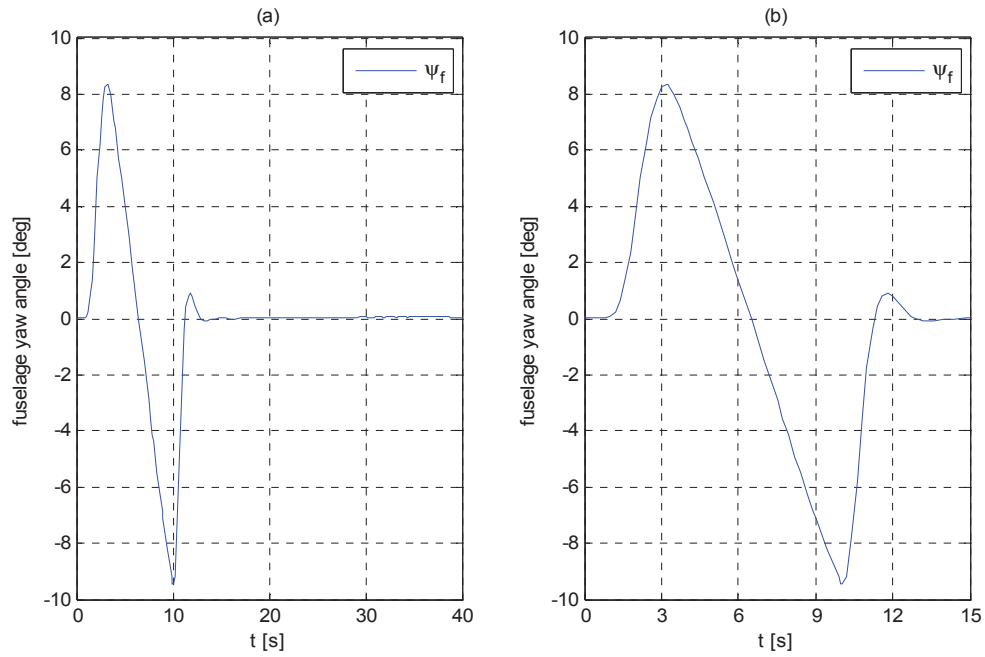
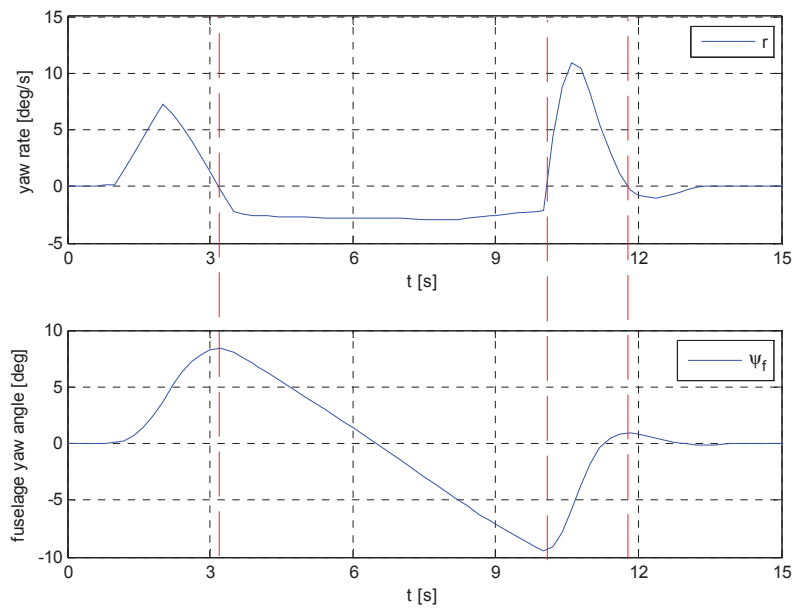Figure 6.15: Yaw (heading) angle response after directional disturbance

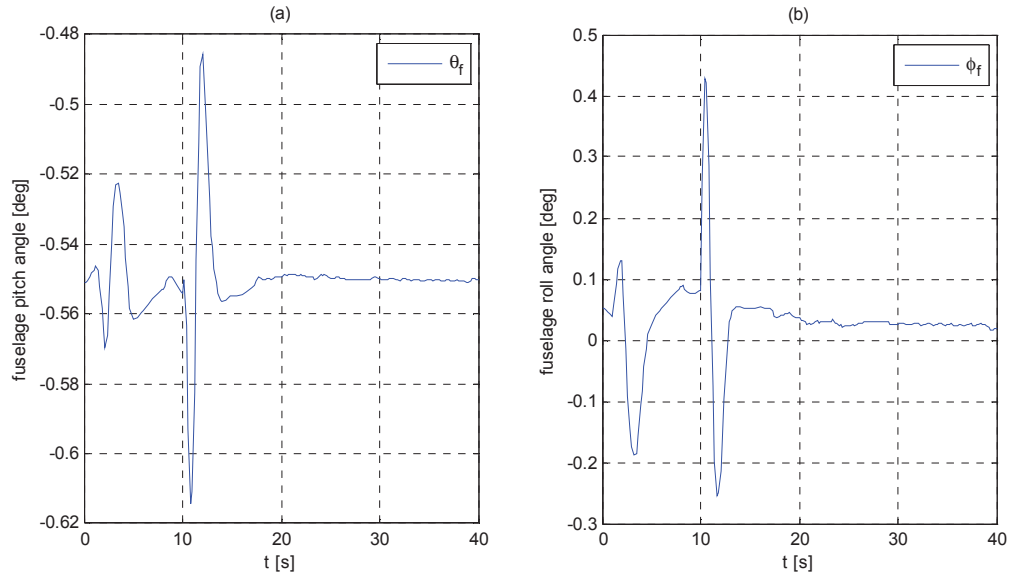Figure 6.16: Relationship between yaw rate and fuselage yaw angle after directional disturbance

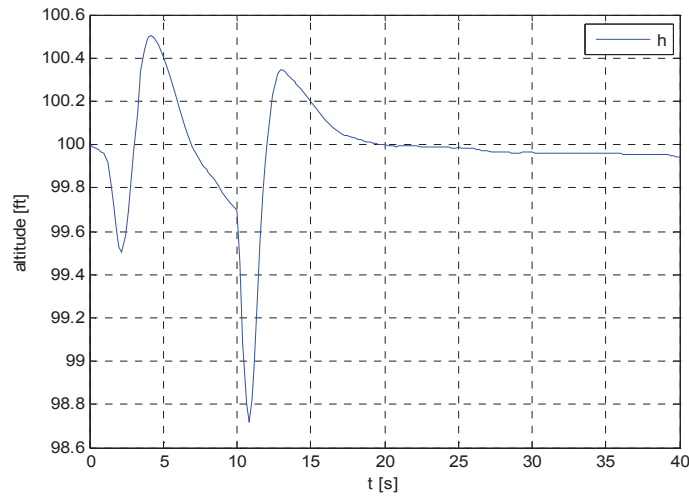**Figure 6.17: Pitch and roll angle behavior after a directional disturbance**

Figure 6.18: Altitude behavior after a directional disturbance

The effect on the altitude after a directional disturbance can be seen in Figure 6.18. The collective pitch of the rotors controls the directional movement as well as the altitude, so a large effect on the altitude can be expected. However, the trend of the altitude is highly influenced by the yaw disturbance, but the maximum difference (1.3 ft) is actually very small. This improves the controllability of the coaxial helicopter.

Finally, the control inputs during the procedure are plotted in Figure 6.19. The collective pitch angles show the given differential disturbance ($\theta_{0u} - \theta_{0l}$) and at $t = 10\ s$ the impact of the directional controller. It can be noticed that the disturbance is not a real step input. This is because the collective pitch angle is influenced by the altitude controller at the same time. The cyclic pitch angles show small deflections to correct for the roll and pitch angles as can be seen in Figure 6.17.
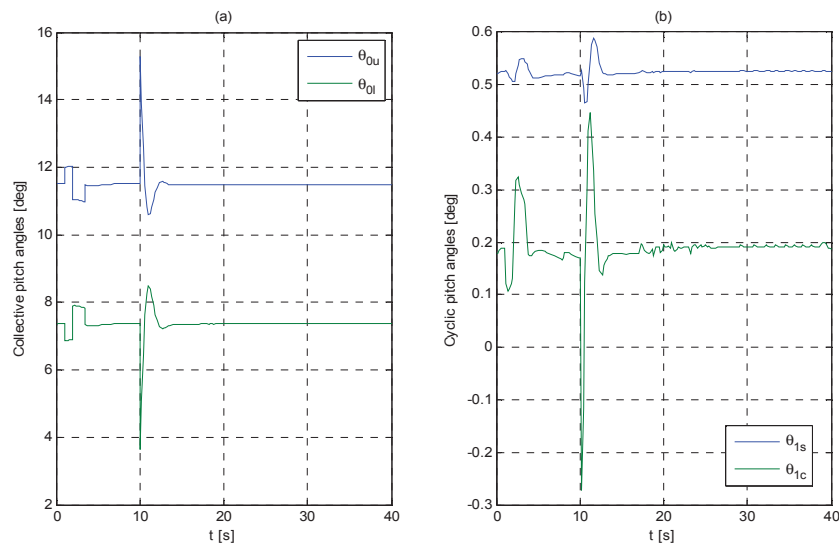
Figure 6.19: Control inputs during the directional disturbance procedure

6.2.4 Collective disturbance behavior

The procedure to check the response and stability along the z-axis is as follows:

1. 0 – 1 second: Trimmed forward flight at 20 m/s.
2. 1 – 2.5 seconds: Positive disturbance of θ_{0u} and θ_{0l} of 2 degrees.
3. 2.5 – 4.5 seconds: Negative disturbance of θ_{0u} and θ_{0l} of 2 degrees.
4. 4.5 – 10 seconds: Helicopter is free to move along the z-axis with θ_{0u} and θ_{0l} back in trimmed position.
5. 10 – 40 seconds: Collective controller is turned on.

When the pilot wants to increase the altitude of the helicopter, he/she should give a positive input (pulling) to the collective. Figure 6.20 shows indeed a positive altitude change after pulling the collective. After pushing the collective, the altitude decreases after a delay of *0.5 s*, because the helicopter still has an upwards velocity. The collective controller has been switched on at *t = 10 s* and the altitude returns to its original trim position within *10 s*.
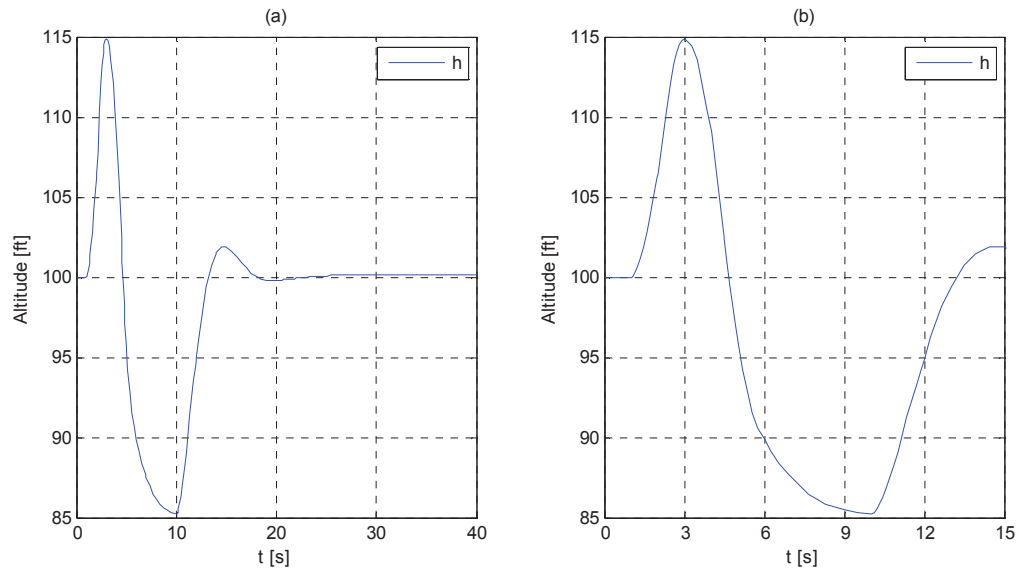
Figure 6.20: Altitude behavior after a collective disturbance

The fuselage angles around the 3 axes can be seen in Figure 6.21. The maximum difference in pitch and roll angle is *0.6 deg* and *1.3 deg* respectively, so there is little influence due to the collective disturbance. This is in contrast to the maximum difference in fuselage yaw angle, which is about *6.9 deg*. It can be concluded that a change in collective pitch angle for both the rotors substantially influences the directional movement, whereas the directional disturbance only influenced the altitude a little (see Figure 6.18). For the rest, all the fuselage angles return to their original trim positions.
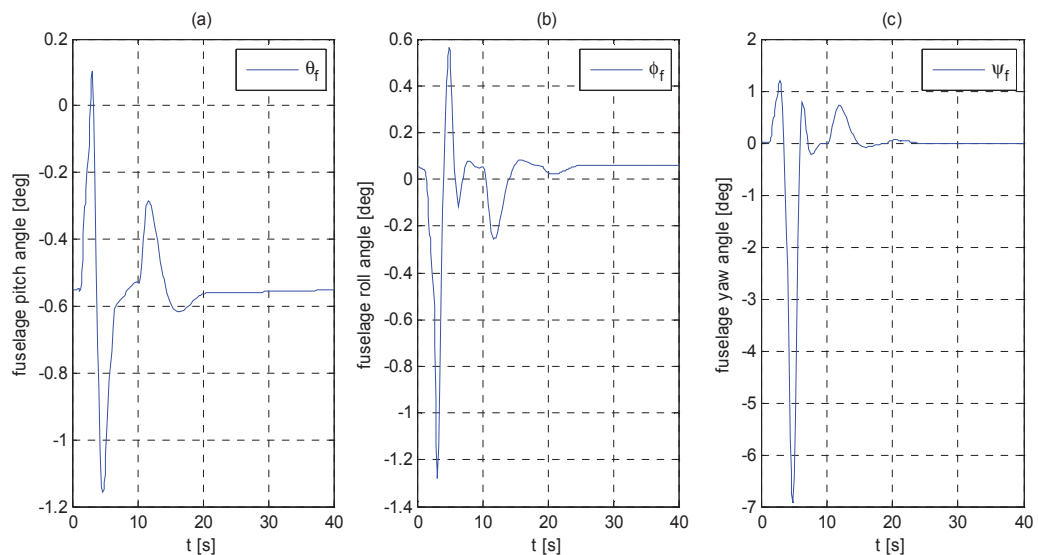

Figure 6.21: Fuselage angles behavior after a collective disturbance

The control inputs after the collective disturbance can be seen in Figure 6.22. The collective pitch inputs during the disturbance attract the attention. It shows how the directional controller is influencing the collective inputs to correct for the yaw angle as can be seen in Figure 6.21c. To be perfectly clear, the summation of the two collective pitch inputs has also been plotted in Figure 6.22a in order to ignore the differential collective input. The lateral and longitudinal cyclic pitch inputs show small deflections to correct for the fuselage angles as can be seen in Figure 6.21a and b.
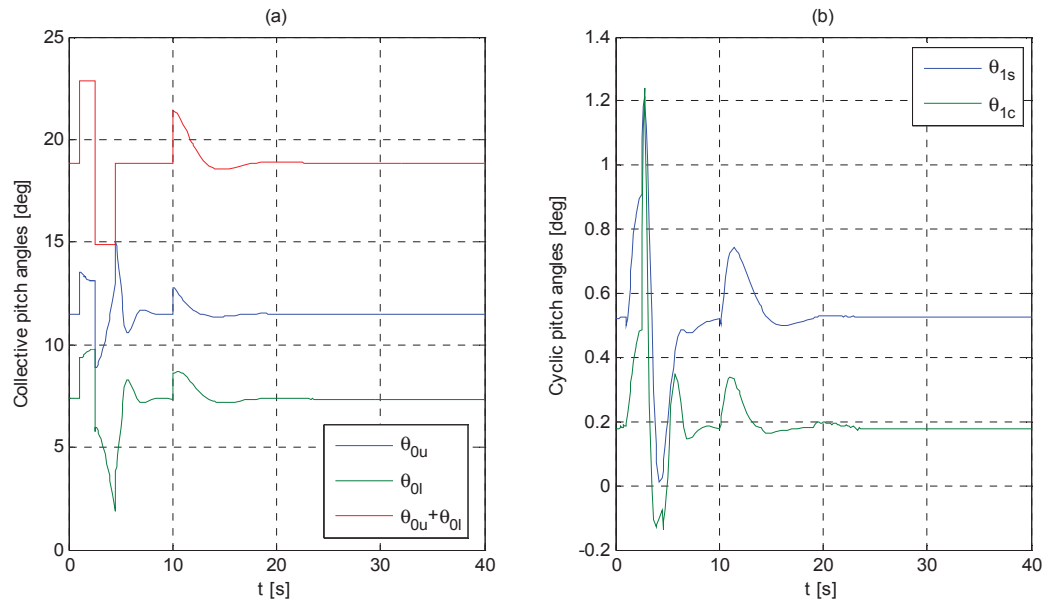

Figure 6.22: Control inputs after a collective disturbance

6.3 Attitude quickness analysis

A combat helicopter should comply with the "Aeronautical design standard performance specification, handling qualities requirements for military rotorcraft" (ADS-33, ref. 53). The ADS-33 contains several handling qualities, under which the "Attitude quickness" requirements. The attitude quickness is very interesting to consider, since the coaxial helicopter has a reputation for quick pitch and heading changes. In order to determine whether the simulated coaxial helicopter meets the ADS-33 requirements, the attitude quickness will be determined for the coaxial helicopter. The following specification is written in paragraph 3.3.3 of the ADS-33 with respect to the attitude quickness: "The ratio of peak pitch (roll) rate to change in pitch (roll) attitude, $q_{pk} / \Delta\theta_{pk}$ ($p_{pk} / \Delta\phi_{pk}$), shall meet the limits specified in Figure 6.23 (and Figure 6.24)." Also the attitude quickness for heading changes will be determined in the same way and should meet the limits in Figure 6.25.
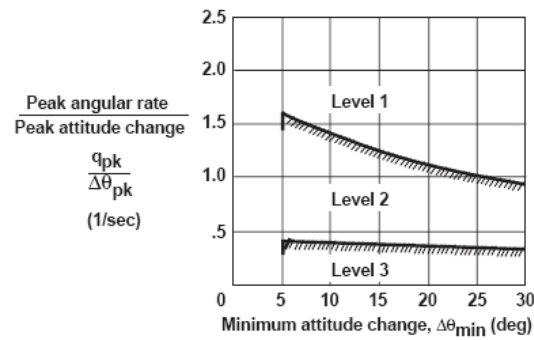

Figure 6.23: Pitch attitude quickness requirements according to ADS-33 (from ref. 53)
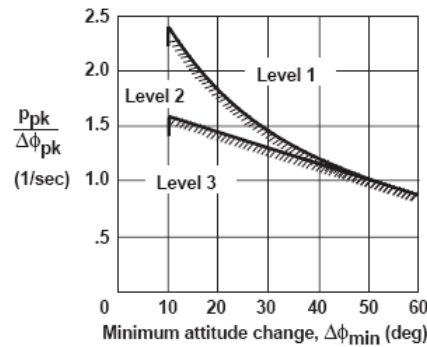

Figure 6.24: Roll attitude quickness requirements according to ADS-33 (from ref. 53)
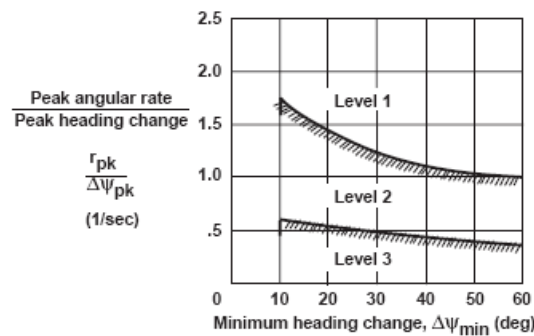

Figure 6.25: Heading attitude quickness requirements according to ADS-33 (from ref. 53)
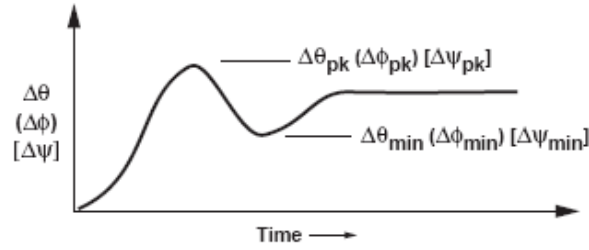
Figure 6.26: Definition of the peak and minimum attitude change (from ref. 53)

The peak and minimum attitude change is needed to determine the quickness. Figure 6.26 shows how these properties will be determined. In Figure 6.23 to Figure 6.25 three levels can be distinguished, which are fixed by the ADS-33. The helicopter has to meet the level 1 requirement in order to have desired handling qualities in the operational flight envelope. According to ADS-33 the quickness has to be determined in the low speed flight regime, so the quickness values will be determined at *V = 20 m/s*.

6.3.1 Pitch attitude quickness

The pitch attitude quickness will be determined by giving a pitch attitude change to the coaxial helicopter model. This will be done for attitude changes of *5 deg* to *30 deg*. Subsequently, the quickness will be plotted against the minimum attitude change and will be compared with the ADS-33 requirements.

The results for the attitude change of *5 deg* are given in Figure 6.27. Because the trimmed pitch attitude is corrected to *0 deg*, the 'Δ-values' are simply equal to the current pitch angle. The data of Figure 6.27 will be used to calculate one point in the 'quickness-plot'. The calculation for an attitude change of *5 deg* is given in eq. (6.8).

$$Q_{pitch(5\deg)} = \frac{q_{pk}}{\Delta\theta_{pk}} = \frac{7.5457 \text{ deg/s}}{5.4666 \text{ deg}} = 1.38 \ s^{-1} \tag{6.8}$$
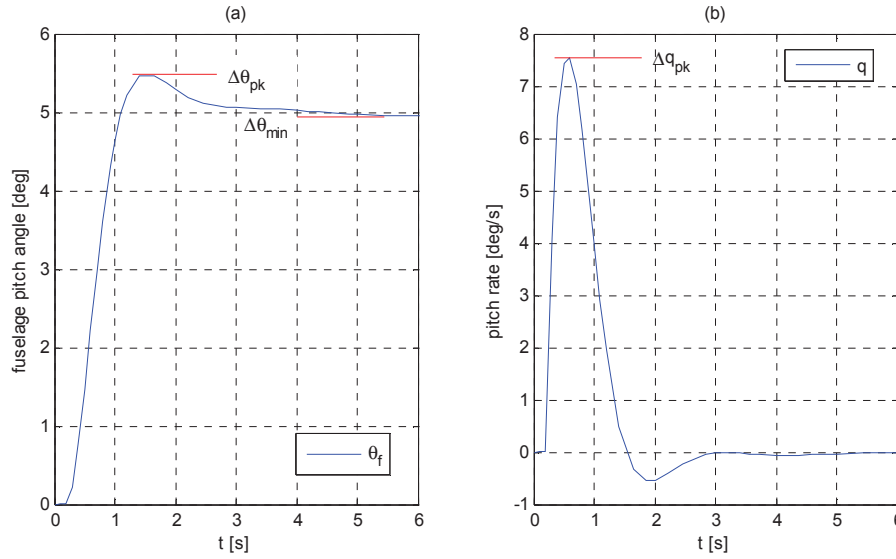
Figure 6.27: Fuselage pitch angle and pitch rate behavior to achieve a pitch attitude change of 5 degrees

The method described above will be used to determine the quickness for all the attitude changes. This will be done by a Matlab routine (see Appendix B). The fuselage pitch angles and pitch rates for all the attitude changes can be found in Appendix D.

The calculated quickness values for each attitude change can be seen in Figure 6.28. The level boundaries according to ADS-33 are also approximated in order to look whether the quickness values comply with the ADS-33 requirement. It is clear that the coaxial helicopter does not meet the level 1 requirement for low attitude changes. The quickness values show a straight line which crosses the level 1 boundary at an attitude change of *15 deg*. A straight line of the quickness values implies that the maximum longitudinal cyclic is not reached, through which the maximum pitch rate and the maximum reached pitch attitude can both increase and keep the same ratio (= quickness). Figure 6.29a shows the longitudinal cyclic input for an attitude change of *5 deg*. It shows that the maximum used longitudinal cyclic pitch angle is only *-3.5 deg*, whereas the assumed range of the longitudinal cyclic is assumed to be equal to *+/- 15 deg* (see Appendix A).
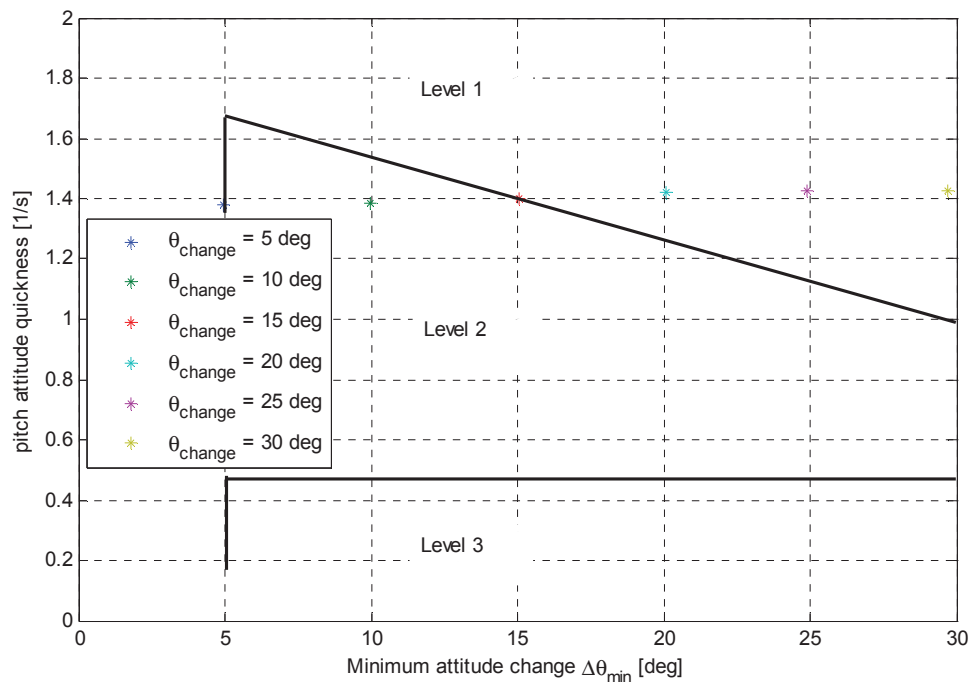
Figure 6.28: Pitch attitude quickness compared with ADS-33 requirements

Above an attitude change of *20 deg*, Figure 6.28 shows a little decreasing quickness. Apparently the maximum longitudinal cyclic angle is reached here. This is confirmed by Figure 6.29b.

The aggressiveness of the pilot by means of the gains of the pilot PID-controller substantially influences the usage of the longitudinal cyclic. Padfield (ref. 44) stated that at the highest level of aggressiveness, "the pilot is attempting to fly the manoeuvre as quickly as possible." In this case the pilot should give the maximum longitudinal cyclic input at each attitude change. The real maximum achievable quickness values will now arise. In order to show this, the proportional gain of the longitudinal cyclic controller has been increased until the maximum longitudinal cyclic input of *-15 deg* has reached. This can be seen in Figure 6.30c. Figure 6.30a and b show the accompanying pitch attitude and pitch rate behaviour. The quickness values with this "gain-configuration" are plotted in Figure 6.31. The accompanying pitch attitude, pitch rate and longitudinal cyclic angle behaviour to determine the remaining quickness values can be found in Appendix D.
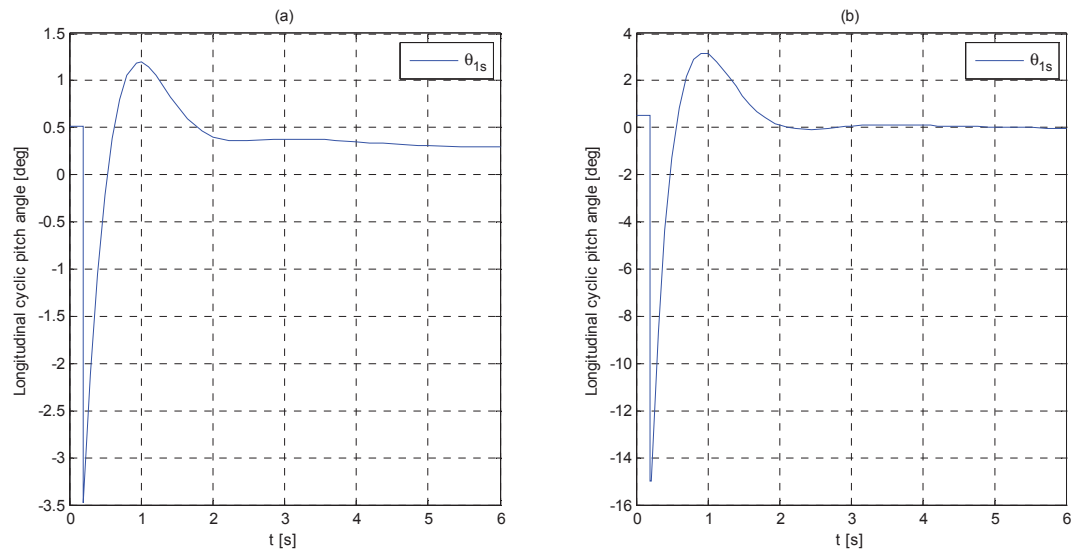
Figure 6.29: Longitudinal cyclic pitch input for an attitude change of 5 degrees (a) and 20 degrees (b)
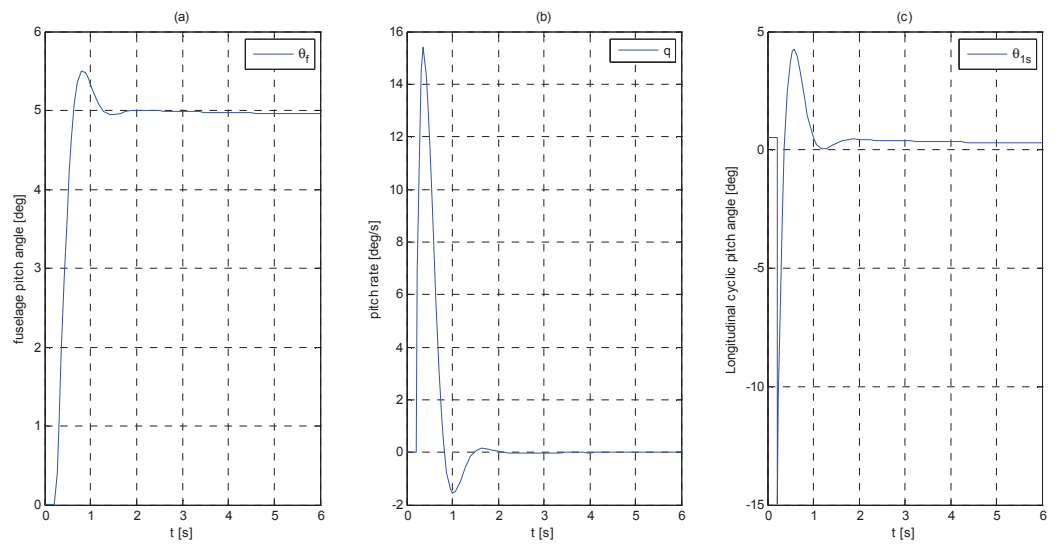

Figure 6.30: Pitch attitude, pitch rate and longitudinal cyclic angle to achieve a maximum quickness for an attitude change of 5 degrees
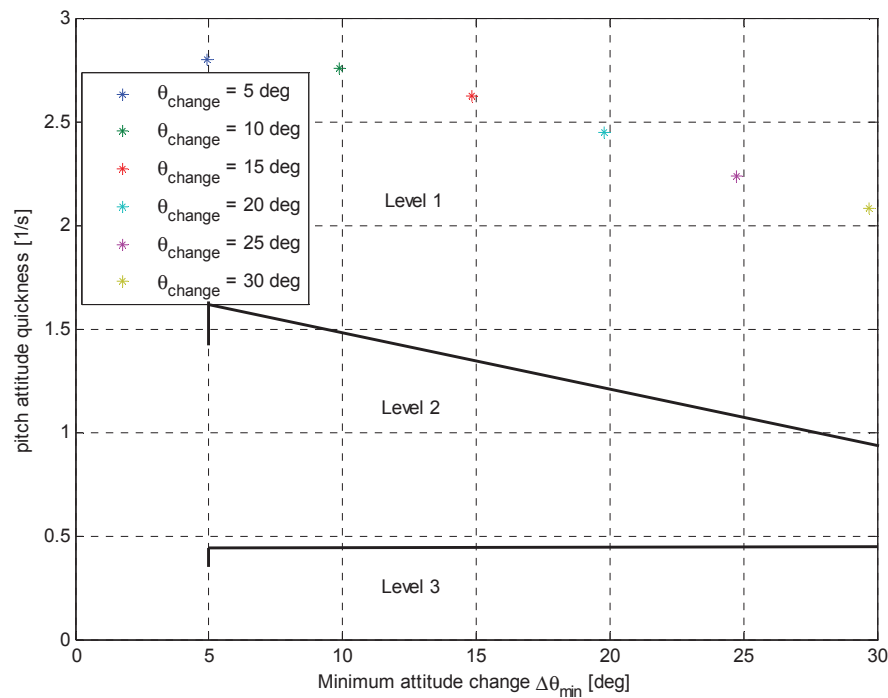
Figure 6.31: Maximum pitch attitude quickness compared with ADS-33 requirements

Figure 6.31 shows the expected decreasing quickness values for increasing attitude changes. It also shows pitch attitude quickness values of about two times the required quickness values for level 1. As mentioned in paragraph 6.2.1, this is exactly what should be expected, because of the fact that a longitudinal cyclic stick input will result in a θ_{1s} deflection for the upper rotor as well as for the lower rotor, which both result in the same movement of the helicopter. In other words, a θ_{1s} disturbance of *1 deg* has twice the impact in comparison with a conventional single rotor helicopter. Anakin (ref. 3) also stated that the time to achieve a predetermined pitch angle with a coaxial rotor configuration is twice as less as for a single rotor configuration (see also paragraph 3.2). Figure 6.31 confirms this statement. Nevertheless, the quickness results strongly depend on the assumed blade range, which is an estimated value. The moments of inertia also influence the quickness of the helicopter and these are assumed to be equal to the Puma data. All in all, the results of Figure 6.31 coincide with the expectations, but are not really reliable.

6.3.2 Roll attitude quickness

The roll attitude quickness will be determined by giving a roll attitude change to the coaxial helicopter model. This will be done for attitude changes of *10 deg* to *40 deg*. Note that the ADS-33 works with attitude changes until *60 deg*, but there has been noticed that it is difficult for the coaxial helicopter to stay steady at a high roll angle. The reason for this behavior is not known. The quickness will be plotted against the minimum attitude change and will be compared with the ADS-33 requirements.

The results for the attitude change of *10 deg* are given in Figure 6.32. Again, the data of Figure 6.32 will be used to calculate one point in the 'quickness-plot'. The calculation for a roll attitude change of *10 deg* is given in eq. (6.9).

$$Q_{roll(10\deg)} = \frac{p_{pk}}{\Delta\phi_{pk}} = \frac{18.9867 \text{ deg/s}}{11.1436 \text{ deg}} = 1.704 \ s^{-1} \tag{6.9}$$
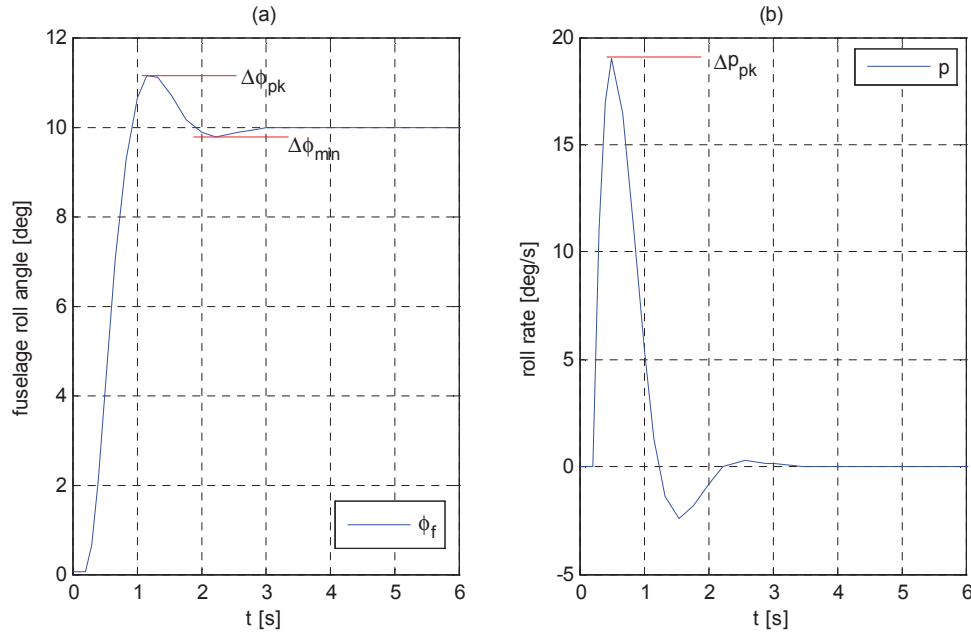

Figure 6.32: Fuselage roll angle and roll rate behavior to achieve a roll attitude change of 10 degrees

The method described above will be used to determine the quickness values for all roll attitude changes. This will be done by a Matlab routine (see Appendix B). The fuselage roll angles and roll rates for all attitude changes can be found in Appendix D.

The calculated roll quickness values for each attitude change can be seen in Figure 6.33. Figure 6.33 shows a deterioration of the roll quickness. Apparently the maximum achievable lateral pitch angle of +/- *6.75 deg* is already reached at an attitude change of *20 deg*. This is confirmed by Figure 6.34.

The level boundaries according to ADS-33 are also approximated in Figure 6.33 in order to find out whether the quickness values comply with the ADS-33 requirement. The quickness for low roll attitude changes does not comply with the level 1 requirement. Higher values should be expected, because the lateral movement is controlled by the lateral cyclic of both rotors. The quickness values are again based on the used pilot PID-controller for the coaxial helicopter, so the low quickness values can be attributed to the same causes as mentioned in paragraph 6.3.1. The roll quickness will increase by increasing the proportional gain of the lateral cyclic controller.
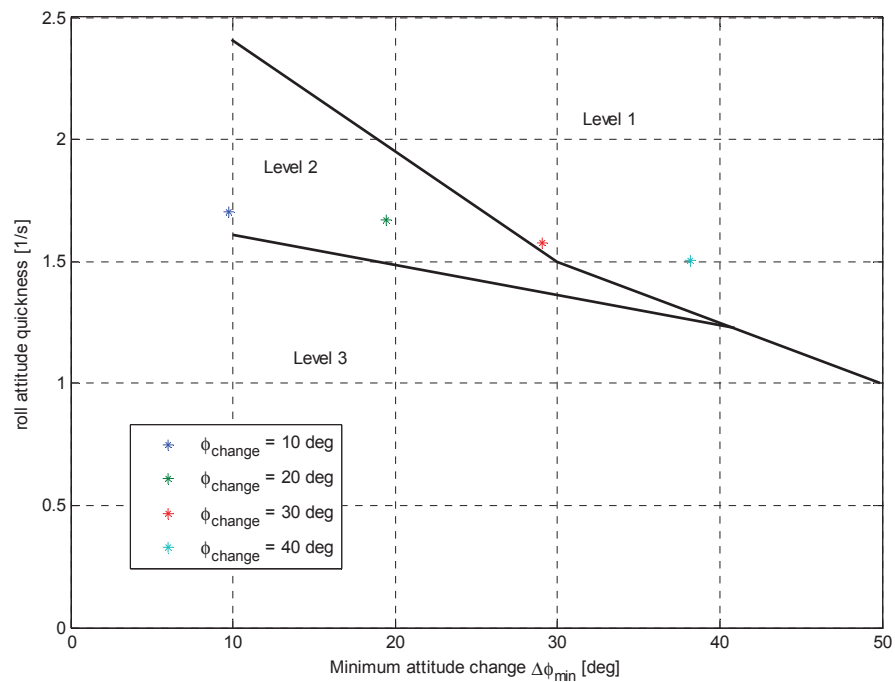
Figure 6.33: Roll attitude quickness compared with ADS-33 requirements
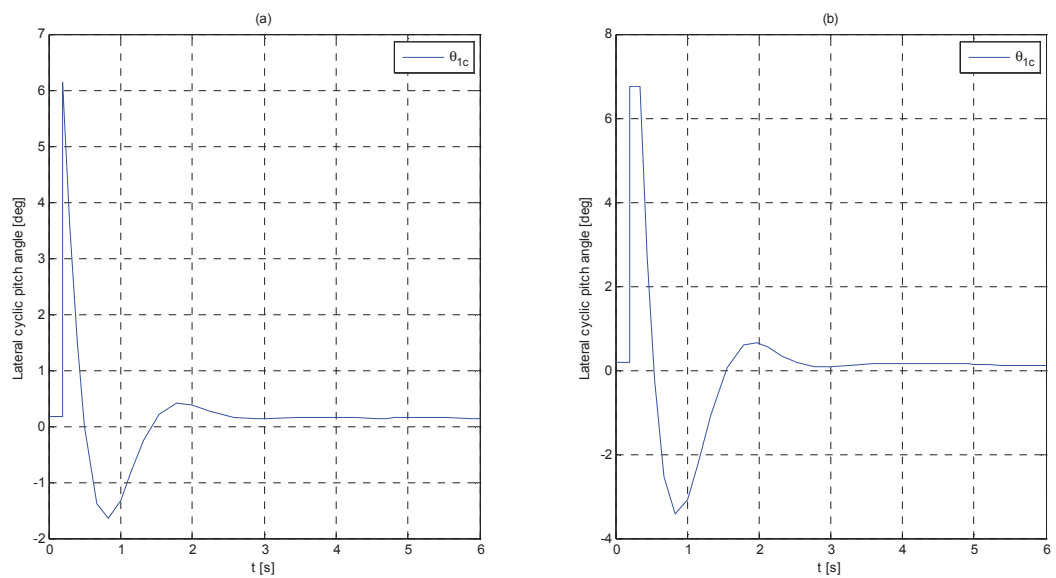

Figure 6.34: Lateral cyclic pitch angle behavior to achieve a roll attitude change of 10 degrees (a) and 20 degrees (b)

6.3.3 Yaw attitude quickness

Just as for the other quickness determinations, the yaw attitude quickness will be determined by giving a yaw attitude change to the coaxial helicopter model. This will be done for yaw changes from *10 deg* to *60 deg*. Subsequently, the quickness will be plotted against the minimum attitude change and will be compared with ADS-33 requirements.

The results of an attitude change of *10 deg* are given in Figure 6.35. The data of Figure 6.35 will be used to calculate one point in the 'quickness-plot'. The calculation for an attitude change of *10 deg* is given in eq. (6.10).

$$Q_{yaw(10\deg)} = \frac{r_{pk}}{\Delta \psi_{pk}} = \frac{11.2479 \text{ deg/s}}{10.9476 \text{ deg}} = 1.0274 \ s^{-1} \tag{6.10}$$

Figure 6.37 shows the calculated yaw quickness values for the simulated coaxial helicopter together with the approximated ADS-33 level boundaries. The yaw quickness does not deteriorate at higher yaw attitude changes. This should imply that the maximum achievable differential collective pitch angle is not reached, but Figure 6.36b shows clearly that the differential collective pitch limit is already reached at an attitude change of *40 deg*. The reason for this strange behavior is not known.

The coaxial yaw quickness values in Figure 6.37 do not comply with the level 1 requirement. Here should be expected much higher values, because, as mentioned in paragraph 6.2.3, the way how the yawing moment is achieved (see paragraph 3.3) can lead to very high yawing moments. In the first place, these low yaw attitude quickness values can be attributed to the same causes as for the roll and pitch quickness (wrong assumed moments of inertia and a wrong tuned PID-controller). But another important factor in this case is the distribution of the differential collective over the two rotors. In paragraph 6.1 the distribution has been fixed on *0.5* for the upper rotor and *-0.5* for the lower rotor, but this was just an assumption. In reality the distribution values can be a lot higher and in that case the quickness will substantially improve. To prove this statement, the yaw quickness is plotted for a distribution of 2.0 for the upper rotor and -2.0 for the lower rotor in Figure 6.38. Figure 6.38 shows an improvement of the yaw attitude quickness of about 40% in comparison with Figure 6.37. Furthermore, it can be seen in Figure 6.38 that the yaw quickness decreases a little bit at an increasing attitude change. This effect occurs, because with this differential collective distribution the collective pitch angle limit is reached and for a higher yaw attitude change this limit will be reached for a longer period. The behaviour of the yaw angles, yaw rates and control inputs for all attitude changes can be found in Appendix D.

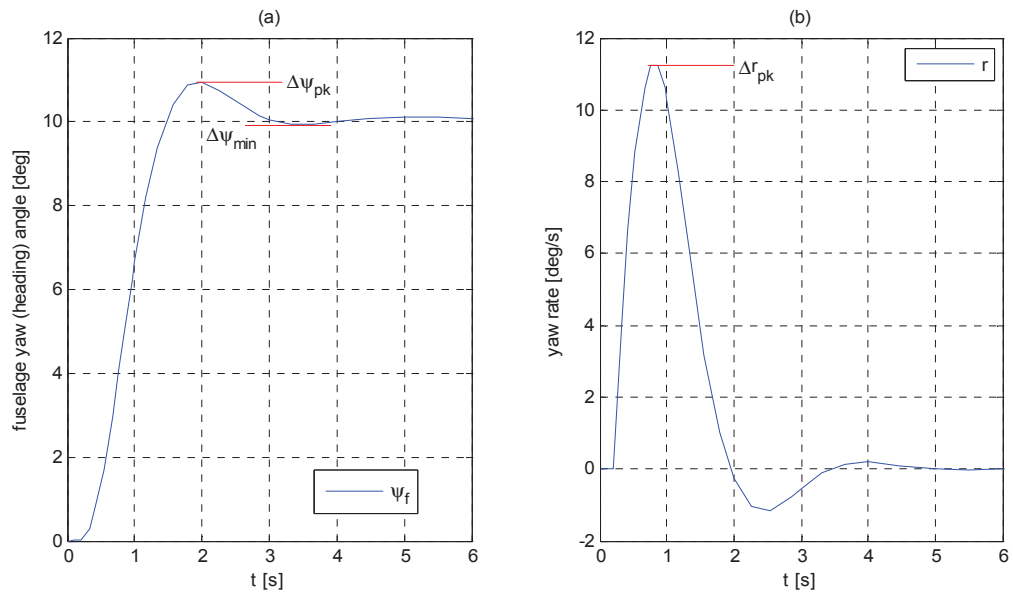Figure 6.35: Fuselage yaw angle and yaw rate behavior to achieve a yaw attitude change of 10 degrees
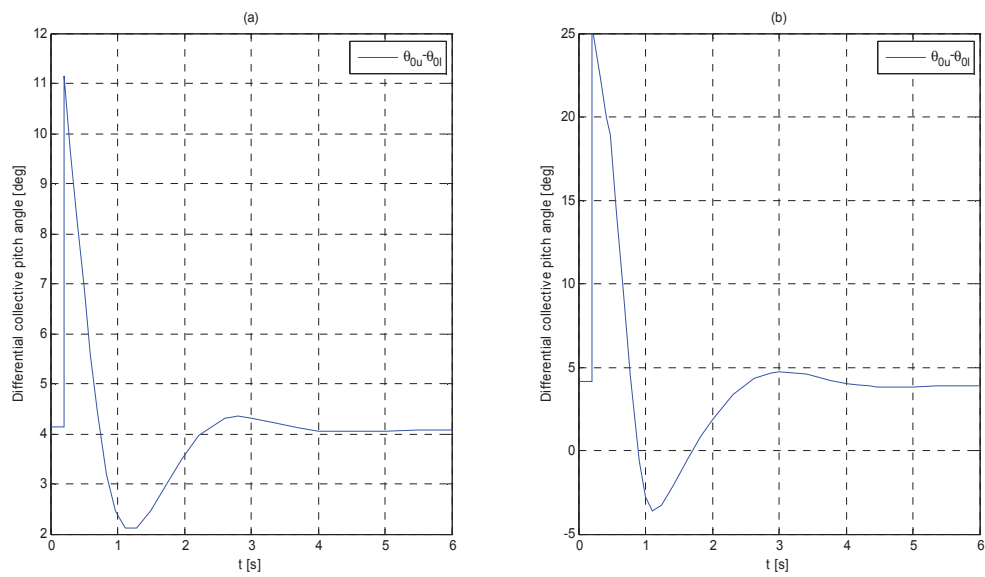

Figure 6.36: Differential collective pitch angle behavior to achieve a yaw attitude of 10 degrees (a) and 40 degrees (b)
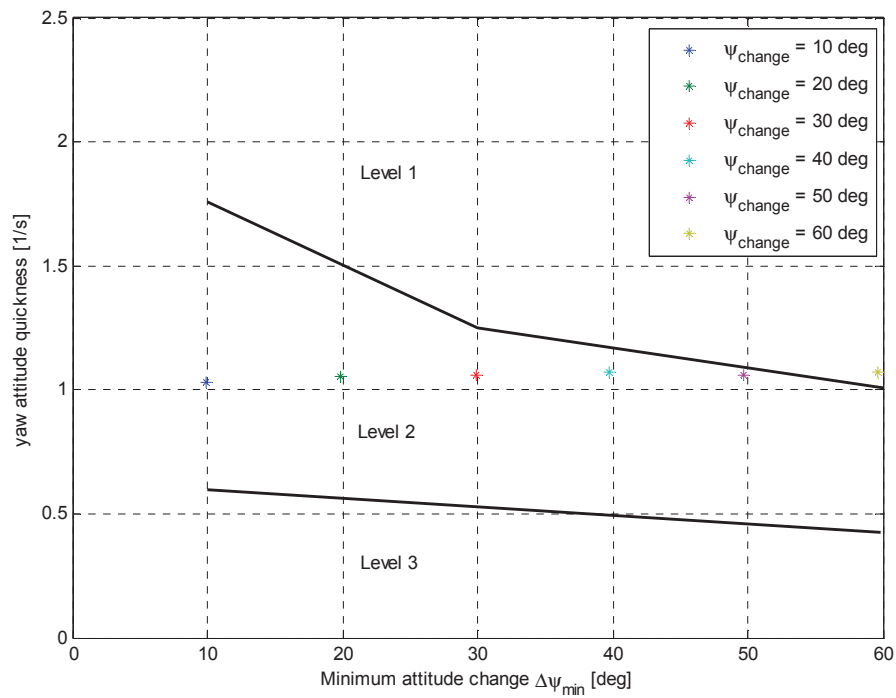
Figure 6.37: Yaw attitude quickness compared with ADS-33 requirements
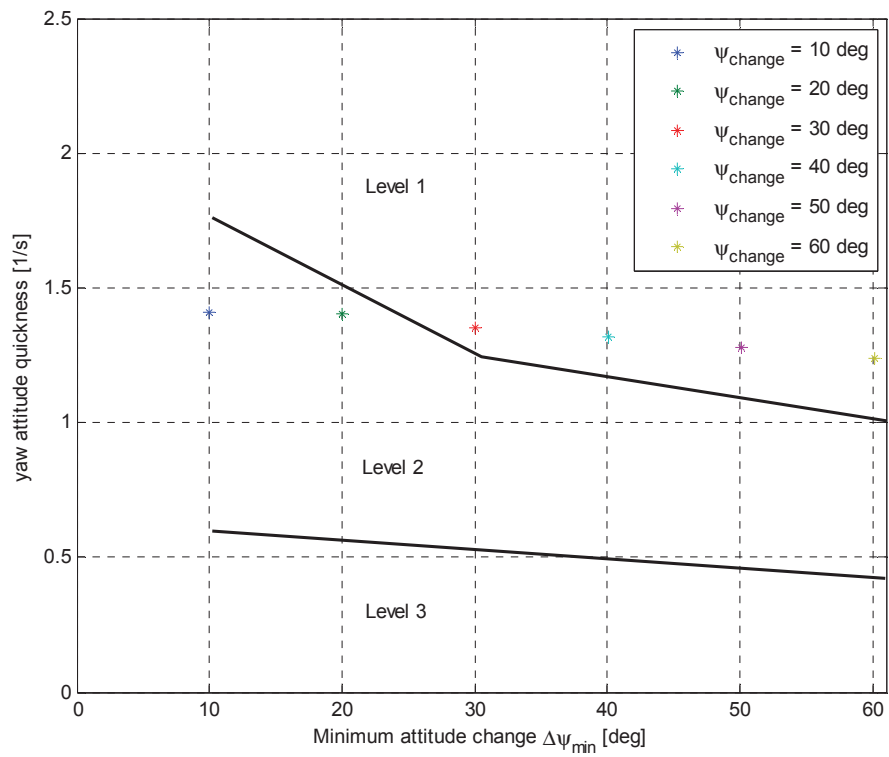

Figure 6.38: Yaw attitude quickness compared with ADS-33 requirements (with improved differential collective distribution)

7 Conclusions and recommendations

7.1 Conclusions

The main goal of this report was to develop a six degrees of freedom model for the coaxial helicopter. The main challenge was to find a method to make a proper simulation of the lower rotor acting in the wake of the upper rotor. The practical method for computing the induced velocity distribution below a lifting rotor from Walter Castles was found appropriate to find an attenuation coefficient which can be used to determine the influence of the upper rotor wake at each position of the lower rotor surface. The wake contraction is also taken into account by means of Landgrebe's generalized wake model. It was not possible to implement the attenuation coefficient in the BEM directly. Therefore the influence of the upper rotor wake at the lower rotor surface had to be approximated by dividing the lower rotor into sections. Subsequently, the BEM was applied on the different sections after which the results were added up to get the forces of the whole lower rotor.

After developing the model, Matlab was used to determine the trim conditions. Unfortunately, it was not possible to validate the trim results with measured coaxial data or even with simulated data. Therefore it was difficult to decide whether the obtained trim results were correct. However, the trim results were plotted together with Puma trim data and it can be concluded that both the coaxial and Puma data show qualitatively the same behaviour. The trim results also show some typical coaxial helicopter characteristics, like the smaller collective pitch angle for the lower rotor and the absence of cross-coupling between the longitudinal and lateral movements. Especially at higher forward speeds there is almost no cross-coupling between the axes and this coincides with the coaxial rotor theory.

Concerning the dynamic response of the coaxial helicopter there can be concluded that the coaxial helicopter model is able to stabilize after each given disturbance. Again, the separation between the longitudinal and lateral movements was well visible. The quickness of the attitude change on each axis is determined in order to visualize a handling quality of the coaxial helicopter. The used coaxial helicopter model did not comply with all level 1 quickness requirements of the ADS-33. However, after giving a maximum longitudinal pitch input for each attitude change, the pitch quickness of the coaxial helicopter was even two times the required quickness for level 1. This coincides with the expectations, but due the lack of coaxial helicopter data, it is not completely reliable.

7.2 Recommendations

The developed coaxial helicopter simulation model turned out to be a good working model, but of course some improvements can be made. First of all, the small amount of available coaxial data and measurements formed a hindrance to validate the developed model. So, if there is more information available in the future, the validation of the coaxial model as well as the comparison with the conventional single rotor helicopter can be substantially improved.

The trim results showed some unwanted behavior for the roll axis at low forward flight speeds. The exact reason is still not known, but supposedly the BEM creates, due to the approximated attenuation coefficients, some asymmetric forces at the lower rotor surface. Presumably this can be solved by making a better approximation of the attenuation coefficients. This can be done by dividing the lower rotor in more sections and in the ideal case applying the BEM with the accompanying attenuation coefficient for each radius and azimuth angle.

The upper rotor is assumed to have a uniform inflow. Especially at higher forward flight speeds, the inflow of the upper rotor is of course anything but uniform. In order to make a better approximation of the real case scenario, the upper rotor inflow can be assumed to be non-uniform.

The wake contraction of the upper rotor wake in forward flight is assumed to have the same value as in hovering flight. The reality can be better approximated by using a different wake contraction for each forward speed.

The coaxial helicopter turned out to have difficulties to stay steady at high roll angles. Presumably this is not a correct characteristic of the coaxial helicopter. The reason for this behavior is still not known and can be investigated in future studies.

A sensitivity analysis can be made of the influence of the separation distance between the rotors. References like Coleman (ref. 21) and Andrew (ref. 1) have already stated that "the greatest gains were made up to a separation distance of 0.05; thereafter, no "practical" gains resulted with increasing separation distance." In future studies, this statement can be confirmed or rejected.

Also a sensitivity analysis can be made of the influence of the moments of inertia of the helicopter. In this report the moments of inertia of the Puma helicopter have been used. In real case the moments of inertia of the coaxial helicopter are probably lower and could substantially improve the handling qualities of the coaxial helicopter.

8 References

1. Andrew M.J., *Co-axial rotor aerodynamics in hover*, Vertica vol.5, pp. 163-177, 1981

2. Akimov A.I., *Flight investigation of coaxial tip vortex structure*, 50th AHS forum, Washington D.C., 1994

3. Anikin V.A., *Aerodynamic-features of a coaxial rotor helicopter*, 17th ERF, Berlin, 1991

4. Anikin V.A., *Helicopter main rotor aerodynamic performance in descent conditions*, 58th AHS forum, Montreal, 2002

5. Anikin V.A., *Modelling of coaxial helicopter flight characteristics*, 27th ERF, Moscow, 2001

6. Azuma A., *Local momentum theory and its application to the rotary wing*, Journal of aircraft Vol. 16, no.1, 1979

7. Azuma A., *Application of the local momentum theory to the aerodynamic characteristics of multi-rotor systems*, Vertica vol. 3, pp. 131-144, 1979

8. Azzam H., *Investigation of helicopter twin-rotor characteristics*, 12th ERF, Garmisch-Partenkirchen, 1986

9. Bagai A., *Free-wake analysis of tandem, tilt-rotor and coaxial rotor configurations*, 51st AHS forum, Fort Worth, 1995

10. Boer J.F., *Specific aspects in the preliminary design process for small RUAVs*, 62nd AHS forum, Phoenix, 2006

11. Bohorquez F., *Design, analysis and hover performance of a rotary wing micro air vehicle*, AHS Journal, 2003

12. Bohorquez F., *Hover performance and swashplate design of a coaxial rotary wing micro air vehicle*, 40th AHS forum, Baltimore, 2004

13. Bourtsev B.N., *Blade flap motion and lower-to-upper rotorblade tips clearances of coaxial helicopters*, AHS Journal, vol. 41, 1996

14. Bourtsev B.N., *Phenomenon of a coaxial helicopter high figure of merit*, 23rd ERF, Dresden, 1997

15. Bourtsev B.N., *Coaxial helicopter rotor design and aeromechanics*, 25th ERF, Rome, 1999

16. Bourtsev B.N., *Aeroelasticity of a coaxial helicopter rotor*, 17th ERF, Berlin, 1991

17. Burgess K.B., *The ABC-rotor – A historic perspective*, 60th AHS forum, Baltimore, 2004

18. Castles W., *The normal component of the induced velocity in the vicinity of a lifting rotor and some examples of its application*, NACA TN-2912, 1953

19. Castles W., *Distribution of normal component of induced velocity in lateral plane of a lifting rotor*, NACA TN-3814, 1956

20. Cheney M.C., *The ABC helicopter*, AIAA paper, no. 69-217, 1969

21. Coleman C.P., *A survey of theoretical and experimental coaxial rotor aerodynamic research*, NASA TP-3675, 1997

22. Dingeldein R.C., *Wind-tunnel studies of multirotor configurations*, NACA TN-3236, 1954

23. Fusato D., *Design sensitivity analysis for ADS-33 quickness criteria and maneuver loads*, 58th AHS forum, Montreal, 2002

24. Gille M., *Simulation of a One-Engine-Inoperative helicopter landing*, Flight Mechanics exercise of the TU-Delft, Delft, 2006

25. Jacobs E.N., *Characterictics of the NACA 23012 airfoil from tests in the full-scale and variable-density tunnels*, NACA TR-530, 1936

26. Jane's All the world aircraft, edition 1990-1991

27. Johnson W., *Helicopter theory*, Dover publications, New York, 1980

28. Harrington R.D., *Performance of a coaxial rotor*, NACA TN-2318, 1951

29. Holten van Th., *Helicopter Performance and Control (AE4-213)*, TU-Delft, Delft, 2002

30. Hoydonk van W.R.M., *Development and validation of a numerical blade element method helicopter model in support of maritime operations*, MSc thesis TU Delft, Delft, 2006

31. Kawachi K., *Extension of local momentum theory to hovering rotor with distorted wake*, Journal of Aircraft Vol. 19, no. 7, 1982

32. Kist R.A., *Evaluation of single and coaxial rotor performance calculations with local momentum theory,* MSc thesis, Delft university of technology, Delft, 1995

33. Kvokov V.N., *Factor analysis of coaxial rotor aerodynamics in hover*, 18th ERF, Avignon, 1992

34. P. Lambermont and A. Pirie, *Helicopters and autogyros of the world / revised edition*, Cassel & company, London, 1958

35. Landgrebe A.J., *Helicopter airflow and wake characteristics for low speed and hovering flight*, 37th AHS forum, New Orleans, 1981

36. Landgrebe A.J., *An analytical method for predicting rotor wake geometry,* AIAA meeting 1969, Atlanta, 1969

37. Landgrebe A.J., *The wake geometry of a hovering helicopter rotor and its influence on rotor performance*, 28th AHS forum, 1972

38. Leishman J.G., *Aerodynamic optimization of coaxial proprotor*, 62nd AHS forum, Phoenix, 1962

39. Leishman J.G., *Principles of helicopter aerodynamics*, Cambridge University Press, New York, 2006

40. Mikheyev S.V., *Ka-50 attack helicopter aerobatic flight*, 24th ERF, Marseille, 1998

41. Mikheev S., *Coaxial helicopters present status and future development*, AIAA paper no. 2003-2939, Dayton, 2003

42. Nagashima T., *Optimum performance and wake geometry of co-axial rotor*, 7th ERF, Garmisch-Partenkirchen, 1981

43. Okuno Y., *Effects of difference in induced velocity distribution on the helicopter*, 13th ERF, Arles, 1987

44. Padfield G.D., *Helicopter flight dynamics*, 2nd edition, Blackwell Publishing Ltd., Oxford, 2007

45. Paglino V.M., *Forward flight performance of a coaxial rigid rotor*, 27th AHS forum, Washington D.C., 1971

46. Pavel M.D., *On the necessary degrees of freedom for helicopter and windturbine low-frequency mode modeling*, Delft university of technology, Delft, 2001

47. Pavel M.D., *Six degrees of freedom linear model for helicopter trim and stability calculation*, Memorandum M-756, Delft university of technology, Delft, 1996

48. R.W. Prouty, *Helicopter Performance, Stability, and Control*, Krieger publishing company, Malabar, 1986

49. Saito S., *A numerical approach to co-axial rotor aerodynamics*, 7th ERF, Garmisch-Partenkirchen, 1981

50. Samokhin V.F., *Acoustic certification of helicopter Ka-32A*, 27th ERF, Moscow, 2001

51. Su Y., *A nonlinear inverse simulation technique applied to coaxial rotor helicopter maneuvers*, Aircraft Engineering and Aerospace Technology, vol. 74, 2002

52. Sunada S., *Maximization of thrust-torque ratio of a coaxial rotor*, Journal of aircraft, vol. 42, 2005

53. United States army aviation and missile command, *Aeronautical Design Standard performance specification handling qualities requirements for military rotorcraft (ADS-33)*, Alabama, 2000

54. Valkov T., *Aerodynamic loads computation on coaxial hingeless helicopter rotors*, 28th Aerospace Science meeting, Nevada, 1990

55. Voorsluis G.M., *A modular generic helicopter model*, MSc thesis TU-Delft, Delft, 2002

56. Wachspress D.A., *Impact of rotor design on coaxial performance, wake geometry and noise*, 62nd AHS forum, Phoenix, 2006

57. Yee K., *Unsteady flowfield and noise propagation due to transonic airfoil interaction*, AIAA journal, vol. 36, 1998

58. Yee K., *An Euler calculation for a hovering coaxial rotor flow field*, 24th ERF, Marseille, 1998

59. Zimmer H., *The aerodynamic calculation of counter rotating coaxial rotors*, 11th ERF, London, 1985

Appendix A: Helicopter and controller parameters

The used helicopter data and PID-controller gains will be presented in this appendix.

Helicopter data

The Kamov Ka-32 coaxial helicopter is used to simulate the coaxial helicopter. As mentioned in paragraph 3.4, the available data of the Ka-32 is insufficient. If a certain helicopter parameter is coming from the Puma helicopter, it is marked with a "*".

General helicopter parameters

Parameter	Description	Value
m	Helicopter mass	10000 kg
I_{xx}*	Moment of inertia about x-axis	9638 kg m^2
I_{yy}*	Moment of inertia about y-axis	33240 kg m^2
I_{zz}*	Moment of inertia about z-axis	25889 kg m^2
J_{xz}*	Product of inertia about x-axis and z-axis	2226 kg m^2

Rotor parameters

Parameter	Description	Value
x_{hu}	Hub x-position of upper rotor relative to cg	0 m
y_{hu}	Hub y-position of upper rotor relative to cg	0 m
z_{hu}	Hub z-position of upper rotor relative to cg	2.186 + H m
x_{hl}	Hub x-position of lower rotor relative to cg	0 m
y_{hu}	Hub y-position of lower rotor relative to cg	0 m
z_{hu}*	Hub z-position of lower rotor relative to cg	2.186 m
H	Rotor separation distance	1.50255 m
Ω	Angular velocity of the rotors	28.4277 rad/s
R	Rotor radius	7.95 m
c	Rotor blade chord	0.48 m
N_b	Number of blades (of 1 rotor)	3
N_r	Number of rotors	2
I_β*	Rotor blade flapping moment of inertia	1280 kg m^2
K_β*	Flap hinge constant	33032 Nm/rad
θ_{tw}	Rotor blade linear twist	-6 deg
e	Flapping hinge offset	0 m
τ_λ	Time constant of rotor induced inflow	0.1 s
$C_{l\alpha}$	Rotor blade lift gradient (NACA 23012)	5.73 rad^{-1}
C_d	Rotor drag coefficient (approximated)	0.01

Blade pitch ranges

Parameter	Description	Value
θ_0*	Collective pitch angle	0 – 25 deg
θ_{1s}*	Longitudinal cyclic pitch angle	-15 – 15 deg
θ_{1c}*	Lateral cyclic pitch angle	- 6.75 – 6.75 deg

Fuselage parameters

Parameter	Description	Value
F_0*	Parasite drag area of the helicopter	1.8 m^2
K_{fus}*	Coefficient in fuselage pitching moment	0.83
Vol_{fus}*	Equivalent volume of circular body	6.11 m^3
C_DS	Equivalent flat plate area	4 m^2

Horizontal stabilizer parameters

Parameter	Description	Value
$C_{l\alpha\_hs}$*	Horizontal stabilizer lift gradient	4 rad^{-1}
α_0*	Horizontal stabilizer incidence angle	-1.5 deg
S_{hs}*	Horizontal stabilizer surface area	1.335 m^2
x_{hs}*	Horizontal stabilizer x-position relative to cg	-8.92 m

Vertical stabilizer parameters

Parameter	Description	Value
$C_{l\alpha\_vs}$*	Vertical stabilizer lift gradient	4 rad^{-1}
β_0*	Vertical stabilizer incidence angle	-1 deg
S_{vs}*	Vertical stabilizer surface area	1.395 m^2
x_{vs}*	Vertical stabilizer x-position relative to cg	-8.563 m
z_{vs}	Vertical stabilizer z-position relative to cg	0 m

PID-controller parameters

The gains for the PID-controllers are determined following the method as mentioned in paragraph 6.1.1.

Longitudinal cyclic controller

Parameter	Description	Value
K_θ	Proportional gain	-0.8
K_{θ_int}	Integral gain	-0.1
K_q	Derivative gain	0.3

Lateral cyclic controller

Parameter	Description	Value
K_Φ	Proportional gain	0.4
K_{Φ_int}	Integral gain	0.002
K_p	Derivative gain	-0.3

Collective (thrust) controller

Parameter	Description	Value
K_z	Proportional gain	-0.005
K_{z_int}	Integral gain	0
K_{zdot}	Derivative gain	0

Differential collective (yaw) controller

Parameter	Description	Value
K_ψ	Proportional gain	0.7
K_{ψ_int}	Integral gain	-0.001
K_r	Derivative gain	-0.4
K_{diff_u}	Distribution of differential collective to upper rotor	0.5
K_{diff_l}	Distribution of differential collective to lower rotor	-0.5

Appendix B: Description of the simulation program

Matlab is used to determine the trim conditions and the dynamic behavior of the developed coaxial helicopter model. The complete simulation program consists of several Matlab routines (M-files) and Simulink models. Each routine or model makes its own specific contribution to the desired result. Two main simulation programs can be distinguished: the trim program and the dynamic program. These two programs will be described in this appendix. The results which are used in this report are all tabulated. The tabulated data can be used to reproduce the results of the report. This is advisable, since the coaxial helicopter model is not quite fast. The mentioned m-files and Simulink models in this appendix as well as the tables with results can be found in the digital appendix.

The trim program

As mentioned in paragraph 5.1, the trim condition of a helicopter is a combination of states and controls in a specific flight condition for which the forces and moments are in equilibrium. In order to obtain a trimmed state of the helicopter for a given forward speed, it requires that the time derivatives of all state variables are zero. This can be seen in eq. (B.1)

$$f = [\dot{u} \ \dot{v} \ \dot{w} \ \dot{p} \ \dot{q} \ \dot{r} \ \dot{\lambda}_{0u} \ \dot{\lambda}_{0l}]^T = 0 \qquad (B.1)$$

The following set of trim variables is used to obtain a certain trim condition.

$$g = [\theta_f \ \phi_f \ \theta_{0u} \ \theta_{0l} \ \theta_{1s} \ \theta_{1c} \ \lambda_{0u} \ \lambda_{0l}]^T \qquad (B.2)$$

The trim program consists of 6 Matlab m-files. Figure B.1 shows the general layout of the trim program and how the different m-files are connected.
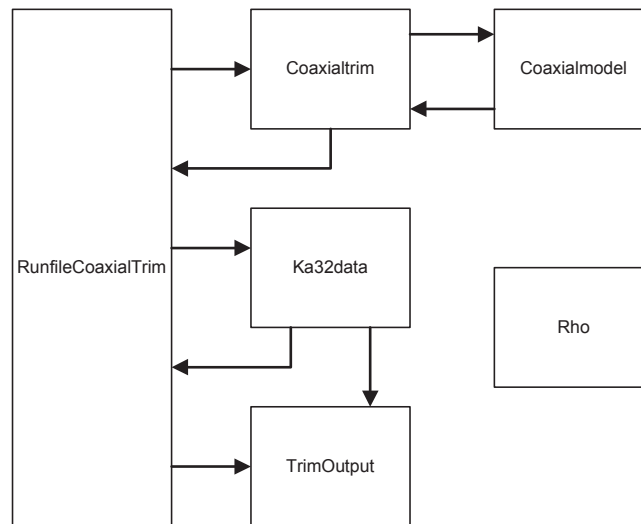

Figure B.1: Layout of the trim program

The Matlab m-files will now be discussed briefly.

- **RunfileCoaxialTrim.m**: This m-file starts the trim program. It controls the other Matlab routines.
- **Ka32data.m**: Ka32data.m provides all needed helicopter data of the Ka-32 coaxial helicopter. As mentioned in paragraph 3.4, Puma data will be used if the Ka-32 data are not available.
- **CoaxialTrim.m**: This m-file uses the Newton iteration method to get the trim conditions. It starts by giving initial (guessed) trim conditions and subsequently the new time derivatives of the states will be determined by using CoaxialModel.m. The Newton iteration method determines the new initial states for the next iteration step until the wanted trim condition (see eq. (B.1)) is met.
- **CoaxialModel.m**: This m-file contains the complete coaxial helicopter model as derived in chapter 4. First, the needed parameters for the BEM will be determined of each rotor and then it calculates the time derivatives of all state variables with the equations of motion.
- **TrimOutput.m**: The post processing file of the trim program. TrimOutput.m produces the desired trim- and power curves.
- **Rho.m**: Calculates the air density at the desired altitude.

The dynamic program

A dynamic simulation program is made in order to determine the dynamic response of the coaxial helicopter. Figure B.2 shows the general layout of the dynamic program and how the different m-files and Simulink models are connected.
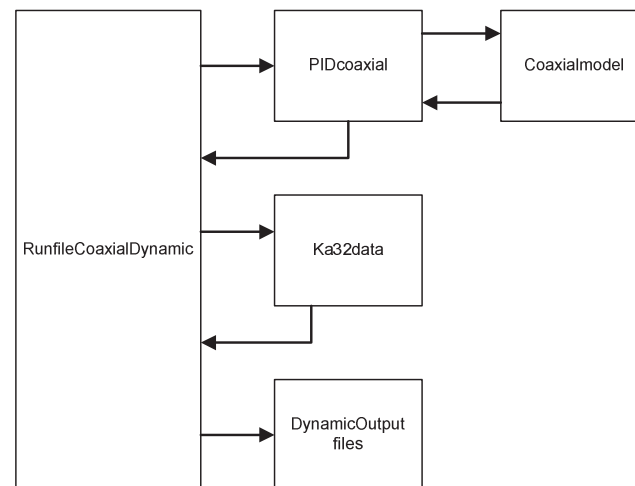

Figure B.2: Layout of the dynamic program

- **RunfileCoaxialDynamic.m**: This M-file contains the gains for the coaxial PID-controller and controls the Simulink simulation model of the coaxial helicopter: PIDcoaxial.mdl. It also loads the required trim data as an initial condition for the simulation.
- **Ka32data.m**: Ka32data.m provides all needed helicopter data of the Ka-32 coaxial helicopter. As mentioned in paragraph 3.4, Puma data will be used if the Ka-32 data are not available.

- **PIDcoaxial.mdl**: This model contains the developed PID-controllers for the coaxial helicopter as mentioned in paragraph 6.1. The model uses the same coaxial model as for the trim program to determine the time derivatives of the states. Subsequently, the time derivatives will be integrated in order to obtain the new states. The complete simulation model and the subsystems for each controller can be seen in Figure B.3 to Figure B.8.
- **CoaxialModel.m**: This m-file contains the complete coaxial helicopter model as derived in chapter 4. First, the needed parameters for the BEM will be determined of each rotor and then it calculates the time derivatives of all state variables with the equations of motion.
- **DynamicOutput.m**: This m-file initiates the desired output m-files for the different disturbances and quickness results.
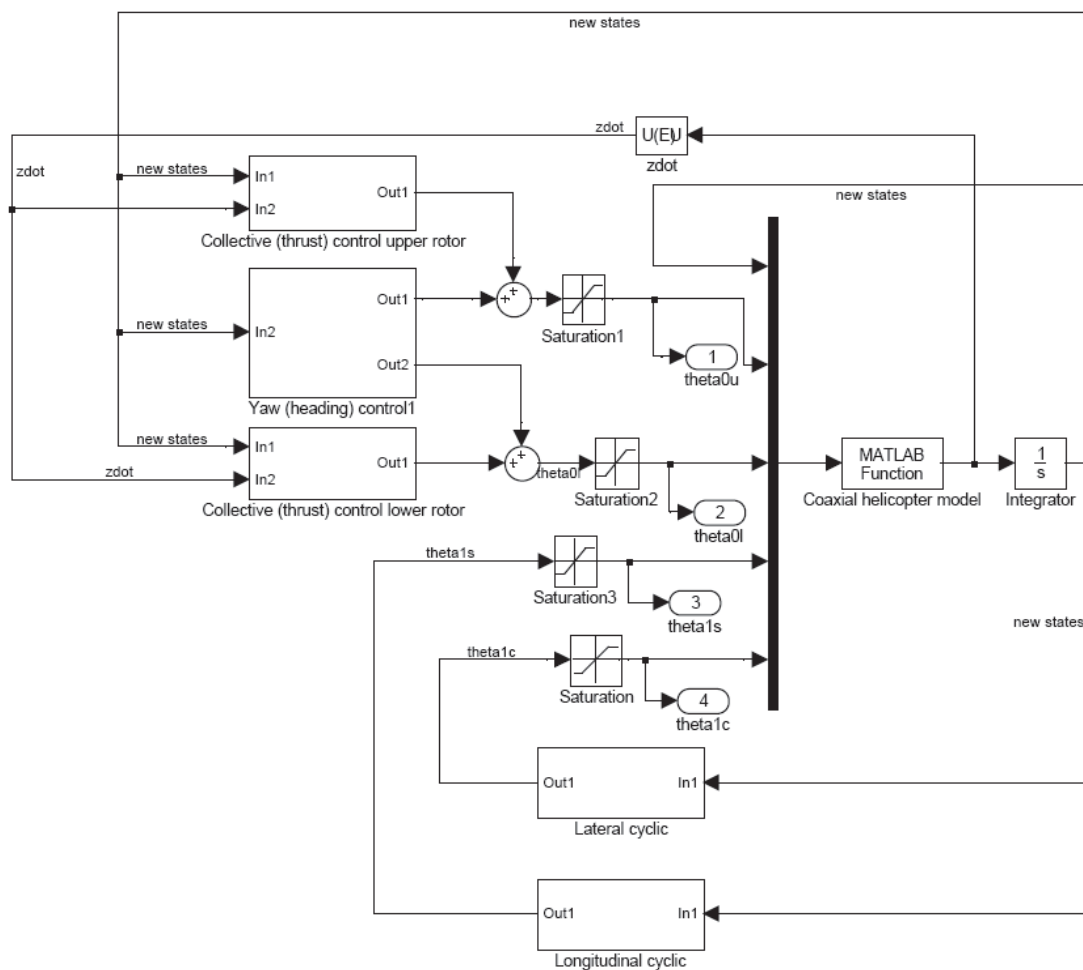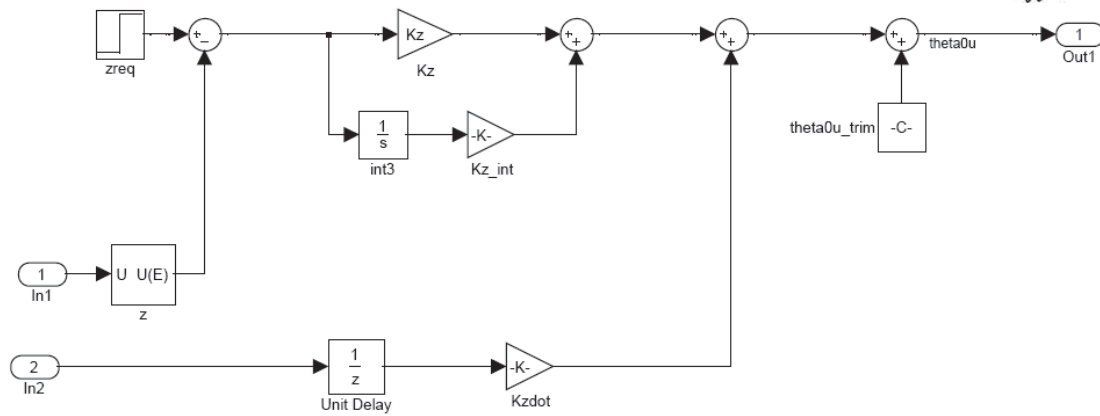

Figure B.3: Coaxial simulation model

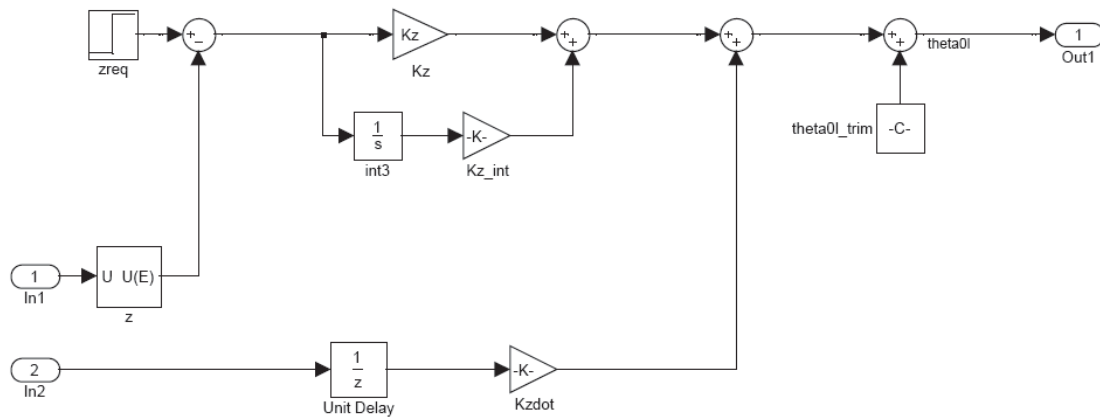**Figure B.4: PID-controller for the collective pitch angle of the upper rotor**

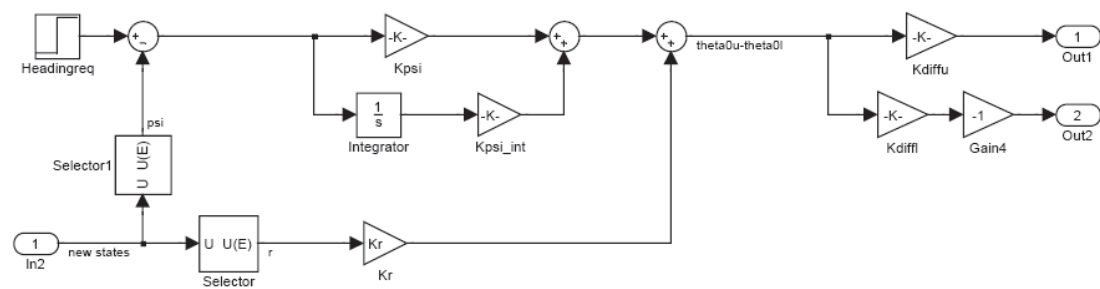**Figure B.5: PID-controller for the collective pitch angle of the lower rotor**

Figure B.6: PID-controller for differential collective pitch (heading) control
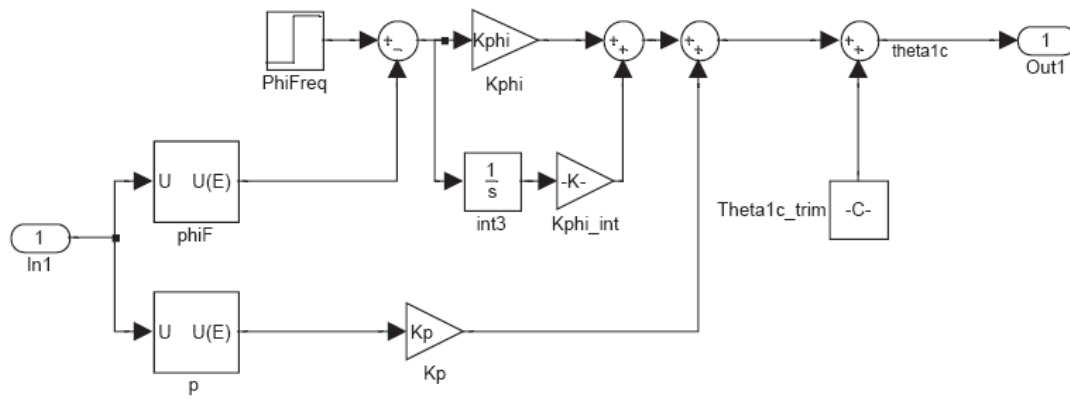
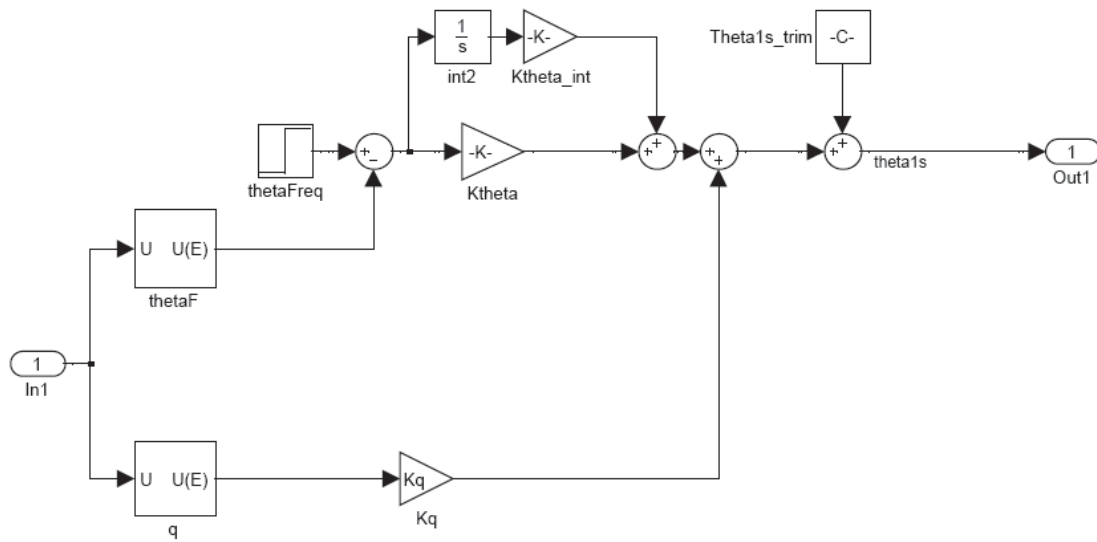**Figure B.7: PID-controller for the lateral cyclic control**

Figure B.8: PID-controller for the longitudinal cyclic control